

An Embedding Green Function Approach for Electron Transport through Interfaces

Von der Fakultät für Mathematik, Informatik und
Naturwissenschaften der Rheinisch-Westfälischen Technischen
Hochschule Aachen zur Erlangung des akademischen Grades
eines Doktors der Naturwissenschaften genehmigte Dissertation

vorgelegt von

Diplom Physiker
Daniel Wortmann

aus Münster

Berichter:

Universitätsprofessor Dr. Stefan Blügel

Universitätsprofessor Dr. Peter H. Dederichs

Tag der mündlichen Prüfung: 04.07.2003

Diese Dissertation ist auf den Internetseiten der Hochschulbibliothek online verfügbar.

An Embedded Green Function Approach for Electron Transport through Interfaces

The theoretical description of electron transport properties through nanoscale systems is one of the major challenges of contemporary solid state physics. Emerging new fields such as magnetoelectronics, spin-electronics or molecular electronics, areas with the potential to extend or replace the present microelectronics, are fueled by recent experimental successes in building such nanoelectronic systems.

In this thesis a new method is established, based on the combination of the embedding Green function method and the full-potential linearized augmented plane-wave (FLAPW) method, to describe the coherent and the sequential electron transport. By the use of the density functional theory realistic systems can be described on the atomic scale. The chosen numerical scheme, the FLAPW method, is today the most reliable and exact method available for first principle electronic structure calculations. However, different to standard bulk setups, the description of electron transport requires the treatment of the scattering problem which is particularly tricky when applying this method. Thus, a key part of the present thesis describes the development of a new computational scheme which is able to deal with a scattering region sandwiched between semi-infinite leads. Based on the ideas put forward by J. Inglesfield the existing FLEUR code is modified to calculate the single-electron Green function for the embedded scattering region. The semi-infinite leads are described in terms of a transfer-matrix formalism which enables one to obtain the so-called complex bandstructure of bulk materials

The electron transport is described using either the Landauer model or Bardeen's formalism of tunneling. These two formulas are discussed as two different limits of single-particle transport and their reformulation in terms of quantities readily available from the embedding method is presented.

Besides the presentation of the theory and the details of its implementation the thesis describes how the method has been applied to several different test systems to validate the implementation. The spin-dependent transport properties of the Fe/MgO/Fe tunneljunction, the model system of tunnel-magnetoresistance (TMR), were investigated. It is shown that the details of the Fe/MgO interface in this junction is of crucial importance for the tunneling conductance. While the pure relaxation of a Fe/MgO interface already changes the conductance, even more drastic modifications are found as soon as one FeO layer is inserted or if the interface is modified by interchanging the Mg and O atoms.

Contents

1	Introduction	1
2	Density Functional Theory	7
2.1	The Hohenberg-Kohn Theorem	8
2.2	Single Particle Formulation	9
2.3	The Exchange-Correlation Potential	12
3	Concepts of Electronic Transport	15
3.1	Basic Considerations	16
3.2	The Landauer Approach	17
3.3	Interpretation of the Landauer Formula	21
3.4	The Bardeen Approach to Tunneling	22
3.5	Experimental Setups	27
3.5.1	Scanning Tunneling Microscope	27
3.5.2	The Junction-Magneto-Resistance	29
4	Green Function Embedding	33
4.1	The Embedding Problem	33
4.2	Setup	35
4.3	The Schrödinger Equation in the Embedding Region	37
4.4	Variational Principle	38
4.5	The Embedding Potential	40
4.6	The Embedded Green Function	41
4.7	Self-consistent Embedding	43

5	Complex Bandstructure, Embedding and Transport	45
5.1	The Transfer-Matrix	46
5.2	T-Matrix and Complex Bandstructure	49
5.3	Complex Bandstructure and Embedding Potential	51
5.4	Wavefunction-Matching	53
5.5	Landauer Formulation	55
5.6	Green Function formulation of Bardeen's Approach to Tunneling . . .	61
6	The FLAPW-Method	63
6.1	The FLAPW Basis Set	65
6.2	The Boundary Conditions	68
6.3	Two regions	70
6.4	Auxiliary volumes	72
6.5	Construction of the Hamiltonian	74
6.6	Calculation of the Green Function	75
6.7	The Transfer-Matrix	77
6.8	Embedding Potential	79
6.9	Construction of the Charge Density	80
	6.9.1 Interstitial region	81
	6.9.2 Muffin-tin spheres	82
6.10	Potential Setup	83
7	First results	87
7.1	Some Recipes	87
7.2	Complex Bandstructures	90
7.3	Basis set in CBS calculations	95
7.4	Transmission from the Green Function	98
7.5	Landauer conductance versus Bardeen's tunneling	102

8	The Fe/MgO/Fe Tunneljunction	107
8.1	Structure	108
8.2	Electronic Structure	111
8.3	Ferromagnetic Fe/MgO/Fe junction	113
8.4	Bardeen's approach applied to the Fe/MgO	117
8.5	LDA+U for MgO	119
8.6	Additional Oxide Layer	122
8.7	Artificial Interface Setup	125
8.8	Antiferromagnetic Alignment, TMR	127
8.9	Conclusions	128
9	Summary and Outlook	129
	Bibliography	132

Chapter 1

Introduction

Increasingly smaller and faster semiconductor circuitry has fueled over the past decades the information technology, producing ever cheaper and faster computing devices that have virtually entered every corner of our modern life and is turning our societies into a global information society. This was made possible since semiconductor electronics have seen a sustained exponential decrease in size and a similar increase in the level of integration over the past 40 years. Known as *Moore's Law*, since the mid seventies, the number of transistors on a semiconductor chip doubled every 18 months. The characteristic feature size will soon fall below the 100 nm mark and will continue to shrink to approximately 20 nm by the year 2015. To all what is known today, the 20 nm structure size provides a barrier for conventional electronics, beyond which a straightforward down-scaling of the feature size keeping the operation principles of today's electronics will not work. Characteristic phenomena for structures of a few nanometers in size are the very few charge carriers, the relevance of single dopant atoms, their non-uniformity, the relevance of single atom defects, the large surface-to-volume ratio, and the high electric fields across small structures. In addition, quantum phenomena will increasingly start to modify and dominate the overall behavior of such devices.

At this frontier nanoelectronics is emerging as a new field geared to continuously alter or replace the present microelectronics. Nanoelectronics research encompasses e.g. magnetoelectronics, spin-electronics or spintronics, and molecular electronics or molelectronics – areas of great potential for future technology. Recent experimental successes like the discovery of the giant magneto resistance effect in magnetic multilayers by Grünberg [BGSZ89] and Fert [BBF⁺88] the realization of the tunneling magnetoresistance effect first described by Julliere [Jul], the spin injection in semiconductors and the electronic transport through single molecules (see e.g. [WRW⁺])

has intensified the interest in describing the electron transport on the atomic scale. A current key issue is the understanding of the electron transport through an atomically sharp interface, single molecules and atomic scale contacts. This requires a transport description based on the detailed electronic structure and depending on the realistic atomic scale geometry and arrangement of the system at hand.

The theoretical description of the complicated interplay between the electronic and magnetic structure, the geometrical constriction and the non-equilibrium situation which determine the transport properties of these systems is one of the major challenges of contemporary solid state physics. Currently at least two different physics communities face the challenge from two different angles: One is the mesoscopic community, with a strong background in non-equilibrium transport able to describe electron correlation effects at low-temperatures. Examples include the fractional quantum Hall effect, the transport through quantum dot arrays exhibiting Kondo-effect, and single-electron devices governed by the Coulomb blockade. In many of these systems the electron wave length is large as compared to the atomic details and the electron wave function can be replaced by an envelope function. The treatment of atomistic details are therefore less important in these cases.

The second group is the electronic structure community, which is currently also making big efforts to tackle the problems of nanoelectronics. This community typically centers around the description of the electronic structure of realistic systems using the density functional theory introduced by Hohenberg and Kohn. Approximating the exchange and correlation of the interacting many electrons by the local density or the generalized gradient approximation this theory turned out to be very powerful in describing the ground state properties, such as the lattice structure or elastic and magnetic properties of realistic low-dimensional systems. The theory makes the description of the many-body problem in a single particle picture possible. How to treat the non-equilibrium transport properties beyond the static Hohenberg-Kohn eigenstates is a current research issue.

In order to use the density functional theory to describe the transport properties one has to keep in mind that the core of the electronic structure methods developed over the past decades focus on finding eigenstates for electrons in increasingly more complex material systems. These eigenstates are usually calculated with periodic boundary conditions and can be used to calculate the total energy of the system or forces exerted on the atoms. For the description of electron transport, however, one has to consider a scattering problem.

In solving the density functional theory equations for the transport properties different degrees of approximations allow different depths in the treatment transport

properties. Using theories of non-equilibrium transport model setups using semi-infinite jellium electrodes [Lan95, DVPL00, DVKPL01] have been investigated. On the same level, transport has been treated using pseudo-potentials and the linear combination of atomic orbitals (LCAO) method [MOB⁺02, TBS02]. Methods of time-dependent density functional theory [ORR02] might be employed as a basis for a time dependent treatment of the transport process. Others have used more sophisticated methods of density functional theory but a much simpler transport theory. Schemes based on wavefunction matching [AH72, HT94, HT95, NBHJ99, KBT00] have been the basis of studies of ballistic, coherent transport [SH88, Sti96]. The same description of transport is found frequently in calculations based on a single-electron Green function using either empirical or non-empirical tight binding schemes [CBLC96, CVHSS97, Mat97], more realistic formulations like the Korringa-Kohn-Rostoker (KKR) methods [KS76, WZD⁺98] or on the tight-binding linear muffin-tin orbital (TB-LMTO) methods [KDT⁺00, XKB⁺01].

The starting point of this thesis is the full-potential augmented plane-wave (FLAPW) method, a state-of-the-art method for first principle electronic structure calculations. Developed over a long period of time, starting with the APW-method of Slater, followed by the linearized method (LAPW) developed by Anderson, Koelling and Arberman in the 1970th, and the implementation of the full-potential extension and the total energy by Weinert and Wimmer, the FLAPW method is today the most reliable and exact method available for electronic structure calculations. It can be applied to open structures and systems with low symmetry and can describe magnetic and complex materials with high accuracy. However, general applications of the method are restricted to periodic structures or two-dimensional films in vacuum. The treatment of the scattering problem of electronic transport is particularly tricky applying this method. The main problem is that the periodic boundary condition usually used to describe the general case of solids with translational symmetry is already used in the definition of the plane-wave basis set of the FLAPW method. In 1981 Inglesfield proposed a method that can be used to overcome this difficulty. By adding an additional term to the Hamiltonian the correct boundary condition for the scattering problem can be obtained. The basic idea in this method is to include the boundary condition imposed on the solution of the Schrödinger equation into the same variational principle from which the Schrödinger equation is derived to treat this boundary condition also variationally.

This thesis is based on the implementation of this idea of embedding into the existing FLAPW code `FLEUR` to calculate the embedded single-electron Green function. One of the most difficult problems in the application of the embedding method is the

calculation of a quantity which was called „embedding potential“ by Inglesfield and which controls the boundary condition imposed. We developed a transfer-matrix formalism and applied it to calculate the so called complex bandstructure of bulk materials and the corresponding embedding potentials. The electron transport is treated in two different models. The Landauer model of transport treats transport in the regime in which a single-electron wavefunction is assumed in all space, i.e. it describes the coherent transport. The theory of Bardeen is frequently used in the case of tunneling and assumes two well separated systems with a small coupling that can be treated in time dependent perturbation theory. Both transport formulas have been rewritten in terms of quantities readily available from the embedding method.

Besides the different aspects of the theory and its implementation into the FLAPW code, also some applications are presented. The very powerful concept of the complex bandstructure is discussed and some examples of complex bandstructures of real materials are discussed. The two different transport formulas are compared for a simple Cu/Vacuum/Cu junction to demonstrate their properties and to point out differences. Finally, the Fe/MgO/Fe junction proposed for the construction of atomically ordered tunnel magneto resistance (TMR) devices is investigated. This setup became the model system for the *ab-initio* treatment of TMR since it allows the growth of perfectly ordered tunnel barriers between magnetically ordered metallic leads. The results demonstrate that details of the Fe/MgO interface are of crucial importance for a correct description of the tunneling conductance of this junction.

The present thesis is organized as follow: In the first chapters the different prerequisites to describe the electronic transport will be presented. A very brief introduction into the fundamentals of the density functional theory will be given first. After that the focus will be on the different models of electronic transport used. The physical significance of these models will be discussed and their foundations will be clarified. The fundamental formulas of the embedding method will be shown in chapter 4. After these chapters containing the fundamentals of the theory, the following two will deal with the details of the formulation of electronic transport by means of the obtained single-electron Green functions and with the implementation of the formulas within the framework of the FLAPW method. Chapter 7 will start with a description of how the different concepts and formulas work together and how the actual calculations are performed followed by some first results for different test systems. The last large chapter of this thesis will use the newly developed method to investigate the Fe/MgO/Fe junction. The influence of the details of the atomic and electronic interface structures will be studied. The summary of the work will be extended by giving some ideas of possible further applications and extensions of

the method.

Chapter 2

Density Functional Theory

In order to calculate properties of the solid state one must in principle solve the Dirac-equation for an enormous number of interacting particles. It is not possible to solve this equation analytically for nontrivial systems. In the past many different schemes have been developed to tackle this many-body problem. The most well known of those are probably methods based on quantum-field theoretical formalisms of many-body perturbation theory. However, while these methods are well suited for a limited number of particle interacting with external fields, the enormous number of different particles in solids and their very different characteristic interaction time and length-scales restricts the applicability of these methods to solid state physics to model systems with different levels of approximations.

A breakthrough in the treatment of the many-body problem was provided by the invention of the density-functional theory(DFT) by Hohenberg and Kohn [HK64, JG89]. They proved that – at least for calculation of the ground state properties – the many-body problem can be replaced by the much simpler problem of minimizing an energy functional of a single particle density. The density functional theory is the foundation of most modern numerical methods which describe solid on an *ab-initio* level, i.e. without using external parameters but by minimizing an energy functional that is unique, e.g. independent of the system in question.

Density functional theory is in principle able to describe the full many-body system. However, to reduce the computational effort, one generally uses the Born-Oppenheimer approximation [AM76]. This is the frequently used idea to separate the atomic degrees of freedom from that of the electrons. Since the mass of the atomic nuclei is at least three orders of magnitude larger than the mass of the electrons one can keep the nuclei at fixed positions while solving the electron problem. In this approach one neglects any quantum effect which may arise from the dynamics of

the nuclei such as the electron-phonon interaction.

Nowadays, the probably most successful and most often used technique to solve the remaining many electron problem is based on the density-functional theory of Hohenberg and Kohn [HK64, JG89].

This chapter will give a brief introduction into the basics of the density functional theory. Since this is not the main subject of this work, this part will be kept very short. It will not deal in detail with any of the more subtle problems arising from e.g. degenerate ground states. Further information on those subjects can be found in [Koh83, Lev79, Esc96]. The presentation will also be restricted to the non-magnetic, non-relativistic case.

2.1 The Hohenberg-Kohn Theorem

There are two theorems which are the foundation of density functional theory which are attributed to Hohenberg and Kohn [HK64] :

1. Theorem: All ground-state properties are functionals of the ground-state density $n(\vec{r})$.

For a system with a non-degenerate ground-state, it immediately follows that the ground-state itself, i.e. the many-particle wavefunction of the ground-state, is a functional of the ground-state density. This first theorem determines the basic strategy that can be used to deal with the many electron system of a solid. Not the many-particle wavefunction is the quantity which will be determined, but the electron density $n(\vec{r})$. Since this function depends on only three independent spatial coordinates rather than on $O(3^{10^{23}})$, this is a great simplification of the numerical task.

2. Theorem: The ground-state total energy functional is minimal for the correct ground-state density with respect to variations of all densities leading to the correct number of electrons.

This second theorem now gives a minimization principle which can be used to determine the ground-state density. If the form of the total energy functional is known, the ground state density can be determined using this second theorem.

2.2 Single Particle Formulation

At this point one has to deal with the question how this total energy functional looks like. In a many particle picture the density is given by $n = \langle \Psi | \Psi \rangle$ where Ψ denotes the antisymmetric many-particle wavefunction. Assuming that the density can also be expressed in terms of single particle eigenfunctions Ψ_i of a system of electrons in some external potential V_{ext} the density can be obtained by

$$n = \sum_{i=1}^N \langle \Psi_i | \Psi_i \rangle . \quad (2.1)$$

A discussion of the existence of such a decomposition of the charge density into single particle states can be found in [Lev79]. Using these single-electron states the energy functional $E[n]$ was expressed by Kohn and Sham [KS65] in the following form

$$E[n] = T[n] + E_{ext}[n] + E_H[n] + E_{xc}[n] \quad (2.2)$$

where $T[n]$ denotes the kinetic energy of a non-interacting electron gas of density n , E_{ext} describes the interaction with the external potential V_{ext} , E_H contains the classical Coulomb interaction, i.e. the Hartree contribution to the energy, and E_{xc} (which is called the exchange-correlation energy) describes all many-body quantum contributions beyond the Hartree-approximation.

The energy of the interaction with the external potential is given by

$$E_{ext} = \int V_{ext}(\vec{r}) n(\vec{r}) d\vec{r}, \quad (2.3)$$

where V_{ext} describes some external potential, to which the Coulomb potential of the nuclei will be the largest contribution.

The Hartree-term is given by

$$E_H[n] = e^2 \int \int \frac{n(\vec{r}) n(\vec{r}')}{|\vec{r} - \vec{r}'|} d\vec{r} d\vec{r}'. \quad (2.4)$$

The exchange-correlation contribution to the total energy functional is unknown for general systems. I will later deal with the question how to approximate this term.

The kinetic energy $T[n]$ is the kinetic energy of N non-interacting electrons:

$$T[n] = \sum_{i=1}^N \langle \Psi_i | -\frac{\hbar^2}{2m} \nabla^2 | \Psi_i \rangle \quad (2.5)$$

The introduction of single-electron wavefunctions into the problem enables one to apply the variational principle of Rayleigh-Ritz (see for example [SW93]) to Eq. (2.2). By applying the method of Lagrange multipliers to the problem one obtains a Schrödinger equation like set of differential equations forming an one-particle eigenvalue problem [KS65]:

$$\left\{ -\frac{\hbar^2}{2m}\nabla^2 + V_{ext}(\vec{r}) + e^2 \int \frac{n(\vec{r}')}{|\vec{r} - \vec{r}'|} d\vec{r}' + V_{xc}(\vec{r}) \right\} \Psi_i = \epsilon_i \Psi_i. \quad (2.6)$$

This equation, which is called the Kohn-Sham equation, has the form of a Schrödinger equation, in which the external potential, the Coulomb interaction and an exchange-correlation potential form an effective potential for non-interacting particles. This exchange-correlation potential is connected to the exchange-correlation energy functional of the previous section by a functional derivative

$$V_{xc}(\vec{r}) = \frac{\delta E_{xc}[n]}{\delta n(\vec{r})}. \quad (2.7)$$

Thus, the minimization process corresponds to the determination of the solution of Eq. (2.6) with respect to the constraints

$$\int |\Psi_i(\vec{r})|^2 d^3\vec{r} = 1, \quad (2.8)$$

which leads to the introduction of the Lagrange multipliers ϵ_i . Since the potentials in Eq. (2.6) depend on the electron-density, which in turn depends on the one-particle wavefunctions Ψ_i by Eq. (2.1) the Kohn-Sham equation has to be solved self-consistently.

This self-consistent solution is obtained in an iteration process as shown in Fig. 2.1.

At this point I would like to discuss the significance of the single particle states Ψ_i and of the corresponding energies ϵ_i . Strictly speaking, these energies do not possess any physical significance. Similarly, the eigenvectors of equation (2.6) do not have any meaning. It is, however, quite common to interpret the single particle energies ϵ_i as excitation energies of electrons and also to use the states Ψ_i as corresponding one-particle wavefunctions in this way. It is known [Jan78, Per83] that the Fermi energy of this independent particle system, e.g. the energy ϵ_N of the highest occupied state, is indeed the work function of the system. Furthermore, it is known that for energies ϵ_i which differ substantially from ϵ_N , the energies ϵ_i do not reproduce the excitation energies very well. Especially, in general Koopmann's theorem is not valid

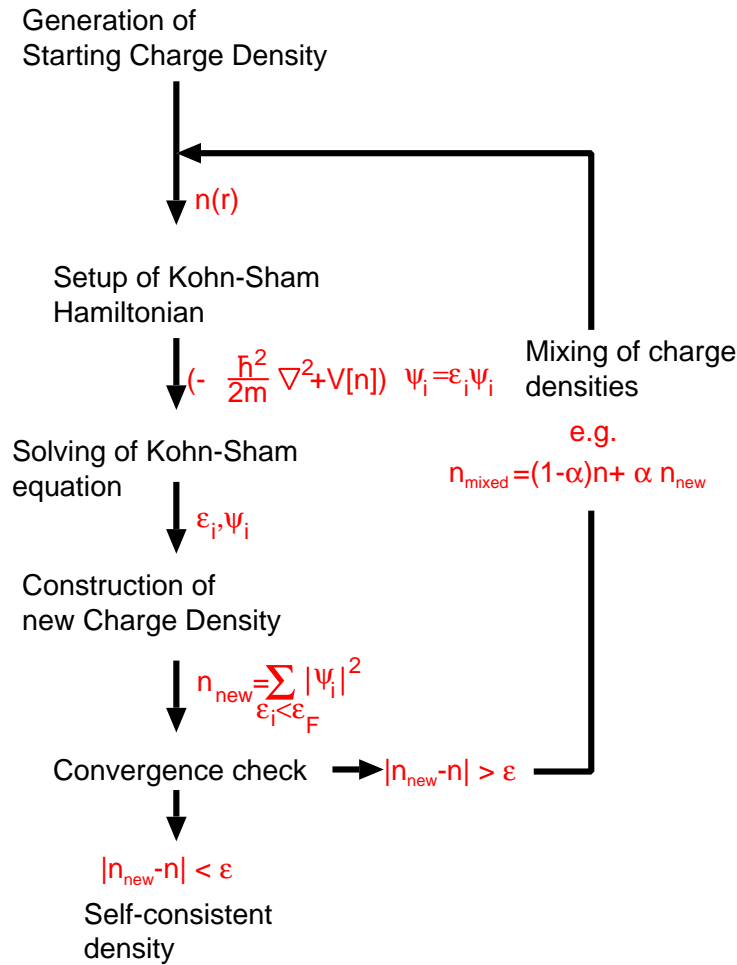


Figure 2.1: The self-consistency iteration process used to solve the Kohn-Sham equations self-consistently.

for density functional theory [JG89].

Even though the eigenstates and eigenvalues do not have any physical meaning in the very strict interpretation of the theory, it turned out, that in many cases they describe the single particle excitations of the system reasonably. Therefore these states are frequently assumed to describe these excitations. In this thesis, electron transport will also be formulated in terms of the eigenvectors and eigenvalues obtained from the Kohn-Sham equations. Consequently, the Kohn-Sham equation will also be called Schrödinger equation and will be assumed to be an equation describing single-electron wavefunctions.

2.3 The Exchange-Correlation Potential

As described so far, density functional theory contains no approximations. The charge density $n(\vec{r})$ obtained by solving the Kohn-Sham equation (2.6) self-consistently would be the exact ground-state density. However, this solution will only be possible if the exchange-correlation energy E_{xc} is known.

Many ways of approximating this energy have been explored. The most widely used approximation is the Local Density Approximation (LDA) or its spin dependent version, the Local Spin Density Approximation (LSDA). In this approximation the exchange-correlation energy is chosen to be at every point \vec{r} the exchange-correlation potential of a free electron-gas with a uniform density of $n(\vec{r})$. The exchange-correlation energy therefore is given by

$$E_{xc}[n(\vec{r})] = \int n(\vec{r})\epsilon_{xc}(n(\vec{r})) d^3r, \quad (2.9)$$

where ϵ_{xc} is no longer a functional of the density but just a function. This approximation is therefore exact in the limit of a free electron-gas with uniform density, and one would expect that the approximation also performs reasonably well for a slowly varying density $n(\vec{r})$. Nevertheless, experience has shown that this approximation also reproduces the main properties of metals quite accurately. Therefore, this approximation can be used to perform calculations on metals with good results. In practice, expression (2.7) is evaluated using an explicit parameterization of $\epsilon_{xc}(n)$. These parameterizations can be obtained by fits to quantum-mechanical many-body calculations. Some parameterizations that are frequently used are those of v. Barth and Hedin [vBH72] or of Moruzzi, Janak, and Williams [MJW78], which are based on the random phase approximation or the parameterizations of Vosko, Wilk, and Nusair [VWN80] or of Perdew and Zunger [PZ81], which are based on Quantum-Monte-Carlo simulations. The most widely used exchange-correlation potential beyond the LDA, the so called generalized gradient approximations (GGA) are based on the extension of Eq. (2.9) to include also the gradient of the density such that the exchange-correlation functional depends on the local density and on the local gradient. Obviously, such a functional can not be motivated from a uniform electron gas like the LDA. However, it has been shown that in some systems, for example in some molecules, in which the assumption of a uniform electron density is questionable the GGA can improve beyond the LDA results.

While the LDA (or GGA) provides good results for systems in which the electrons are delocalized it fails in strongly correlated systems with localized states. In general it

is well known that the LDA tends to overestimate the hybridization and the chemical bonding leading to an underestimation of the lattice constant. Even more seriously, the LDA fails spectacularly in several semiconducting and insulating materials by predicting no bandgap and thus giving a metallic ground state. To improve the results in these cases several different attempts have been made to improve the approximation of the exchange-correlation potential. Probably the most successful and most developed approach is the so called GW-approximation which tries to approximate the excitation of the N-electron system into a (N+1)-electron system in a many-body quantum theoretical way. The key quantities in this approach are the one particle Green function (G) and the screened Coulomb interaction (W). The major drawback of the method are its enormous computational costs.

Other schemes focus on more specific aspects to improve the LDA such as the „self-interaction correction“ in which the correlation part of the exchange-correlation potential is improved by explicitly subtracting the self-interaction of the localized wavefunctions with the charge density due to the same state. It has been demonstrated [TSW93] that this approach can greatly improve the resulting total energies and that it can predict a gap in many oxide materials in which LDA fails.

In this work I will present some results obtained by using the so called LDA+U scheme. This is a somewhat simpler scheme based on the idea of introducing an orbital dependent potential to correct the LDA for the missing strong on-site Coulomb interaction which is the origin of the splitting between the occupied and unoccupied states. Formally, the LDA exchange-correlation functional is modified by adding two extra terms

$$E_{\text{LDA+U}} = E_{\text{LDA}} + E_{ee} - E_{dc} \quad (2.10)$$

where E_{ee} denotes the electron-electron interaction energy and E_{dc} must be chosen such that it cancels the double-counting of the electron-electron interaction energy already included in E_{LDA} . The important difference of the LDA+U scheme compared to the simple LDA is due to the fact that the two extra functionals E_{ee} and E_{dc} do not depend on the charge density but are functionals of the orbital occupation matrices

$$n_{m,m'}(l) = \sum_{\mu} \int f(\mu - e_F) \langle lm | \phi_{\mu} \rangle \langle \phi_{\mu} | lm' \rangle dV, \quad (2.11)$$

where f denotes the Fermi-distribution and e_F the Fermi energy. Eq. (2.11) contains a projection of the wavefunction onto some localized wavefunction ϕ of state μ with some defined orbital quantum numbers l, m . The LDA+U is generally applied to only localized states of a single l quantum number. The projection on the function

$|lm\rangle$ shows that the LDA+U can be understood best from the atomic limit and the two extra functionals E_{ee} and E_{dc} can be defined from this point of view. Practically speaking, the functionals are defined by using empirical parameters, called U and J such that the desired band-splitting is obtained [SLP99], however the parameters can in principle also be determined in an extended self-consistency procedure [SD94, DBZA84] to avoid external parameters in an otherwise ab-initio calculation.

Chapter 3

Concepts of Electronic Transport

Calculating the electronic current flowing in a system due to the application of a bias voltage is one of the most difficult problems in solid state physics. Different levels of theories have been applied to the problem and many different aspects of the problem have already been discussed.

One of the most well-known method to treat electronic transport in solids is based on the Boltzmann equation, which describes the time-dependent change in the distribution function due to the applied field. Very often, the Boltzmann equation is used in the so called relaxation-time approximation, assuming a simple linear dependence of the scattering rate of the conducting electrons on the distribution function that can be expressed in terms of a characteristic scattering time. This is a simple approximation of the inelastic processes which have to be considered in a theoretical description of so called diffusive transport in large structures.

A more basic approach to the problem of electric conductance uses the idea of treating the current as a response of the system to the applied electric field. In its most rigorous formulation this idea can be used in the linear response limit in which one assumes that the current depends linearly on the field. Using the corresponding time-dependent quantum mechanical formulation one obtains the so called Kubo formalism which can be used to obtain the conductance of the system. While this approach is very general, it is not always easy to apply to realistic systems. It can be applied to the diffusive transport regime as described by the Boltzmann equation as well as in the ballistic transport regime, in which only elastic scattering is considered. This ballistic regime is of importance in atomic scale nanostructures much smaller than the electron mean-free path.

In the following, I will concentrate on two different models to describe the ballistic electron transport. One, the Landauer approach, is well known from applications

in mesoscopic physics and allows an interesting, widely applicable and intuitive approach linking conductance and transmission, while the other, the Bardeen approach, is more specific to the tunneling regime of transport governed by very low conductances.

3.1 Basic Considerations

The transport process is actually a complicated many electron problem of a system in non-equilibrium. On the macroscopic scale one can already define some of the different quantities describing the system like current and charge density or the applied electric field. However, it is very difficult to trace these quantities down to the microscopic scale due to the complicated thermodynamical averaging taking place. On the other hand, even the very microscopic view of transport contains many important physical processes which are hard to describe. Concluding, a proper theoretical approach to the transport problem would include many different effects on very different length and timescales. In the following I will only deal with the very restricted subset of phenomena that are due to the quantum mechanical nature of the electrons and I will therefore consider systems which can be described by pure wavefunctions without any statistical averaging. Still, in this picture one would have to describe the electron transport by the time-dependent many-body wavefunction $\Psi(t)$. For example one could consider the probability $P_{i,f}$ of the system changing its state from some initial multi-electron state Ψ_i into a final multi-electron state Ψ_f where the two states differ with respect to their charge distribution. Thus, this approach makes it necessary to calculate the time-dependent many particle wavefunctions of the entire system. This is a very difficult task which cannot be solved in general.

To overcome this fundamental obstacle I will switch to the single-electron picture of electron transport. Similar to replacing in density functional theory the many particle problem of determining the ground state of a many-body quantum mechanical system by an single particle Kohn-Sham formalism I will treat the electronic transport as due to the transport of many independent single-electrons. Furthermore, I will assume that the single particle states in the Kohn-Sham formulation actually describe these independent single-electrons. Of course there can be no hope that this very simplistic model actually is able to catch all the essential physics of the transport process. However, again analogous to standard band-structure calculations of solids in equilibrium in which in many cases the Kohn-Sham single particle eigenvalues and states can be successfully interpreted as the elementary excitations

of the systems I will apply the same procedure to the electronic transport and assume that the effects of the atomic arrangement, of the electronic (self-consistent) charge density and single particle potential on the current can actually be modeled by this approach.

Many effects restrict the validity of the single-electron approach. Most obvious might be electron-electron scattering effects of different conducting electrons, but also interactions with the lattice beyond the static approximation, i.e. electron-phonon scattering, screening and charging effects or many particle interactions in magnetic systems might limit the validity of the single electron picture. Only if these processes are sufficiently weak, one can hope that the single particle approximations in terms of the Kohn-Sham states will provide reasonable results. In this case one can define an average length, the coherence length, between the occurrence of such processes. In the single particle picture the description in terms of the Kohn-Sham wavefunction will hold only on length scales shorter than this length scale, since these processes not included in the model will lead to the scattering destroying the phase coherence between the single-electron states involved.

Summarizing, single-electron transport will first be described within length scales much shorter than the phase coherence length. In this regime the electrons are considered to be well described by the Kohn-Sham eigenstates of the system. Consequently, the electron will *not* change its energy during the transport process. This view of the electron transport will be called ballistic transport.

3.2 The Landauer Approach

Landauer [Lan57] proposed a theory of the transport process which is well adapted to describe the ballistic transport. A very intuitive and simple derivation will be presented here. The Landauer equation can also be derived more rigorously starting from linear response theory. In the Landauer approach to transport one considers the region Ω in which the electrons travel ballistically to be attached to two reservoirs L and R (see Fig. 3.1).

The conductance Γ of the region Ω is defined by the current I_{LR} divided by the potential difference between the two reservoirs. The current I_{LR} on the other hand is given by the current due to all electrons traveling from L to R minus the current due to the electrons traveling vice versa

$$I_{LR} = I_{L \rightarrow R} - I_{R \rightarrow L}. \quad (3.1)$$



Figure 3.1: Basic setup of the Landauer approach to transport. The reservoirs are assumed to be in thermal equilibrium.

To arrive at an equation for these currents, one can start with a simple one-dimensional model. The current from the left to the right is determined by all electrons leaving the left reservoirs, entering the scattering region Ω , and leave this scattering region by passing into the right reservoir. If one now assumes a very simple picture of the region Ω in which its electronic structure is described by single band in which states with $k > 0$ propagate from the left to the right the current is given by an integral over all states with $k > 0$ up to the Fermi wave-vector k_F

$$I_{L \rightarrow R} = \int_0^{k_F} ev(k)dk, \quad (3.2)$$

where v denotes the group velocity of the state. Since

$$v = \frac{1}{\hbar} \frac{\partial E}{\partial k} \quad (3.3)$$

and converting the integral over k into an energy integration using the density of states $n(E)$,

$$\begin{aligned} I_{L \rightarrow R} &= \int_0^{\mu_L} \frac{e}{\hbar} \frac{\partial E}{\partial k} n(E) dE \\ &= \int_0^{\mu_L} \frac{e}{\hbar} \frac{\partial E}{\partial k} \frac{1}{\partial E / \partial k} \frac{1}{2\pi} dE \\ &= \int_0^{\mu_L} \frac{e}{\hbar} dE = \frac{e}{\hbar} \mu_L, \end{aligned} \quad (3.4)$$

where the energy integration has to be performed over all energies up to the Fermi energy (the chemical potential) of the left reservoir. This can be understood from the requirement that the electrons were assumed to be incoming from the left and therefore must be occupied in the reservoir.

Using the same derivation for the states incoming from the right reservoir one obtains

$$I_{LR} = \frac{e}{h}(\mu_L - \mu_R). \quad (3.5)$$

Identifying the difference in the chemical potentials μ_L and μ_R with the applied voltage $eV = (\mu_L - \mu_R)$ one obtains the following interesting equation for the conductance

$$\Gamma = \frac{I_{LR}}{V} = \frac{e^2}{h}. \quad (3.6)$$

This equation is truly remarkable since it states that each conducting band contributes the same to the conductance. Irrespective of the density of states or the group velocity of the conducting states the conductance is always given by the fundamental quantum of conductance $\frac{e^2}{h}$. Indeed, as Eq. (3.4) shows, states with a low velocity and therefore a low current $j = ev$ are compensated by their higher density of states such that the conductance remains constant.

In the case of multiple bands, the derivation has to be modified by the inclusion of an extra sum over the different bands. Such a summation also has to be performed in the case of the three dimensional interface in which different bands for different parallel components of the wave-vectors are present. Therefore, in the general case of N conducting bands one obtains

$$\Gamma = \frac{e^2}{h}N. \quad (3.7)$$

The different „bands“ in this discussions are usually called „channels“. The argumentation presented so far did not care about the proper definition of these channels. These were simply assumed to form some kind of „band“ within Ω described by the usual formalism of a wave-vector \vec{k} and a dispersion relation $E(\vec{k})$. Strictly speaking, since the system is not periodic, one cannot speak of Bloch states with some wave-vector having a component k in the direction of the current.

Obviously a key point in the discussion was the preparation of a state traveling from inside the reservoirs through the region Ω . Therefore one should clarify this idea here. For such a state traveling to the right, one might assume the typical scattering problem. Inside the left reservoir one considers a wavefunction being a Bloch state propagating towards the region Ω . „Propagate towards“ in this context should be understood as a state having a current flowing towards Ω . Within the reservoirs the resulting scattering state can be written in terms of reflected ψ_r and transmitted ψ_t states with the same energy as the incoming state ψ_{in} . These are all solutions of the bulk Schrödinger equation describing the reservoirs. The \vec{k} values of these

transmitted and reflected states have to be chosen such that the states „propagate away“ from Ω .

$$\psi(\vec{r}) = \begin{cases} \psi_{\text{in}}(\vec{r}) + \sum_n r_{\text{in},n} \psi_r^n(\vec{r}) & , \vec{r} \text{ in left reservoir} \\ \sum_{n'} t_{\text{in},n'} \psi_t^{n'}(\vec{r}) & , \vec{r} \text{ in right reservoir} \end{cases} \quad (3.8)$$

Where, for the time being the summations can be considered to be performed over all reflected Bloch states or all transmitted Bloch states. The complex coefficients r and t are called reflection and transmission coefficients, respectively. Later on, a similar expansion will be extended to include also states decaying away from the interfaces into the reservoirs. However, since these do not carry any current and by shifting the interface far enough into the reservoirs one can eliminate these decaying states.

Looking back to the derivation of the Landauer formula, an important change has to be made. While in Eq. (3.2) and Eq. (3.3) the summation over the incoming states and the evaluation of the current from their group velocities were all performed within the same single band picture, now one has to distinguish more carefully. The k integration in Eq. (3.2) has to be performed over the „in“ label of the expansion in Eq. (3.8) corresponding to different incoming perpendicular components of the total \vec{k} -vector. The sum over the velocities on the other hand is best performed in the right electrode. This is possible since current is conserved and can be very easily be carried out if all transmitted states and the incoming state are normalized to carry unit current. Using the orthogonality of the Bloch states one can perform the same steps as in Eq. (3.1) to (3.5) again to derive the more general Landauer equation for ballistic transport in the presence of some scattering of the incoming electrons,

$$\Gamma = \frac{e^2}{h} \sum |t_{ij}|^2, \quad (3.9)$$

where i, j label the Bloch states in the reservoirs traveling from the left to the right.

Eq. (3.9) allows a simple interpretation of the transport in terms of the underlying quantum mechanical property of the transmission probability $P_{ij} = |t_{ij}|^2$ of an electron from the incoming Bloch state i into the transmitted Bloch state j . This interpretation makes the requirement of normalizing the incoming and transmitted Bloch states to unit current very clear, since in this normalization the direct interpretation of this probability is reasonably well defined and Eq. 3.9 can be seen as a simple generalization of Eq. 3.7.

3.3 Interpretation of the Landauer Formula

The Landauer formula Eq. (3.9) was the source of some confusion for quite some time after its first formulation [Büt86, SS88]. The most striking feature of the equation might be its limit for a perfectly transmitting region, i.e. for a region with $P_{ij} = |t_{ij}|^2 = 1$ for some set of i, j . For example if one would consider a perfect bulk crystal sandwiched between reservoirs of the same bulk material the expansion of Eq. (3.8) would collapse to

$$\psi(\vec{r}) = \begin{cases} \psi_{\text{in}}(\vec{r}) + \sum 0\psi_r & , \vec{r} \text{ in left reservoir} \\ 1 \psi_t = \psi_{\text{in}}(\vec{r}) & , \vec{r} \text{ in right reservoir} \end{cases} , \quad (3.10)$$

and one would rediscover Eq. (3.7) with N denoting the number of incoming Bloch states. At first glance, this means that the Landauer equation predicts a limited conductance of a system without any decoherent scattering, i.e. of a perfect bulk crystal. In the same way the Landauer equation would also give a finite conductivity of a free electron gas. This stimulates the following obvious question: How can a region with ballistic transport, i.e. without any dissipative processes, have a finite conductance? Since there is a voltage drop over the region and a current is flowing, some energy must dissipate. The key to the answer to this question lies in the definition of the reservoirs which were assumed to be in thermal equilibrium with some chemical potential μ attached to them. This is only possible, if there are actually dissipative processes in the reservoirs leading to the „thermalization“ of the „hot“ electrons being transferred across the region of ballistic transport.

The surprising result of a finite conductance in the case of a perfect crystal can now be interpreted in different ways: Either the setup described was not correct, since the reservoirs could not remain in thermal equilibrium being at the same time perfect crystals like the region of ballistic transport or, which is actually very much the same, no finite voltage can be applied across such a system. The finite conductance of such a system with perfect ballistic transmission can now be interpreted as due the finite resistance at the interface between the reservoir and the ballistic region. This is also called the Sharvin-resistance of the system.

Another point worth mentioning in the discussion of the physical significance of the Landauer equation is its formulation in terms of a two-terminal device. Both the current and the voltage drop are defined between the same two reservoirs. In many experiments, especially in mesoscopic physics a four point measurement is performed in which the current is driven between electrodes different than those between the voltage drop is measured. Büttiker [Büt86] presented a generalization

of the Landauer equation to these multi-terminal case. All problems discussed in this thesis take place on the atomic scale and therefore multi-terminal arrangements are not the typical experimental arrangement and thus Eq. (3.9) will be sufficient.

While the Landauer equation is valid in many cases reaching from systems with high conductivity to systems in the tunneling regime, in some instances one has to be careful in its application. Only states in which the incoming and transmitted waves can be described by Bloch states contribute to the tunneling current. This excludes the contribution of any state localized within the region of ballistic transport. This corresponds to the fact that these states do not carry any current within the simple one electron picture of transport chosen. In reality, there exist processes beyond this picture which lead to some coupling of these localized states to the otherwise orthogonal Bloch states in the reservoirs. For example the many-body electron-electron interaction, electron-phonon scattering, or structural defects not included in the description can provide such a coupling. Thus, while the Landauer approach will be correct for cases of high transmission through Bloch states, one could imagine that in the limit of a very low transmission probability other processes of transport across the ballistic region become important. In the one electron picture these processes could be thought of as the transition of an electron from the reservoirs into some localized state of the reservoir, the transition of the electron from one side of the reservoir to the other and than the transition of the electron into a state of the other reservoir. The validity of the Landauer model is now limited by the transmission probability between the reservoir states and the localized state. If this probability becomes comparable to the probabilities $P_{ij} = |t_{ij}|^2$ the Landauer equation breaks down.

On the other hand, one can of course treat the other limit in which the transition probability between the two sides of the reservoir becomes very small and the many-body processes needed to couple the states can be neglected. This limit can be successfully described by theories for the quantum mechanical tunneling process.

3.4 The Bardeen Approach to Tunneling

The following description of the tunneling process is based on Bardeen's approach to tunneling which first applies time dependent perturbation theory to the problem and then makes some additional approximations. Fig. 3.2 shows the tunneling setup used in this approach. Two semi-infinite crystals are separated by a barrier region, which will be assumed to be a vacuum barrier for simplicity. If this vacuum barrier is

sufficiently high and wide one can think the total setup to consist of two independent systems: one at the left (L) and one at the right (R) side.

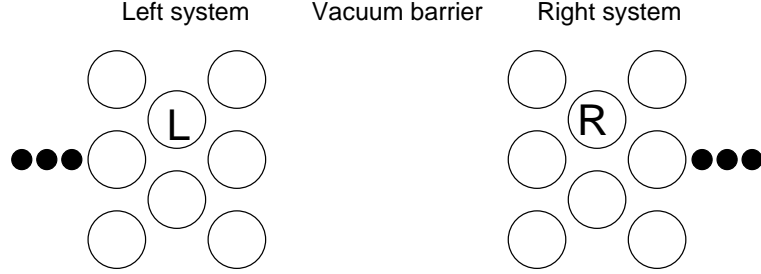


Figure 3.2: Tunneling setup used in Bardeen's approach to transport. The two semi-infinite crystals at the left and the right are separated by a vacuum barrier.

This total separation of the systems leads to two independent Schrödinger equations for the two sides

$$\begin{aligned} (T + U_L)\psi_L &= \epsilon_L\psi_L, \\ (T + U_R)\psi_R &= \epsilon_R\psi_R, \end{aligned} \quad (3.11)$$

where T denotes the operator of the kinetic energy of a single electron and U_L and U_R are the potentials of the left and right system, respectively. The single particle wavefunction $\psi(t)$ of the entire setup is determined by the total Hamiltonian $H = T + U_L + U_R$.

Now one can apply time dependent perturbation theory to describe the tunneling of an electron from across the vacuum barrier. Tunneling from the left to the right is assumed. The opposite situation of an electron tunneling vice versa may be treated completely analogously. The initial state of the tunneling process is localized in the left system. Therefore, there exists an eigenstate ψ_L^μ with $|\psi(t \rightarrow -\infty)\rangle = |\psi_L^\mu\rangle$. The time dependence of the state $|\Psi(t)\rangle$ is governed by the Hamiltonian of the whole system.

$$i\hbar\frac{\partial}{\partial t}|\psi(t)\rangle = H|\psi(t)\rangle. \quad (3.12)$$

The tunneling probability is given by the overlap of this time-dependent wavefunction with a wavefunction $|\psi_R^\nu\rangle$ of the right system. Multiplying Eq. (3.12) from the left with $\langle\psi_R^\nu|$ leads to

$$\langle\psi_R^\nu|\left(i\hbar\frac{\partial}{\partial t}\right)|\psi(t)\rangle = \langle\psi_R^\nu|H|\psi(t)\rangle. \quad (3.13)$$

Using the Schrödinger equation for the right state one obtains

$$\begin{aligned} i\hbar \frac{\partial}{\partial t} \langle \psi_R^\nu | \psi \rangle &= \langle \psi_R^\nu | H | \psi \rangle - \langle \psi_R^\nu | H_R | \psi \rangle \\ &= \langle \psi_R^\nu | U_L | \psi \rangle . \end{aligned} \quad (3.14)$$

Substituting $|\psi(t \rightarrow -\infty)\rangle = |\psi_L^\mu\rangle$ for $|\psi\rangle$ at the right hand side of Eq. (3.14) leads to first order perturbation theory

$$i\hbar \frac{\partial}{\partial t} \langle \psi_R^\nu | \psi \rangle = \langle \psi_R^\nu | U_L | \psi_L^\mu \rangle . \quad (3.15)$$

Even though this equation looks familiar one has to emphasize that this is not a result obtained by standard time-dependent perturbation theory. The states $|\psi_L\rangle$ and $|\psi_R\rangle$ are eigenstates of two a priori different Hamiltonians H_L and H_R , respectively. Therefore, these eigenstates do not form a complete orthogonal basis of the eigenspace of the total Hamiltonian $H = T + U_L + U_R$ and the matrix elements at the left side of Eq. (3.15) are not sufficient to determine the complete time dependence of $|\psi\rangle$. This is a basic weakness of Bardeen's approach. However many applications [HBP⁺98, HAB⁺99, VSB⁺97, LYB⁺99] of this formalism have shown that Bardeen's approximation produces reliable results for systems which are well separated, i.e. systems where the overlap of the two wavefunctions ψ_R and ψ_L is small.

Since the potential U_L is not small in the left region, the question arises whether one is allowed to use perturbation theory at all. However, it can be seen from Eq. (3.15) that the quantity which in fact determines the strength of the perturbation of the initial state is $\langle \psi_R^\nu | U_L | \psi_L^\mu \rangle$. Since the final wavefunction $|\psi_R\rangle$ is localized in the right region in which the left potential U_L is very weak this perturbation might still be regarded as a small perturbation and thus time depended perturbation will lead to reasonable results.

By separating the time-dependence of the states $|\psi_L^\mu\rangle = e^{\frac{i}{\hbar}\epsilon_\mu t} |\Psi_L^\mu\rangle$ and $|\psi_R^\nu\rangle = e^{\frac{i}{\hbar}\epsilon_\nu t} |\Psi_R^\nu\rangle$, integrating Eq. (3.15) and performing the limit $t \rightarrow \infty$, one obtains an expression for the tunneling-probability per time interval

$$P_{\mu\nu}^{LR} = \lim_{t \rightarrow \infty} \frac{1}{t} \frac{1}{\hbar^2} \int_0^t |\langle \psi_R^\nu | U_L | \psi_L^\mu \rangle|^2 \quad (3.16)$$

$$= \lim_{t \rightarrow \infty} 4\hbar \frac{\sin^2\left(\frac{\epsilon_\nu - \epsilon_\mu}{2\hbar} t\right)}{(\epsilon_\nu - \epsilon_\mu)^2} |M_{\mu\nu}^{RL}|^2 , \quad (3.17)$$

where the matrix element $M_{\mu\nu}^{LR}$ is given by the stationary-state matrix element of

the potential

$$M_{\mu\nu}^{LR} = \langle \Psi_R^\nu | U_L | \Psi_L^\mu \rangle. \quad (3.18)$$

Assuming a continuous range of energy levels ϵ_μ (or ϵ_ν) the limit of Eq. (3.17) can be evaluated directly [Sch93]. One obtains

$$P_{\mu\nu}^{LR} = \frac{2\pi}{\hbar} \delta(\epsilon_\nu - \epsilon_\mu) |M_{\mu\nu}^{LR}|^2. \quad (3.19)$$

This result is similar to the well known 'Golden Rule' Fermi obtained for standard time-dependent perturbation theory. It describes elastic tunneling with energy $\epsilon_\nu = \epsilon_\mu$ only. Formally the energy conservation is taken care of by the δ -function in Eq. (3.19).

To evaluate this matrix element Bardeen introduced an additional approximation. He assumed the potential U_L to be zero in the right region of space. Similar the right potential should be zero in the left region. More formal he introduced a separation surface S which separates the regions in which the two potentials differ from zero. This can be formulated by the condition $U_L U_R = 0$ for any point in space. Figure 3.3 shows the setup as used in this additional approximation.

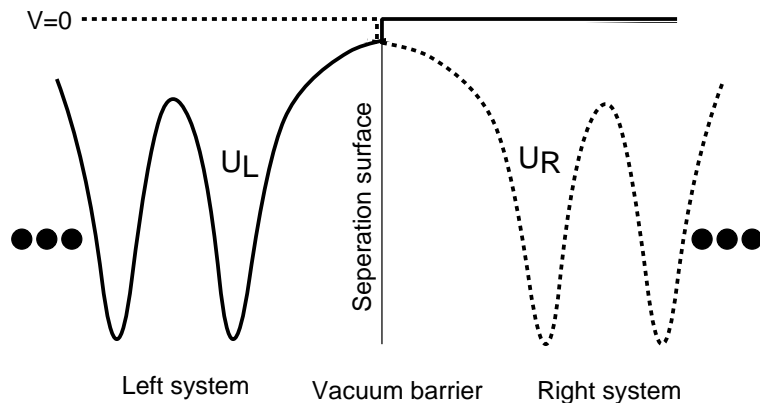


Figure 3.3: Potential used in the Bardeen approach to tunneling. The left (right) potential U_L (U_R) is then assumed to be zero in the right (left) region.

Of course, this approximation will become better if the potentials U_L and U_R are reasonably small at and beyond the separation surface. This will be the case if the separation surface is located far out in the vacuum. Therefore, one will expect that Bardeen's approximation is valid for tunneling processes through a wide barrier while the results of this approach will become invalid for very small distances.

Using the Schrödinger equation for the left wavefunction and having in mind that the potential U_L is zero in the right space one can now rewrite the matrix element

as an integral over the left region only

$$M_{\mu\nu}^{LR} = \int_L \Psi_R^\nu(\vec{r})^* (\epsilon_\mu + \frac{\hbar^2}{2m} \vec{\nabla}^2) \Psi_L^\mu(\vec{r}) dV \quad (3.20)$$

which can be written in a more symmetric form

$$\begin{aligned} M_{\mu\nu}^{LR} &= \int_L \left\{ \Psi_R^\nu(\vec{r})^* \epsilon_\nu \Psi_L^\mu(\vec{r}) + \Psi_R^\nu(\vec{r})^* \frac{\hbar^2}{2m} \vec{\nabla}^2 \Psi_L^\mu(\vec{r}) \right\} dV \\ &= \int_L \left\{ \Psi_R^\nu(\vec{r})^* \overleftarrow{(T + U_R)} \Psi_L^\mu(\vec{r}) + \Psi_R^\nu(\vec{r})^* \frac{\hbar^2}{2m} \vec{\nabla}^2 \Psi_L^\mu(\vec{r}) \right\} dV \\ &= -\frac{\hbar^2}{2m} \int_L \left\{ \Psi_R^\nu(\vec{r})^* \vec{\nabla}^2 \Psi_L^\mu(\vec{r}) - \Psi_R^\nu(\vec{r})^* \vec{\nabla}^2 \Psi_L^\mu(\vec{r}) \right\} dV \end{aligned} \quad (3.21)$$

In these transformations at first the eigenvalue ϵ_μ was substituted by ϵ_ν because energy conservation requires the calculation of matrix elements with $\epsilon_\mu = \epsilon_\nu$ only. In the second step the Schrödinger equation for the right state was used (the arrow indicates on which wavefunction the operators acts). The integration area is the left region. Since the potential U_R is assumed to be zero in this region, it was dropped in the last step. Using Greens theorem and the boundary condition that the right wavefunction is zero at infinite distance from the separation surface, this integral can be transformed into an integral over the separation surface

$$M_{\mu\nu}^{LR} = -\frac{\hbar^2}{2m} \int_S \left(\Psi_L^\mu(\vec{r}) \vec{\nabla} \Psi_R^\nu(\vec{r})^* - \Psi_R^\nu(\vec{r})^* \vec{\nabla} \Psi_L^\mu(\vec{r}) \right) dS. \quad (3.22)$$

So far only an expression for the probability of the transition of an electron from a left state into a right state was obtained.

To account for a finite bias voltage V applied between the two sides an additional term eV is introduced modifying Eq. (3.19) slightly. This probability can then be written as

$$P_{\mu\nu}^{LR} = \frac{2\pi}{\hbar} \delta(\epsilon_\mu^L - \epsilon_\nu^R - eV) |M_{\mu\nu}^{LR}|^2. \quad (3.23)$$

To calculate the tunneling current one has to sum over all different possible left and right states and one has to keep in mind that the electrons might tunnel from the left to the right as well as vice versa. The total current therefore is given by

$$\begin{aligned} I &= I^{L \rightarrow R} - I^{R \rightarrow L} \\ &= e \sum_{\mu\nu} f(\epsilon_\mu) (1 - f(\epsilon_\nu + eV)) P_{\mu\nu}^{LR} - e \sum_{\mu\nu} (1 - f(\epsilon_\mu)) f(\epsilon_\nu + eV) P_{\nu\mu}^{RL} \\ &= e \sum_{\mu\nu} (f(\epsilon_\mu) - f(\epsilon_\nu + eV)) P_{\mu\nu}^{LR} \end{aligned} \quad (3.24)$$

where $f(\epsilon)$ denotes the Fermi-distribution function which is introduced to ensure that only tunneling from occupied to unoccupied states can occur. In Eq. (3.24) the symmetry of the tunneling probability $P_{\mu\nu}^{LR} = P_{\nu\mu}^{RL}$ which can easily be deduced from Eq. (3.22) was used. The sum in Eq. (3.24) has to be performed over all right states labeled by ν and all left states labeled by μ . No further assumption is made on the nature of these left and right states, i.e. both Bloch states and surface states decaying into the bulk contribute to the current. Therefore, this formula differs significantly from the Landauer formula.

3.5 Experimental Setups

This chapter will close with a short presentation of two major experimental setups in which transport phenomena on the atomic scale become important and which can be investigated by the Landauer and the Bardeen approach.

3.5.1 Scanning Tunneling Microscope

Since its invention by Binnig and Rohrer in 1982 [GBW82] the Scanning Tunneling Microscope (STM) has become a frequently used tool in surface science. Its setup basically consists of a sharp metal tip which in the ideal case has only a single apex atom, i.e. it is mono-atomically sharp (Fig. 3.4). Using piezo-crystals this tip can be moved in all three dimensions on a 0.01 \AA scale. If the tip is moved close to the

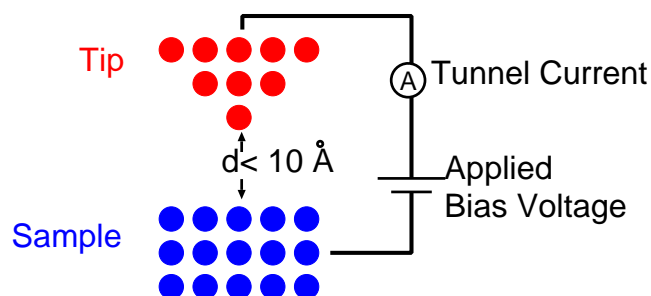


Figure 3.4: Setup of an STM.

sample (up to a distance in the range of a couple of \AA only) electrons can tunnel through the vacuum barrier from the tip into the surface and vice versa. In the case of a conductive sample material and with an applied bias voltage this effect can lead

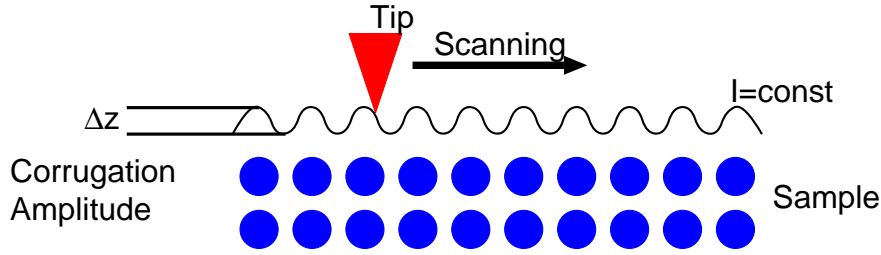


Figure 3.5: Constant-current mode. The tip is scanned along the line of constant tunneling current. This leads to a corrugation of the tip position with a corrugation amplitude Δz .

to a current of electrons tunneling between the systems. This current is the basic quantity measured in an STM experiment.

Two different modes of operation of the STM are frequently used: First, one can scan the tip position over the surface and obtain a two-dimensional map of the tunneling current. In practice, this mode is normally realized by keeping the current fixed and by varying the tip-sample distance d accordingly (Fig. 3.5). This so called constant-current mode ensures that the tip does not touch the surface while being scanned over the sample. The experimental quantity measured in the constant-current mode is no longer the tunneling current but the corrugation of the tip. A characteristic outcome of such measurements is the corrugation amplitude (Fig. 3.5). This quantity is defined as the difference between the largest and smallest tip-sample distance in a constant current experiment. Due to the exponential dependence of the tunneling current on the width of the barrier, i.e. of the tip-sample distance, this experimental setup allows a high resolution vertical to the surface. Combined with the high accuracy of the positioning of the tip parallel to the surface, images with an extremely high resolution can be obtained. Steps and islands can be mapped easily and if the experimental setup is stable enough one can reach atomic resolution with this method. In these STM images with atomic resolution, single ad-atoms on a surface and single defects can be observed.

The second main mode of operation of an STM is the spectroscopy mode in which for a chosen tip position the differential conductivity dI/dV for variable bias voltages V are measured and recorded. This mode allows a local investigation of the electronic structure.

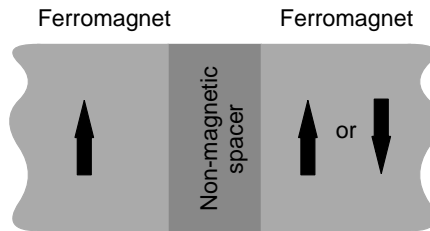


Figure 3.6: Setup of a magnetic junction. The two ferromagnetic electrodes are separated by a non-magnetic spacer and might be ferromagnetically or antiferromagnetically aligned.

3.5.2 The Junction-Magneto-Resistance

In the last several years the investigation of spin-dependent transport through magnetic junctions became a big issue in both fundamental solid state research and applied research. Following the discovery of the giant magneto resistance (GMR) effect many other kinds of junction magneto resistance phenomena have been discovered and investigated. The basic setup of these experiments is shown in Fig. 3.6. A magnetic junction is constructed out of a two-dimensional multilayer system of different materials. In general, two ferromagnetic (FM) layers are separated by some non-magnetic (NM) spacer. In practice, one often has to include more than those three different layers and a complicated multi-layer stacking is used to control the magnetic properties of the ferromagnetic layers for example in so-called exchange bias systems, or to allow better epitaxial growth, or to include contacts and anti-corrosion protection. In this work the theoretical description will be restricted to the simple setup of two semi-infinite electrodes and a spacer. Recent progress in experimental preparation techniques, especially the development of the molecular beam epitaxy made it possible to build such devices on the nanoscale with spacer thicknesses in the range of a few atomic layers. However, still many of these junctions exhibit a large amount of roughness or alloying at the interface and very often the spacer is amorphous.

The perpendicular conductance of such a magnetic multilayer depends on the relative orientation of the two ferromagnets. With R_{AF} and R_{FM} denoting the corresponding resistances in anti-ferromagnetic and ferromagnetic alignment of the two FM electrodes, one defines the ratio

$$JMR = \frac{\Delta R}{R} = \frac{R_{AF} - R_{FM}}{R_{AF} + R_{FM}} \quad (3.25)$$

as the junction magneto-resistance (JMR). Sometimes the so called „optimistic“

definition of

$$JMR_+ = \frac{R_{AF} - R_{FM}}{\min(R_{AF}, R_{FM})} \quad (3.26)$$

can also be found. In agreement with these definitions and as in general the resistance of the ferromagnetically aligned junction is lower, than that of the antiferromagnetically aligned, it is custom to speak of a negative JMR if the antiferromagnetically aligned junction shows a higher conductance.

Depending on the kind of spacer layer one can speak of different effects. The GMR occurs in FM/NM/FM metallic multilayers like Co/Cu/Co. Since some years, the production of these junctions is of big technological interest. Many different kind of sensors have been engineered in which an external magnetic field is detected by its influence on the magnetization direction of one of the FM layers. Today, these sensors are the state of the art technology in read-heads of magnetic hard disks.

While the GMR effect is based on the spin-dependend transmission of electrons through different metallic layers, one can also replace the spacer layer by a non-magnetic insulating material. In ideal realizations the electrons only tunnel across the junction and consequently one speaks in such systems of tunnel magneto resistance (TMR). In contrast to the GMR systems which show a very high conductance, these TMR systems have a very low conductance because of the low transmittance of the electrons through the tunnel barrier. The exponential decrease of the transmission probability in the tunneling process makes it necessary to produce even thinner barriers. This imposes a severe problem in the comparison of experimental results with the calculations presented here since very often the actual tunnel barrier is very hard to control experimentally.

Another choice of barrier material might be a semiconductor. In this case one generally speaks of processes like spin-injection to describe the formation of current of spin-polarized electrons passing from the ferromagnet into the semiconductor. Many problems like the conductivity mismatch [SFM⁺00] between metallic FM electrodes and the semiconductor NM spacer, the formation of Schottky barriers, the possibility of building spin-transistors or the possible use of FM semiconductors as electrodes have been investigated both experimentally and theoretically in these systems.

The multilayer setup as introduced in Fig. 3.6 can be employed in different ways in transport measurements. The most simple setup is a single junction with the current driven perpendicular through the spacer. This is the so called current-perpendicular to plane (CPP) setup [Fig. 3.7a)] and the one which will be assumed in all calculations to follow. It is the typical setup for TMR systems and spin-injection systems. Since in TMR-elements the transmission of the tunneling barrier

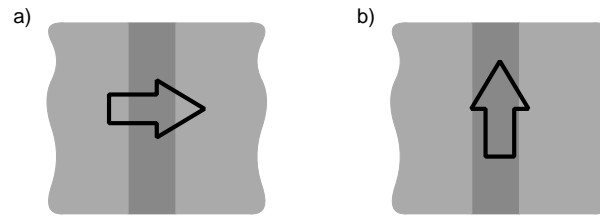


Figure 3.7: Two orientations of the junction with respect to the current. The current may either flow perpendicular to the junction (a) or parallel to it (b).

is quite small only single junctions are made. In contrary, the voltage drop in GMR-elements being all metallic is very small and typically the current in-plane (CIP) geometry [Fig. 3.7b)] is used. In this setup the current is flowing parallel to the planes. The difference in the transmission through the interfaces can be interpreted as additional scattering at these planes. In a model of diffusive transport this leads to junction magneto-resistance.

Chapter 4

Green Function Embedding

This chapter will introduce the formalism of “Green function embedding” following the original prescription of J. Inglesfield [Ing81]. I will discuss how to calculate the Green function of interfaces sandwiched between two semi-infinite bulk electrodes. This geometry will also be used in the transport setups discussed later on. Only the basic equations and ideas will be discussed, all details due to the actual implementation will be postponed to chapter 6. For convenience the formulas will be presented in atomic units with $\hbar = c = 1$.

4.1 The Embedding Problem

Most standard *ab-initio* methods used in solid state physics are developed for the calculation of bulk properties. In this case one can employ the very powerful “Bloch theorem” to restrict the problem to a single unit-cell with periodic boundary conditions (see e.g. [AM76]). According to the Bloch theorem the wavefunction can be written as

$$\Psi_{\vec{k}}(\vec{r}) = e^{i\vec{k}\vec{r}} u_{\vec{k}}(\vec{r}), \quad (4.1)$$

with the function $u_{\vec{k}}(\vec{r})$ having the Bravais periodicity. Since the potential $V(\vec{r})$ has the same periodicity one can reformulate the Kohn-Sham equation to

$$\left(-\frac{1}{2}(\vec{\nabla} + i\vec{k})^2 + V(\vec{r}) \right) u_{\vec{k}}(\vec{r}) = \epsilon u_{\vec{k}}(\vec{r}) \quad (4.2)$$

and solve the equation for $u_{\vec{k}}(\vec{r})$ with periodic boundary condition. However, if the translational symmetry is broken this trick can no longer be used. The probably two most important cases in which such a loss of translational symmetry occurs is

the impurity problem of a localized quasi zero-dimensional impurity placed within a host crystal and the problem of two half spaces joined together. Examples for this second problem are surfaces of crystals or the two-dimensional interface between different crystals. Even though the Bloch theorem is not applicable to such systems one can take advantage of the fact that these perturbations from an ideal crystal are localized in the sense that far from the impurity or the interface the bulk properties of the crystal will be retained. In particular the charge density, the basic quantity to describe the system in DFT, differs from its bulk value only in the vicinity of the perturbation. This makes it possible to develop schemes within the framework of the DFT which are based on splitting the system into the bulk-like regions and a small perturbed region which contains the interface or impurity itself and some additional space in which the charge density will be disturbed from its bulk value. The actual size of this region of course depends strongly on the physics of the perturbation and on the actual physical processes screening the influence of the perturbation. For example charged impurities in semiconductors and metals will have a very different effects on the surrounding charge density than uncharged defects. Having identified the region in which the charge density is actually affected by the perturbation, different approaches have been developed to treat this region. Among them are the Green function methods using the Dyson equation and the supercell methods in which the perturbed region is repeated. The two-dimensional slab in the FLAPW film method, as used in the FLEUR code, can also be understood as such a restriction of the unit-cell to the space in which the potential is perturbed.

One very important point remains to be pointed out. Even though the influence of the perturbation on the charge density is restricted to some small region, the change in the wavefunctions is not! As discussed above, within a three-dimensional infinite crystal the wavefunctions can be written as Bloch states with some wave-vector \vec{k} . These states can be understood as describing electrons traveling through the crystal having some defined crystal momentum \vec{k} . If a perturbation is present, these states are no longer allowed eigenstates of the perturbed system as they do not fulfill the correct differential equation near the perturbation. One can, however, construct the correct solutions by considering the scattering problem. As the potential is undisturbed in the asymptotic limit far away from the perturbation, one can start with a Bloch like solution in this region and consider the scattering of this state at the perturbation. This procedure will in general lead to a modification of the solution in the asymptotic region as well, in which the resulting wavefunction is a linear combination of the incoming Bloch wave and scattered waves. As an easy example one might consider the case of a surface where the total reflection at the

vacuum barrier will lead to the formation of standing waves as linear combinations of the incoming and backscattered Bloch waves. The fact that this modification of the wavefunction due to the scattering is not confined within a small region around the perturbation imposes a key problem in the calculation of quantities that can not be expressed in terms of the electron density, like for example the electric current. While methods based on supercell calculations can easily obtain the charge density, they have huge disadvantages in the calculation of the current. Recently a scheme has been formulated [RZM01] which tries to overcome these drawbacks. However, it lacks generality and one has to impose severe restrictions on the system. The Green function based methods using either the Dyson equation or the embedding method to treat the perturbation on the other hand are able to reproduce not only the correct charge density but also a Green function which can be extended into whole space, which includes all information about the scattering process and which therefore can be used to construct the correct wavefunctions.

4.2 Setup

Before going into more details, the setup used in the formulation of the embedding method should be introduced. The embedding method deals with the problem of some region of space Ω (see Fig. 4.1a)), enclosed within a larger “outer” volume V_0 . The boundary surface S of the volume Ω separates the two regions of space. In all space a local potential $V(\vec{r})$ exists and the solution of the Schrödinger equation is well-behaved. We now want to solve the Schrödinger equation in region Ω such that the solution obtained is actually the constriction of a solution of the full Schrödinger equation in the whole space ($\Omega+V_0$) to the region Ω only. Of course this solution can be found by integrating the Schrödinger equation in all space, but the embedding method enables one to treat region Ω only while taking the effect of the outer volume into account through the boundary condition on the separation surface S .

While the basic equations of the embedding method can be formulated very elegantly in the setup as introduced so far, the actual application of the method will be restricted to the special case of an embedding region Ω introduced in the previous chapter, which has the shape of a slab (see Fig. 4.1b)), i.e. one assumes that Ω is infinite in two dimensions and of finite size in the third dimension. Later applications will include cases in which the slab could consist of a single layer of atoms of bulk material with two-dimensional translational symmetry, called monolayer, or of a few monolayers, forming a heterostructure or describing an interface between two semi-infinite crystals. The boundary surface S of the slab volume Ω is divided into

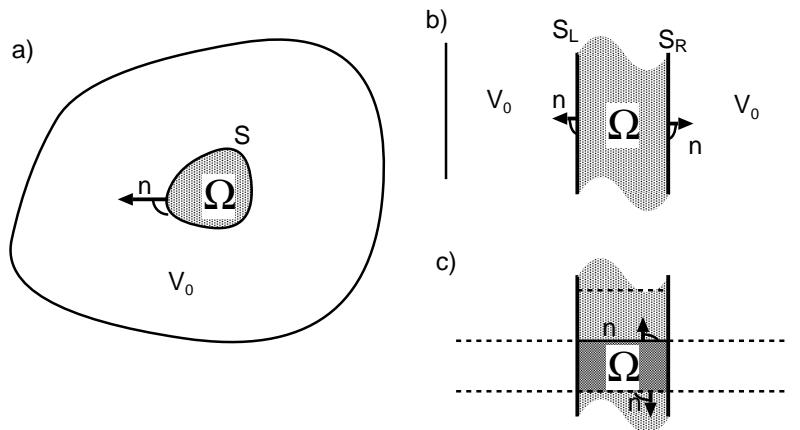


Figure 4.1: Setup used for the embedding method. (a) The region of interest is a volume Ω separated by the surface S from an outer region V_0 . Actual applications use the slab setup (b) in which Ω is infinite in two dimensions and of finite size normal to the two boundaries S_L and S_R . (c) in the slab case the calculation can be restricted to the indicated single unit-cell due to translational symmetry parallel to the boundaries. The surface normals indicated by arrows are assumed to point outwards.

two parts: the left, S_L , and the right, S_R , boundary. Throughout this chapter the indices L , R and b ($b = L$ or R) will denote quantities defined on the left, the right or either boundary, respectively. S without any index refers to both S_L and S_R . Very frequently the surface normal derivative of some function $f(\vec{r})$ will be taken on these boundary surfaces. This quantity is defined as $\hat{n}(\vec{\nabla}f(\vec{r}))$, the projection onto the surface normal vector \hat{n} . By definition, the surface normals will always be assumed to point out of the region Ω as indicated in Fig. 4.1. The operator of the surface normal derivative is usually written as $\frac{\partial}{\partial n}$, n denoting the coordinate along \hat{n} or even shorter as ∂_n .

The two different regions Ω as shown in Figs. 4.1a) and 4.1b) differ in one important aspect. While in the first definition the embedding region Ω is enclosed within the outer space V_0 and encompasses a finite volume in Ω , the slab setup is infinite. Strictly speaking, the derivation of the embedding equations given later on, which relies on the application of Green's theorem is only valid for the finite setup. However, the extension to the slab geometry is possible in the case of two-dimensional periodicity throughout the system. In this case one can apply Bloch's theorem to restrict the volume to one single unit cell parallel to the slab (Fig. 4.1c)). Because of the periodic boundary conditions on the surface of this single unit cell, and the difference in the direction of the surface normals, all contributions from the auxiliary surfaces between adjacent unit-cells vanish and one can restrict the discussion to the surfaces between the slab and the outer volume only.

4.3 The Schrödinger Equation in the Embedding Region

The Schrödinger equation is normally treated as a boundary value problem. In typical physical problems the boundary conditions the wavefunction must satisfy are well known, but the energy spectrum is not. Examples for such boundary conditions are the Bloch condition in the three-dimensional crystal which imposes periodic boundary conditions or the condition of the wavefunction decaying to zero into the vacuum for a surface calculation. However, here a region is considered which is only a very tiny part of the whole space the wavefunction Ψ is defined in. Therefore, since the energy of the state ϵ is given by $\epsilon = \int \psi^*(\vec{r}) H(\vec{r}) \psi(\vec{r}) dV / \int \psi^*(\vec{r}) \psi(\vec{r}) dV$, where the integration has to be performed over all space, the contribution from the region Ω to this integral is negligible (only delocalized wavefunctions are considered, in the case of states localized in Ω this discussion must be modified) and thus the energy can be thought of as being determined by the outside region only. Thus, the Schrödinger equation is to be solved for some given energy ϵ .

As the Schrödinger equation is a second order partial differential equation for the slab setup different kinds of conditions can now be imposed to solve this equation for fixed energy. The most simple case might be the case of the initial value problem. If one specifies both the value of the wavefunction and its normal derivative on either boundary surface, the corresponding solution is uniquely determined. While this might seem a most reasonable procedure, finding the actual solution of this problem is extremely difficult. For each energy there exist initial values for which the solutions grow or decay exponentially. Any numerical inaccuracy in describing the desired solution therefore might lead to an exponentially increasing error at the other boundary. Mathematically speaking the initial value problem of the Schrödinger equation is an ill-posed problem. Thus the straightforward integration of the initial value problem is bound to fail spectacularly and other more involved methods have been employed if one wants to solve the initial value problem [HT95]. These methods are currently most successfully applied using local pseudopotentials.

It is known to be much more stable to impose a more symmetric condition which acts on both boundary surfaces [SH88, Wac86]. Many different schemes have been developed in which different forms of conditions on the boundary surfaces have been imposed on the wavefunctions. For example the value of the solution on both boundaries or the normal derivative of the wavefunction or different combinations of these values have been used. In the following it will be shown how the embedding method of Inglesfield [Ing81, IB88] treats the problem.

4.4 Variational Principle

The starting point of the embedding method is the variational principle for the expectation value of the energy

$$E = \frac{\int \Psi^*(\vec{r}) H(\vec{r}) \Psi(\vec{r}) dV}{\int \Psi^*(\vec{r}) \Psi(\vec{r}) dV} = \min. \quad (4.3)$$

It is well known that the actual (ground state) solution of the Schrödinger equation

$$H(\vec{r}) \Psi(\vec{r}) = E \Psi(\vec{r}) \quad (4.4)$$

can be found by varying $\Psi(\vec{r})$ such that Eq. (4.3) leads to the minimal energy E and that in this sense Eq. (4.3) and Eq. (4.4) can be considered identical. In the problem of embedding one wants to deal with the small volume Ω only. Thus, the function Ψ is partitioned in the following way

$$\Psi(\vec{r}) = \begin{cases} \psi(\vec{r}) & \text{in } V_0 \\ \phi(\vec{r}) & \text{in } \Omega . \end{cases} \quad (4.5)$$

Now the variation of the function Ψ is restricted to Ω , i.e. a test function ϕ in Ω is chosen and then it is extended into V_0 by attaching a solution of the Schrödinger equation with energy ϵ to it

$$H(\vec{r}) \psi(\vec{r}) = \epsilon \psi(\vec{r}) \text{ in } V_0. \quad (4.6)$$

The function ψ can be chosen such that it fulfills the correct boundary condition at some outer boundary of V_0 (for example is Bloch-periodic) and at the same time its amplitude can be adjusted such that the total trial function Ψ becomes continuous across the interface between Ω and V_0 . However, for a general trial function ϕ it is not possible for the function Ψ to have a continuous derivative across the interface as well. As the kinetic energy operator included in $H(\vec{r})$ contains the ∇^2 operator, this leads to the appearance of an additional surface term ensuring that the Hamiltonian is hermitian

$$\begin{aligned} \int_{\Omega+V_0} \Psi^*(\vec{r}) \nabla^2 \Psi(\vec{r}) dV &= \int_{\Omega} \phi^*(\vec{r}) \nabla^2 \phi(\vec{r}) dV + \int_{V_0} \psi^*(\vec{r}) \nabla^2 \psi(\vec{r}) dV \\ &+ \int_S \{ \psi^*(\vec{r}) \partial_n \phi(\vec{r}) - \phi^*(\vec{r}) \partial_n \psi(\vec{r}) \} dS, \end{aligned} \quad (4.7)$$

which is a simple application of Green's theorem (see for example [Ing81]). The difference in sign between the two terms in the surface integral arises from the difference in the direction in the normal derivative ∂_n between the two regions Ω and V_0 .

Substituting Eq. (4.7) into Eq. (4.3) one now obtains an expression for the energy expectation value which contains volume integrals over Ω and V_0 and a term acting at the surface only

$$E = \frac{\int_{V_0} \psi^*(\vec{r})H(\vec{r})\psi(\vec{r}) dV + \int_{\Omega} \phi^*(\vec{r})H(\vec{r})\phi(\vec{r}) dV + \frac{1}{2} \int_S \{\psi^*(\vec{r}) \partial_n \phi(\vec{r}) - \phi^*(\vec{r}) \partial_n \psi(\vec{r})\} dS}{\int_{V_0} \psi^*(\vec{r})\psi(\vec{r}) dV + \int_{\Omega} \phi^*(\vec{r})\phi(\vec{r}) dV} \quad (4.8)$$

Before using the variational principle to derive a differential equation by taking the functional derivative of Eq. (4.8) with respect to the trial function ψ^* one has to consider the volume integrals over the outer volume V_0 . Inglesfield showed that these can be expressed in terms of surface integrals on the boundary surface S by using the energy derivative of the Green function [Ing81]. This approach leads to a very general equation in which the energy eigenvalue ϵ in the outer region V_0 can be determined self-consistently. Furthermore, strictly speaking the pre-defined energy ϵ and the variational energy E do not have to be the same. However, at this point one can argue that one is looking for a final solution of the Schrödinger equation in all space with some energy eigenvalue ϵ and that thus in the end $E = \epsilon$ must hold. Using this identity the volume integrals over V_0 in Eq. (4.8) can be eliminated. Using the assumed continuity $\psi = \phi$ on the surface one can vary Eq. (4.8) for ϕ^* and obtains

$$(H(\vec{r}) - \epsilon)\phi(\vec{r}) + \frac{1}{2}\delta(n - n_s) [\partial_n \phi(\vec{r}) - \partial_n \psi(\vec{r})] = 0, \quad (4.9)$$

where n denotes the normal coordinate perpendicular to the surface and n_s the position of the surface, i.e. the second term acts on the surface only. This equation looks like a modified Schrödinger equation with an additional surface term which ensures that the solution has the correct derivative at the boundary surface. However, this equation is not ready for use since the normal derivative $\partial_n \psi(\vec{r})$ is not known in advance. Furthermore, it should be stressed once again, that in Eq. (4.9) the normal derivative will be energy dependent and thus Eq. (4.9) does not define an eigenvalue problem for ϵ any more, but instead it is an equation the solution of the Schrödinger equation in Ω , which can be matched at the same energy to the solution ψ in V_0 , must fulfill.

4.5 The Embedding Potential

To overcome the problem of the unknown normal derivative $\partial_n \psi(\vec{r})$ in Eq. (4.9) one can use the Schrödinger equation in V_0 and the defining equation for the Green function G_0 in V_0

$$(H(\vec{r}) - \epsilon)\psi(\vec{r}) = 0 \quad (4.10)$$

$$(H(\vec{r}) - \epsilon)G_0(\vec{r}, \vec{r}'; \epsilon) = -\delta(\vec{r} - \vec{r}'). \quad (4.11)$$

Writing $H(\vec{r}) = -\frac{1}{2}\nabla^2 + V(\vec{r})$, multiplying Eq. (4.10) with $G(\vec{r}, \vec{r}')$, multiplying Eq. (4.11) with $\psi(\vec{r})$, subtracting the results and integrating over V_0 one obtains

$$\begin{aligned} \int_{V_0} \delta(\vec{r} - \vec{r}')\psi(\vec{r}) dV &= \\ \psi(\vec{r}') &= -\frac{1}{2} \int_{V_0} G_0(\vec{r}, \vec{r}'; \epsilon) \nabla^2 \psi(\vec{r}) - \psi(\vec{r}) \nabla^2 G_0(\vec{r}, \vec{r}'; \epsilon) dV \\ &= \frac{1}{2} \int_S G_0(\vec{r}, \vec{r}'; \epsilon) \partial_n \psi(\vec{r}) - \psi(\vec{r}) \partial_n G_0(\vec{r}, \vec{r}'; \epsilon) dS. \end{aligned} \quad (4.12)$$

Again Green's theorem has been used to convert the volume integral into a surface integral. In this step some care has to be taken because of the outer surface of region V_0 and the special shape of V_0 . In principle the surface S must include not only the boundary between the regions V_0 and Ω but also the outer boundary of V_0 . Similarly, in a slab setup Green's theorem can not be applied in the very strict mathematical sense as the region V_0 consists of two non-connected parts. In a very formal derivation one could either restrict Eq. (4.12) to one of these parts and go to the limit in which the outer surface is placed at infinite distance with vanishing ψ and $\partial_n \psi$ on it. Alternatively, one could join the two sides of V_0 at their outer boundary by some kind of a periodic boundary condition and thereby cancel the effect of the outer boundary. One might note here, that the derivation shown here requires the potential $V(r)$ in the Hamiltonian to be local. One can easily show, that this strict requirement can be slightly released. As long as the potential is local on the boundary surfaces a non-local contribution might be present [Ish97].

Eq. (4.12) can be simplified if a special Green function is used. As Eq. (4.12) holds for any boundary condition the Green function fulfills on S , one is free to use the von-Neumann condition of vanishing normal derivative

$$\partial_n G_0(\vec{r}, \vec{r}') = 0 \quad \text{on } S. \quad (4.13)$$

Putting \vec{r}' on S one obtains

$$\psi(\vec{r}_S) = \frac{1}{2} \int_S G_S(\vec{r}_s, \vec{r}_s'; \epsilon) \partial_n \psi(\vec{r}_s') dS', \quad (4.14)$$

where the notation G_S is introduced for the surface projection of the Green function G_0 . This equation can be inverted for $\partial\psi$

$$\partial_n \psi(\vec{r}_S) = 2 \int_S G_S^{-1}(\vec{r}_s, \vec{r}_s'; \epsilon) \psi(\vec{r}_s') dS'. \quad (4.15)$$

Equation (4.15) is one of the fundamental foundations of the embedding formalism. The quantity $G_S^{-1}(\vec{r}_s, \vec{r}_s'; \epsilon)$, the surface inverse of a particular Green function, was called “embedding potential” in the original paper of Inglesfield. One important interpretation is that of the embedding potential as a generalized logarithmic derivative. As seen by Eq. (4.15) it can be viewed as a linear operator acting on the value of the wavefunction on the boundary surface and returning the normal derivative of the wavefunction. This property will be used frequently in applications of the method.

4.6 The Embedded Green Function

The question of how to obtain the embedding potential in a numerical scheme will be postponed to chapter 5. Instead the focus now should return to Eq. (4.9). All quantities in this expression were defined in region Ω only. The only remaining problem in the application of this equation was the unknown normal derivative of the “external” wavefunction $\partial_n \psi(\vec{r}_S)$. Using Eq. (4.15) the derivative can now be rewritten in terms of the embedding potential and of the value of the wavefunction at the boundary surface. Since the ansatz for the trial function was a continuous function across the boundary this value of the wavefunction is equal to the value of the function $\phi(\vec{r})$ defined within Ω . Thus Eq. (4.9) can be rewritten to

$$(H(\vec{r}) - \epsilon)\phi(\vec{r}) + \frac{1}{2}\delta(n - n_s) \left[\partial_n \phi(\vec{r}) - 2 \int_S G_S^{-1}(\vec{r}, \vec{r}_s'; \epsilon) \phi(\vec{r}_s') dS' \right] = 0, \quad (4.16)$$

which can be written symbolically as

$$(H_{\text{emb}}(\epsilon) - \epsilon)\phi(\vec{r}) = 0, \quad (4.17)$$

where the Hamiltonian H_{emb} has been defined to include the normal Hamilton operator as well as the surface derivative and the non-local embedding potential acting

on the boundary surface.

Compared to Eq. (4.9) the reformulation of the unknown surface derivative of the “external” wavefunction in terms of the embedding potential has some advantages. It is in general not possible solve Eq. (4.9) because this surface derivative $\partial_n \psi(\vec{r}_S)$ is unknown. Even if there would be only one single solution of the Schrödinger equation in V_0 at the energy ϵ which would be consistent with the desired boundary condition on the outer side of region V_0 , one still would not be able to specify $\partial_n \psi(\vec{r}_S)$ on both surfaces. Having fixed the value of $\partial_n \psi(\vec{r}_S)$ on one surface one has to multiply the derivative on the other boundary with an unknown factor which is actually a property of region Ω . The situation in fact is even more complicated since multiple solutions in V_0 may exist. Eq. (4.16) on the other hand does not suffer from these problems as the embedding potential is uniquely defined by the outer region V_0 only.

However, the embedding potential and therefore the embedding Hamiltonian H_{emb} is energy dependent and the direct solution of Eq. (4.16) for the wavefunctions is in general not possible. Instead the most useful quantity to look at is the Green function in Ω . Using the modified embedding Hamiltonian H_{emb} the Green function is given by

$$(H_{\text{emb}}(\epsilon) - \epsilon)G(\vec{r}, \vec{r}'; \epsilon) = -\delta(\vec{r} - \vec{r}'). \quad (4.18)$$

Since $G(\vec{r}, \vec{r}_0)$ fulfills for any fixed \vec{r}_0 and $\vec{r} \neq \vec{r}_0$ the same Schrödinger equation as the wavefunction, its boundary conditions are actually also treated by an expression completely analogous to Eq. (4.15). One can use the spectral representation of $G(\vec{r}, \vec{r}')$ to show that the Green function obtained from Eq. (4.18) is the Green function of the region Ω being embedded within V_0 with the correct boundary condition to be extended into V_0 [Ing81]. Furthermore, in a direct transfer the embedding potential can be used to obtain the surface normal derivative of the Green function

$$\partial_n G(\vec{r}_S, \vec{r}_S') = 2 \int_S G_S^{-1}(\vec{r}_s, \vec{r}_s'') G(\vec{r}_S'', \vec{r}_S') dS''. \quad (4.19)$$

In this equation an additional index S has been introduced for the embedding potential to distinguish it from the Green function G as these two symbols denote completely different quantities. One should be careful, not to confuse the embedding potential G_S^{-1} , being a quantity determined by the outer volumes V_0 , with the Green function G of region Ω .

4.7 Self-consistent Embedding

Knowing the Green function in the embedded region Ω allows now also to determine self-consistently the potential in Ω upon which the Green function is calculated. This is the typical situation in density functional theory and is called self-consistent embedding. In the embedding theory, the Green function, satisfying the outgoing boundary condition, is calculated by adding the matrix elements of the embedding potentials, $G_{S_L}^{-1}$ and $G_{S_R}^{-1}$, to the Hamiltonian of the *isolated* slab region Ω . The imaginary part of such a Green function is related to the (local) density of states of the system by

$$n(\vec{r}; \epsilon) = -\frac{1}{\pi} \Im G(\vec{r}, \vec{r}; \epsilon). \quad (4.20)$$

This equation can easily be derived from the spectral representation of the Green function. Writing symbolically

$$G(z) = \frac{1}{z - H}, \quad (4.21)$$

for the complex energy $z = \epsilon + i\delta$ and using the eigenfunctions $\psi(\vec{r})$ (with corresponding eigenvalue ϵ_ψ) as a complete, orthogonal basis set one obtains the spectral representation of the Green function

$$G(\vec{r}, \vec{r}'; \epsilon + i\delta) = \sum_{\psi} \frac{\psi(\vec{r})^* \psi(\vec{r}')}{\epsilon - \epsilon_\psi + i\delta}. \quad (4.22)$$

Using the Dirac identity

$$\lim_{\delta \rightarrow +0} \frac{1}{x + i\delta} = P \frac{1}{x} - i\pi \delta(x), \quad (4.23)$$

with P denoting the principle value, one can rewrite the imaginary part of the diagonal ($\vec{r} = \vec{r}'$) elements of G

$$\begin{aligned} \Im G(\vec{r}, \vec{r}; \epsilon) &= \sum_{\psi} |\psi(\vec{r})|^2 \Im \lim_{\delta \rightarrow +0} \frac{1}{\epsilon - \epsilon_\psi + i\delta} \\ &= -\pi \sum_{\psi} |\psi(\vec{r})|^2 \delta(\epsilon - \epsilon_\psi) \\ &= -\pi n(\vec{r}, \epsilon). \end{aligned} \quad (4.24)$$

This equation forms the basis of the self-consistent embedding scheme in which the standard procedure described in chapter 2 diagonalising the Hamiltonian and

determining the charge density by the summation over all occupied states is replaced by the inversion of the Hamiltonian to determine the Green function. The total charge density or more accurately the particle density is determined from

$$n(\vec{r}) = -\frac{1}{\pi} \Im \int^{e_F} G(\vec{r}, \vec{r}; z) dz. \quad (4.25)$$

The energy integration is carried out along some contour in the complex plane up to Fermi energy e_F to avoid poles of the Green function on the real axis [ZDD82]. The embedding approach deals with a small system in contact with a large outer volume. Consequently, the Fermi energy is determined completely by the outer volume. A determination of the Fermi energy by the condition of charge neutrality of the system is needed. Indeed, the embedding region might not necessarily be charge neutral. For example metal surfaces with externally applied electric fields will include extra charges screening the field.

However, it may be worth noting that with the embedding formalism alone, one cannot treat systems with a large bias voltage ΔV applied between the two bulk leads on both sides of an interface. To be concrete, consider a case where $e_{FL} = e_{FR} + \Delta V$ with $e_{FL/R}$ being the Fermi energy of left/right bulk electrode and $\Delta V > 0$. Then, in the energy interval $[e_{FL}, e_{FR}]$, only the states incident from the left contribute to the charge and current densities of the system, whereas the density of states as obtained from Eq. (4.25) contains also the contribution of the states incident from the right. Hence, one must treat one-electron wave functions explicitly. One possibility for doing so can be the use of Eq. (5.35) derived in the next chapter.

Chapter 5

Complex Bandstructure, Embedding and Transport

After both the fundamentals of electronic transport and of the embedding method have been introduced in chapters 3 and 4, respectively, in this chapter both ideas will be combined. Two major themes can be identified: At first, a transfer-matrix will be introduced. In this context the concept of the complex bandstructure plays a key role. The complex bandstructure is one of the most powerful tools in the discussion of effects at interfaces or surfaces. An extensive and detailed discussion of the general properties of the complex bandstructure can be found in [Hei64].

Not so much weight will be given to the mathematical foundations behind the idea of extending the well known 'real' bandstructure into the complex \vec{k} space, but instead the attention should be concentrated on the significance of the complex bandstructure to semi-infinite systems and transport calculations. However, before starting it must be stressed that even though the complex bandstructure is generally used in these systems with broken translational symmetry, it is actually a bulk property.

The second part of the current chapter will deal with the calculation of electronic transport within the embedding method. First, it will be shown that the transmission coefficients which are needed for the evaluation of the Landauer equation (5.39) can be obtained from the transfer-matrix and the complex bandstructure. However, later applications are based on the reformulation of the Landauer equation in terms of the Green functions available in the embedding method. The chapter will be closed by a discussion of the reformulation of Bardeen's formalism in terms of Green functions.

5.1 The Transfer-Matrix

We start again with considering a slab Ω . The theoretical description which will follow does not depend on the actual form of the boundaries S_b . They might be planar or curved, the only necessary assumption is that they enclose the space of the slab without any holes, i.e. they must be topological equivalent to planar boundaries. However, since many quantities are defined on the boundaries one should define a coordinate system on the boundaries. For the sake of simplicity the boundary surfaces are assumed to be planar and parallel such that one can define a Cartesian coordinate system (x, y, z) where (x, y) are the two-dimensional coordinates in the boundary surfaces and (z) is the coordinate perpendicular to them. Two-dimensional vectors will be denoted by the index \parallel and the normal component of vectors by the character n or z . The issue of defining the boundary surfaces will be re-discussed in chapter 6 when the LAPW basis set is introduced.

Since the Schrödinger equation is a second order differential equation, the solution $\psi(\vec{r})$ in Ω with (in general complex) energy z is completely determined by specifying the value $\psi(\vec{r}_b)$ and the derivative in the local surface-normal direction $\partial_n \psi_b = \frac{\partial}{\partial n} \psi(\vec{r}_b)$ on one of the boundary surfaces, $b = L$ or $b = R$. Again, the outwards normal direction is chosen to define the positive surface normal. To simplify the notation, one can collect the value $\psi(\vec{r}_b)$ and the derivative $\partial_n \psi(\vec{r}_b)$ of the solution to define the vector of boundary value

$$\Psi_b = \begin{pmatrix} \psi(\vec{r}_b) \\ \partial_n \psi(\vec{r}_b) \end{pmatrix}. \quad (5.1)$$

The transfer-matrix T , called T-matrix hereafter¹, maps the left boundary values of the solution of the Schrödinger equation onto the right ones:

$$\Psi_R = T \Psi_L. \quad (5.2)$$

Obviously, the T-matrix is a property of the region Ω only. Only the Hamiltonian, in particular the potential $V(\vec{r})$, needs to be known in region Ω .

The T-matrix describes the propagation of solutions of the Schrödinger equation through Ω , given in terms of the value and the normal derivative on one boundary. This suggests that the T-matrix may quite naturally be expressed by the Green function. Using again Green's theorem Eq. (4.12), it allows to express the wave-

¹In scattering theory, T-matrix is meant as an abbreviation of the transition matrix, which is different from the transfer-matrix defined in this work.

function $\psi(\vec{r})$ in region Ω including the boundaries S_L and S_R by the corresponding Green function $G(\vec{r}, \vec{r}'; \epsilon)$,

$$\psi(\vec{r}) = -\frac{1}{2} \int_{S_L+S_R} [G(\vec{r}, \vec{r}_b) \partial_n \psi(\vec{r}_b) - \partial_n G(\vec{r}, \vec{r}_b) \psi(\vec{r}_b)] d^2 \vec{r}_b, \quad (5.3)$$

where the energy dependence of the Green function has been omitted for simplicity. Placing \vec{r} in Eq. (5.3) at S_L or S_R one obtains a set of linear equations relating ψ_b and $\partial_n \psi_b$ which can be written in matrix notation as

$$\begin{aligned} 2\psi_R &= -G_{RR} \partial_n \psi_R + \partial_n G_{RR} \psi_R - G_{RL} \partial_n \psi_L + \partial_n G_{RL} \psi_L \\ 2\psi_L &= -G_{LR} \partial_n \psi_R + \partial_n G_{LR} \psi_R - G_{LL} \partial_n \psi_L + \partial_n G_{LL} \psi_L. \end{aligned} \quad (5.4)$$

The surface Green functions G_{LL} , G_{LR} , G_{RL} , and G_{RR} are defined by placing \vec{r} and \vec{r}' onto the boundaries S_b and $S_{b'}$, respectively. For example $G_{LR}(z) = G(\vec{r}_L, \vec{r}_R; z)$, means the first argument of the Green function is placed at S_L and the second at S_R . The projected wavefunctions ψ_b are defined analogously. Note, that there is an implicit two-dimensional integration in all products. Since the T-matrix is a linear operator it can be written as

$$T = \begin{pmatrix} T_1 & T_2 \\ T_3 & T_4 \end{pmatrix}. \quad (5.5)$$

Using the same matrix notation, Eq. (5.2) is given by

$$\begin{pmatrix} \psi_R \\ \partial_n \psi_R \end{pmatrix} = \begin{pmatrix} T_1 & T_2 \\ T_3 & T_4 \end{pmatrix} \begin{pmatrix} \psi_L \\ \partial_n \psi_L \end{pmatrix}. \quad (5.6)$$

Comparing Eq. (5.4) with Eq. (5.6) one obtains the sub-matrices T_1 , T_2 , T_3 , and T_4 given by the following set of equations:

$$T_1 = A^{-1} \left(-\frac{1}{2} G_{LR}^{-1} \partial_n G_{LL} - G_{LR}^{-1} + \frac{1}{2} G_{RR}^{-1} \partial_n G_{RL} \right), \quad (5.7)$$

$$T_2 = A^{-1} \left(\frac{1}{2} G_{LR}^{-1} G_{LL} - \frac{1}{2} G_{RR}^{-1} G_{RL} \right), \quad (5.8)$$

$$T_3 = 2G_{LR}^{-1} + G_{LR}^{-1} \partial_n G_{LL} + G_{LR}^{-1} \partial_n G_{LR} T_1, \quad (5.9)$$

$$T_4 = -G_{LR}^{-1} G_{LL} + G_{LR}^{-1} \partial_n G_{LR} T_2, \quad (5.10)$$

with

$$A = -\frac{1}{2}G_{RR}^{-1}\partial_n G_{RR} - G_{RR}^{-1} + \frac{1}{2}G_{LR}^{-1}\partial_n G_{LR}. \quad (5.11)$$

Hence, one can express the T-matrix in terms of the Green function and its normal surface derivative. A particularly simple form is obtained by choosing a Green function which satisfies the von-Neumann boundary condition of vanishing normal derivative on S :

$$\frac{\partial}{\partial n}G(\vec{r}, \vec{r}_b; z) = 0 \quad \text{for } \vec{r} \neq \vec{r}_b. \quad (5.12)$$

In this case, Eqs. (5.7)-(5.11) simplify to

$$T = \begin{pmatrix} G_{RR}G_{LR}^{-1} & \frac{1}{2}G_{RL} - \frac{1}{2}G_{RR}G_{LR}^{-1}G_{LL} \\ 2G_{LR}^{-1} & -G_{LR}^{-1}G_{LL} \end{pmatrix}. \quad (5.13)$$

Even though the formulation of the T-matrix in terms of a Green function with vanishing normal derivative at the boundaries is simple, it is important to realize that the Green function with the von-Neumann boundary condition is not necessarily suitable to calculate other quantities as it does not correspond to a reasonable physical setup. While it might seem difficult to construct the Green function with the special requirement of von-Neumann boundary condition, this problem can actually be easily solved using the embedding method. According to Eq. (4.16) one constructs the Hamiltonian

$$H_{\text{emb}} = H(\vec{r}) + \frac{1}{2}\delta(n - n_S)\frac{\partial}{\partial n}, \quad (5.14)$$

i.e. the embedding Hamiltonian of the system with zero embedding potential. The Green function corresponding to this Hamiltonian fulfills the desired boundary condition.

Before describing possible applications of the theory, the definition of the transfer-matrix should be compared to those of other existing methods. At first glance the T-matrix method seems similar to electronic structure methods which implemented some propagation formalism like those in Refs. [AH72, HT94]. However, these methods differ in one important aspect: The transfer-matrix is not obtained by solving an initial value problem in which one chooses boundary values only at one surface and integrates the Schrödinger equation on a real space grid to obtain the values on the opposite side. Because of the existence of the exponentially increasing solutions of the Schrödinger equation such an approach suffers from instabilities. Furthermore, so far the application of such methods has been restricted to local pseudo-potentials. In the calculation of the T-matrix by Eq. (5.13) both boundaries are treated equally. A further point to mention is the difference between the definition of the transfer-matrix in Eq. (5.2) and the one used for example by van Hoof *et al.* [vHSKB98].

While van Hoof et al. use an additional basis outside region Ω , i.e. to the left of S_L and to the right of S_R , to define a transfer-matrix which operates on states given in this basis at the boundaries, the discussion presented here treats the region Ω only and does not depend on any outside regions.

5.2 T-Matrix and Complex Bandstructure

In this section the T-matrix will be calculated for a system with translational symmetry normal to the slab. The eigenvalue problem of the T-matrix will be investigated and the complex bandstructure is introduced. Hence, the region Ω is now assumed to be a principal layer of bulk material with three-dimensional translational symmetry. The principal layer is a bulk unit that can generate the infinite three-dimensional bulk material upon application of translational symmetry operations. For example, for a lattice with bcc or fcc crystal symmetry the principal layer is just a monolayer, or a plane of atoms, respectively. Thus, there exists a translation vector \vec{d} between S_L and S_R , which is a lattice vector. In this special case an interesting observation can be made. The Bloch theorem follows from the fact that in an infinite crystal the eigenfunctions of the Hamiltonian can be chosen such that these functions are at the same time eigenfunctions of the translation operator which keeps the lattice invariant. This is the consequence of these translations commuting with the Hamiltonian due to the periodicity of the potential. If the region Ω is now a principal layer of some crystal the T-matrix of the system can be viewed as a special case of such a translation operator. In fact, it translates the vector of the boundary value of the wavefunction (5.1) from S_L to S_R , which is actually (neglecting the definition of surface normals for the moment) the same operation as the translation operator $T_{\vec{d}}$, which translates by \vec{d} , performs on this vector. Therefore, the eigenvalues of the T-matrix of such a principal layer should be the same as the eigenvalues of $T_{\vec{d}}$ which can be written as

$$\lambda = e^{i\vec{k}\vec{d}}. \quad (5.15)$$

This leads to the following so-called generalized Bloch condition that will hold between the vectors of boundary values Ψ_L and Ψ_R [Eq. (5.1)]:

$$\Psi_R = \begin{pmatrix} \psi(\vec{r}_L + \vec{d}) \\ \partial_n \psi(\vec{r}_L + \vec{d}) \end{pmatrix} = e^{i\vec{k}\vec{d}} \tilde{I} \Psi_L. \quad (5.16)$$

The matrix $\tilde{I} = \begin{pmatrix} 1 & 0 \\ 0 & -1 \end{pmatrix}$ was introduced to take the definition of the positive

surface normal into consideration, which reverses its direction as \vec{r}_S changes from S_L to S_R . Together with Eq. (5.2) one obtains the eigenvalue problem for T :

$$T\Psi_L = \lambda \begin{pmatrix} 1 & 0 \\ 0 & -1 \end{pmatrix} \Psi_L \quad (5.17)$$

$$\tilde{T}\Psi_L = \lambda\Psi_L. \quad (5.18)$$

In the last equation the T-matrix $\tilde{T} = \tilde{I}T$ is redefined to include \tilde{I} . To understand the significance of Eqs. (5.16) and (5.17) the physical background of the generalized Bloch condition is discussed: In bulk crystals, the Bloch theorem states that the solutions of the Schrödinger equation can be chosen such that they fulfill Eq. (5.16) with a real Bloch vector \vec{k} . The fact that the Bloch vector is required to be real is not a consequence of diagonalizing simultaneously the Hamiltonian and the translation operator, but it follows from the additional requirement that in an infinite crystal a solution of the Schrödinger equation should be normalizable. Since a Bloch function with a complex vector $\vec{k} = \vec{q} + i\vec{k}$ grows exponentially due to the factor $\exp(i\vec{q}\vec{r}) \exp(-\vec{k}\vec{r})$ in some direction of \vec{r} it can not be normalized when integrated over the entire infinite crystal. However, in cases in which the crystal is actually not truly infinite, these exponentially growing or decaying solutions, also called evanescent states, can occur. The classical example for these solutions are surface states, which decay exponentially from the surface.

The extension of the possible \vec{k} -vectors to the complex plane extends the well-known bandstructure $\epsilon(\vec{q})$. In principle, the two equations

$$H\psi = z\psi \quad (5.19)$$

and

$$T_{\vec{d}}\psi = \lambda\psi \quad (5.20)$$

define a generalized bandstructure $z(\vec{k})$, where both z and \vec{k} can take complex values. In general, one only considers real energies and the term „complex bandstructure“ is conventionally used to actually refer to the so called “real lines” consisting of the solutions with real energy and real or complex \vec{k} . In standard electronic structure calculations one chooses a specific \vec{k} vector, i.e. a specific $\lambda = \exp(i\vec{k}\vec{d})$, and then solves Eq. (5.19) to obtain the eigenvalues of the Hamiltonian consistent with Eq. (5.20). Here, the opposite becomes feasible. To obtain the “real lines” one determines the T-Matrix $T(\epsilon)$ for a set of real energies ϵ and solves Eq. (5.17) for

$\lambda(\epsilon)$. In this work, only systems with two-dimensional translation symmetry are considered. In this case the parallel component \vec{k}_{\parallel} of \vec{k} is a good quantum number, i.e. the Hamiltonian, the Green function and the T-matrix are diagonal in \vec{k}_{\parallel} and, together with the energy ϵ , \vec{k}_{\parallel} is chosen in advance to calculate the perpendicular component $k_z(\vec{k}_{\parallel}, \epsilon)$.

This section will be closed by the discussion of some important properties of the T-matrix. As the solution of the Schrödinger equation is uniquely determined by the vector of the boundary values Ψ_L (or Ψ_R), the eigenvectors of the T-matrix are linearly independent and the T-matrix can be inverted. The inverse T-matrix maps Ψ_R onto Ψ_L . For a real band, i.e. for an energy $z = \epsilon$, time inversion symmetry requires $\epsilon(\vec{k}) = \epsilon(-\vec{k})$ and the eigenvalues of the T-matrix occur in pairs λ, λ' with

$$\lambda\lambda' = 1 \tag{5.21}$$

. In other words, for each eigenvalue ϵ of H and for each λ of the eigenvalue spectrum of T corresponding to the generalized Bloch vector \vec{k} , there exists an inverse eigenvalue λ^{-1} corresponding to $-\vec{k}$ and therefore the inverse T-matrix T^{-1} has the same eigenvalue spectrum as T . This opens up an interesting aspect of the theory. The eigenvectors of T can be grouped into two sets. One set of eigenvectors corresponds to states which propagate to the left if $|\lambda| = 1$ or decay to the left if $|\lambda| > 1$. The other set contains eigenvectors describing states propagating to the right ($|\lambda| = 1$) or decaying to the right $|\lambda| < 1$. One should note that the classification of the propagating states with $|\lambda| = 1$ cannot be achieved by the direction of the \vec{k} -vector but only by the direction of the current flow. This classification of the eigenstates is important for the application of the complex band structure theory discussed next: the calculation of the embedding potential.

5.3 Complex Bandstructure and Embedding Potential

In this work the most important application of the T-matrix and of the complex bandstructures will be the determination of the embedding potential. The embedding potential was defined in the previous chapter (Eq. (4.15)) as the surface inverse of a very special Green function. To use this definition for a calculation of the embedding potential one has to determine the Green function of the bulk with von-Neumann boundary condition on the embedding surface and with outgoing boundary condition towards infinity. This is a difficult task to perform. Most

successful has been the iterative procedure proposed in Ref. [CvHNI92] which was applied in some cases [CNvHI93, Ish97, TBCI96]. However, the iterative method has two major drawbacks: very often many iterations are needed to reach a good level of convergence and more seriously, it turns out to be very hard to obtain embedding potentials for real energies with this method, as the outgoing boundary condition cannot be ensured for real energies. Instead, another method to determine the embedding potential will be used in this work. The starting point is Eq. (4.15), which is repeated here for convenience.

$$\partial_n \psi(\vec{r}_S) = 2 \int_S G_S^{-1}(\vec{r}_s, \vec{r}_s') \psi(\vec{r}_s') dS', \quad (5.22)$$

which is interpreted as the embedding potential acting as a linear operator on $\psi(\vec{r}_S)$ to yield $\partial_n \psi(\vec{r}_S)$. Such an operator is completely known, if its action on any complete set of functions $\psi(\vec{r}_S)$ is known. Now, one should turn back to Eqs. (5.19) and (5.20). In the same manner as the eigenvectors of the Hamiltonian span the complete space of possible solutions consistent with the chosen \vec{k} vector, the eigenvectors of the T-matrix span at the chosen energy the complete space of possible boundary conditions for the solutions of the Hamiltonian. However, out of all these eigenvectors one is only interested in those consistent with the outgoing boundary condition, i.e. only the boundary vectors of states propagating or decaying away from the interface are needed.

Eq. (5.22) can be inverted for G_S^{-1} by switching to a symbolic matrix notation and using the eigenvectors of the T-matrix to construct the two matrices

$$[\psi] = [\psi_1, \psi_2..](\vec{r}_S) \text{ and } [\partial\Psi] = [\partial\psi_1, \partial\psi_2..](\vec{r}_S). \quad (5.23)$$

I.e. the two matrices $[\psi]$ and $[\partial\psi]$ contain the vectors ψ_i and corresponding $\partial\psi_i$ as columns, respectively. The subscript i labels the eigenvectors Ψ_i of the T-matrix corresponding to outgoing solutions. As the vectors ψ_i are linear independent and complete, one can use the matrices defined in Eq. (5.23) to rewrite

$$[\partial\Psi] = 2G_S^{-1} [\Psi] \quad (5.24)$$

which can be solved for the embedding potential

$$G_S^{-1} = \frac{1}{2} [\partial\Psi] [\Psi]^{-1}. \quad (5.25)$$

This allows the calculation of the embedding potential directly from the states of

the complex bandstructure, i.e. from the T-matrix. No iteration is needed and the method works both for real and complex energies.

5.4 Wavefunction-Matching

The T-matrix and the complex bandstructure can be used for a simple solution of the transport problem in the Landauer approach. The starting point for this solution is the decomposition of the asymptotic wavefunction in the leads into incoming, reflected and transmitted states. These regions are assumed to be already part of semi-infinite bulk crystals, i.e. the potential is that of the bulk and therefore the solutions can be described by the states of the complex bandstructure. The decomposition of the asymptotic wavefunction (5.34) on the boundary S_b between the leads and the interface region, which contains all the potential perturbation, can now be written in terms of the vectors of boundary values

$$\Psi_L = \Psi_{in} + \sum_n r_n \Psi_L^n \quad (5.26)$$

and

$$\Psi_R = \sum_{n'} t_{n'} \Psi_R^{n'}. \quad (5.27)$$

In these expansions the boundary vector Ψ_{in} must correspond to an incoming Bloch state, i.e. a Bloch state with net current flowing from the left to the right, the boundary vectors of the reflected waves Ψ_L^n must be outgoing Bloch states or evanescent states decaying to the left. Correspondingly, the states with the boundary values Ψ_R^n must be Bloch states with a net current flowing to the right or evanescent states decaying to the right. Hence, here the decomposition of the eigenvalues and eigenstates of the T-matrix discussed in section 5.2 must be used again.

As these boundary values are related by Eq. (5.2), one can use the T-matrix in the interface region Ω to obtain the transmission and reflection coefficients by solving

$$\sum_n t_n \tilde{I} \Psi_R^n = T \Psi_L^{in} + \sum_n r_n T \Psi_L^n \quad (5.28)$$

for t_n and r_n . If all Bloch states involved in the decomposition in the asymptotic regions have been normalized to carry unit current perpendicular to the interface,

i.e. if for the boundary values of all these states one has

$$j = \Im \int \Psi_b^* \begin{pmatrix} 0 & 1 \\ 0 & 0 \end{pmatrix} \Psi_b dS = \Im \int \psi^*(\vec{r}_b) \partial_n \psi(\vec{r}_b) dS = \pm 1, \quad (5.29)$$

the transmission coefficients $t_{n,in}$ can be directly used in the Landauer formula

$$\Gamma = \frac{e^2}{h} \sum_{n,in} |t_{n,in}|^2, \quad (5.30)$$

where the summation has to be performed over all incoming Bloch states labeled by in and all transmitted Bloch states n .

This approach is called the simple wavefunction matching method, as it basically determines the reflection and transmission coefficients such that a total wavefunction can be constructed with a continuous value and a continuous first derivative across the interface. This is the procedure one commonly applies in one-dimensional text-book problems on quantum mechanics. Think for example of tunneling across a one-dimensional barrier. This matching of the value and the derivative has been formulated using the T-matrix. While this scheme is simple and very intuitive in its interpretation, the actual numerical application turns out to be difficult. In the formulation presented here, one can basically identify two sources of problems which are both closely linked. Firstly, because of the expansion of the boundary values into plane-waves it becomes necessary to include more two-dimensional plane-waves into the expansion, i.e. more Fourier components, than the actual number of Bloch or evanescent states one wants to match. Of course, there are in principle arbitrarily many evanescent states available for matching, but since those with a large imaginary part of the \vec{k} -vector are rapidly decaying and extremely difficult to converge one does not want to include all of them. The second problem of the simple matching formulation presented here arises from the formulation in terms of the T-matrix. The T-matrix maps the boundary values from the left to the right corresponding to the solution of the initial value problem. Hence again, small numerical inaccuracies on one boundary can lead to exponentially magnified errors on the other boundary. Mathematically, this problem manifests itself in the occurrence of very large and very small eigenvalues of the T-matrix. With increasing thickness of the scattering region, the T-matrix becomes closer and closer to singularity and the solution of Eq. (5.28) cannot be stabilized anymore.

Different ideas have been proposed to overcome the problems of the simple wavefunction matching formulation. The most successful of these match the wavefunctions

in some least square sense, i.e. these methods do not simply try to match all fourier components but try to select only a physical subset of reflected and transmitted states and match the fourier components by minimising their mismatch. More on the mathematical properties of the wavefunction-matching approach can be found in [AH72, WB82, SH88, KS99, KS97].

In this work, the simple wavefunction matching is avoided by using a reformulation of the Landauer equation in terms of Green functions. It avoids the numerical problems associated with the use of the vectors of boundary values by using the generalized logarithmic derivative in the form of the embedding potential instead. By the direct use of the surface-projected Green functions the T-matrix is no longer calculated and the numerical problems in inverting ill-conditioned matrices do not accumulate either.

5.5 Landauer Formulation

The starting point will be again the wavefunction in the asymptotic region. In the following the first superscript, L or R , is used to distinguish between states in the left or the right lead, the second superscript, i or o , to distinguish between incoming and outgoing states with respect to region Ω , and the subscript, b or e , to distinguish between Bloch and evanescent waves. The index α ($\alpha = L$ or $\alpha = R$) is now used to label the two sides to avoid confusion with the superscript used for the Bloch states. For example, $\psi_b^{Li}(\vec{r})$ stands for a Bloch state in the left lead propagating toward the interface. The expectation value of the normal component of the current operator on the boundary surface S_α is given by

$$J_\alpha(\phi, \psi) = \frac{1}{2i} \int_{S_\alpha} [\phi^*(\vec{r}_S) \partial_n \psi(\vec{r}_S) - \partial_n \phi^*(\vec{r}_S) \psi(\vec{r}_S)] dS. \quad (5.31)$$

Suppose that ϕ and ψ are solutions of the Schrödinger equation (5.19) $J_\alpha(\phi, \psi)$ remains constant if S_α is moved around inside the bulk crystal. This property leads to the well-known identities

$$J_\alpha(\psi_e^{\alpha o}, \psi_e^{\alpha o}) = 0, \quad (5.32a)$$

$$J_\alpha(\psi_e^{\alpha o}, \psi_b^{\alpha o}) = J_\alpha(\psi_b^{\alpha o}, \psi_e^{\alpha o}) = 0, \quad (5.32b)$$

$$J_\alpha(\psi_b^{\alpha o}, \psi_b^{\alpha o}) = \delta_{bb'}. \quad (5.32c)$$

The first two of these equations simply state that evanescent states cannot carry any current which is a simple consequence of the current conservation. Eq. (5.32c)

provides a condition for normalizing the Bloch states to carry unit current.

By substituting Eq. (4.15) in Eq. (5.31) and making use of the identity $G_{S_\alpha}^{-1}(\vec{r}_S, \vec{r}_S') = G_{S_\alpha}^{-1}(\vec{r}_S', \vec{r}_S)$, one obtains a useful expression,

$$J_\alpha(\psi_\nu^{\alpha o}, \psi_{\nu'}^{\alpha o}) = 2 \int_{S_\alpha} [\psi_\nu^{\alpha o}(\vec{r}_S)]^* \Im G_{S_\alpha}^{-1}(\vec{r}_S, \vec{r}_S') \psi_{\nu'}^{\alpha o}(\vec{r}_S') dS dS'. \quad (5.33)$$

Similarly, one may define a Wronskian-like quantity $W_\alpha(\phi, \psi)$ by replacing $\phi^*(\vec{r})$ in Eq. (5.31) by $\phi(\vec{r})$. In this case, instead of Eq. (5.33), one has $W_\alpha(\psi_\nu^{\alpha o}, \psi_{\nu'}^{\alpha o}) = 0$.

In the notation introduced, the scattering process in which a Bloch state b incident from the interior of the left is scattered at the interface and either reflected back or transmitted into the right volume as described by Eq. (5.34) is expressed as

$$\psi(\vec{r}) = \begin{cases} \psi_b^{Li}(\vec{r}) + \sum_\nu r_{b\nu} \psi_\nu^{Lo}(\vec{r}) & , \vec{r} \text{ in left volume} \\ \sum_{\nu'} t_{b\nu'} \psi_{\nu'}^{Ro}(\vec{r}) & , \vec{r} \text{ in in right volume} \end{cases}, \quad (5.34)$$

where $r_{b\nu}$ and $t_{b\nu'}$ denote reflection and transmission coefficients, respectively, with subscripts ν and ν' running through both Bloch and evanescent states. Now the boundary conditions of the Green function are specified by assuming that $G(\vec{r}, \vec{r}_S)$ in Eq. (5.3) fulfills the outgoing boundary condition on S_L and S_R . In this case the reflected and transmitted waves in Eq. (5.34) do not contribute to the integral in Eq. (5.33) because $W(\psi_\nu^{\alpha o}, \psi_{\nu'}^{\alpha o}) = 0$. As a result, Eq. (5.3) simplifies to

$$\psi(\vec{r}) = -\frac{1}{2} \int_{S_1} [G(\vec{r}, \vec{r}_S) \partial_n \psi_b^{Li}(\vec{r}_S) - \partial_n G(\vec{r}, \vec{r}_S) \psi_b^{Li}(\vec{r}_S)] dS. \quad (5.35)$$

In deriving Eq. (5.35), it was assumed that \vec{r} is located in Ω . Yet, since S_L can be moved to any place in the left lead, Eq. (5.35) holds for an arbitrary \vec{r} in the left lead. Also, S_R can be moved to any place in the right lead. The Green function with the outgoing boundary condition can be expanded as

$$G(\vec{r}, \vec{r}') = \sum_{\nu, \nu'} g_{\nu\nu'} \psi_\nu^{Lo}(\vec{r}) \psi_{\nu'}^{Ro}(\vec{r}'), \quad (5.36)$$

for \vec{r} in the left lead and \vec{r}' in right lead. One might denote the complex conjugate of $\psi_b^{Li}(\vec{r})$ by $\psi_{b^*}^{Lo}(\vec{r})$, which is a Bloch state propagating to the left. With this in mind, substituting Eq. (5.36) in Eq. (5.35) and using the identity $G(\vec{r}, \vec{r}') = G(\vec{r}', \vec{r})$, one has

$$\psi(\vec{r}) = \sum_{\nu'} i g_{b^*\nu'} \psi_{\nu'}^{Ro}(\vec{r}), \quad \vec{r} \text{ in the right lead.} \quad (5.37)$$

Comparing Eq. (5.37) and Eq. (5.34) yields

$$t_{b\nu'} = i \cdot g_{b^*\nu'}. \quad (5.38)$$

Putting this into the Landauer equation, evaluated for Bloch states at the Fermi energy ϵ_F , one gets

$$\Gamma = \frac{1}{2\pi} \sum_{bb'} |t_{bb'}|^2 = \frac{1}{2\pi} \sum_{b^*b'} |g_{b^*b'}|^2. \quad (5.39)$$

With the use of Eq. (5.32), the summation over all Bloch states can be expanded into a summation over all outgoing (Bloch and evanescent) states by introducing the expectation value of the current operator

$$\Gamma = \frac{1}{2\pi} \sum_{\mu\nu} \sum_{\mu'\nu'} g_{\mu\nu}^* J_1(\psi_\mu^{Lo}, \psi_{\mu'}^{Lo}) J_2(\psi_\nu^{Ro}, \psi_{\nu'}^{Ro}) g_{\mu'\nu'}. \quad (5.40)$$

Using Eqs. (5.33) and (5.36), one finally obtains

$$\Gamma = \frac{2}{\pi} \int_{S_L} dS_L dS'_L \int_{S_R} d\vec{r}_R d\vec{r}'_R G(L, R) \cdot \Im G_{S_R}^{-1}(R, R') G^*(R', L') \Im G_{S_L}^{-1}(L', L), \quad (5.41)$$

where argument L in the Green function stands for \vec{r}_L and the same applies for the other three arguments. With the abbreviation $G_{LR} = G(\vec{r}_L, \vec{r}_R)$, Eq. (5.41) is written more concisely as

$$\Gamma = \frac{2}{\pi} \text{Tr} [G_{LR} \Im G_{S_R}^{-1} G_{RL}^* \Im G_{S_L}^{-1}]. \quad (5.42)$$

This equation expresses the conductance in the Landauer approach by the Green function of the interface with arguments on different sides of the interface G_{LR} and G_{RL} and the embedding potentials. One should note that the fact that only the imaginary part of the embedding potentials enter into the expression corresponds to the summation over propagating Bloch states only in the Landauer equation. While in a taint similarity to the T-matrix the Green functions G_{LR} and G_{RL} also connect the two boundary surfaces in the application of Eq. (5.42), no inversion of ill-converged quantities is needed and hence the stability of the obtained conductance is much better than in the case of the simple wavefunction matching.

Two more comments are in order: (i) The formulas Eqs. (5.42) and (5.43) require the evaluation of the Green functions on boundary surfaces, S_L and S_R . It was

previously shown for a one-dimensional model [IT01] that the Green function calculated with the embedding method is more accurate on boundary surfaces than that obtained by solving the Dyson equation cast in matrix form using basis functions, since the embedding method explicitly takes account of the outgoing boundary condition of the Green function. (ii) Even with the embedding method, it would be extremely difficult to numerically compute the derivatives of the Green function on boundary surfaces, since typically, the Green function is expanded with a finite number of plane-wave like basis functions in actual implementations of the embedding approach. In such an expansion, the numerical derivative converges much slower than the function itself and oscillations in the current density might occur which violate current conservation. With Eq. (5.42) one can avoid this problems since no numerical derivative of the Green function has to be calculated. The embedding potential in Eq. (5.42) is a property of the bulk crystal and should be calculated separately prior to the embedding calculation.

In the past, a number of papers have been published in which the Landauer-Büttiker formula Eq. (5.42) was reformulated in terms of the Green function. Among them Baranger and Stone derived a general conductance formula [BS89] that can be applied to multiple leads in a strong magnetic field. For the present system having two leads on both sides of the interface and without a magnetic field, their formula reads

$$\Gamma = -\frac{1}{4\pi} \int_{S_L} d\vec{r}_L \int_{S_R} d\vec{r}_R \Re[\partial_L \partial_R G(L, R) \times G^*(L, R) - \partial_L G(L, R) \partial_R G^*(L, R)], \quad (5.43)$$

where it is understood that the Green function satisfies the outgoing boundary condition. To proceed, one expresses the normal derivatives of the Green function using the embedding potentials as

$$\partial_L G(L, R) = 2 \int_{S_L} dS'_L G_{S'_L}^{-1}(L, L') G(L', R), \quad (5.44a)$$

$$\partial_R G(L, R) = 2 \int_{S_R} dS'_R G_{S'_R}^{-1}(R, R') G(L, R'), \quad (5.44b)$$

$$\begin{aligned} \partial_L \partial_R G(L, R) &= 4 \int_{S_L} dS'_L \int_{S_R} d\vec{r}_R' \\ &\times G_{S'_L}^{-1}(L, L') G_{S'_R}^{-1}(R, R') G(L', R'). \end{aligned} \quad (5.44c)$$

By substituting Eq. (5.44) in Eq. (5.43) and noting that the arguments in the Green functions and the embedding potentials are permutable, one can show easily that Eq.

(5.43) coincides with Eq. (5.42). Baranger and Stone themselves gave a proof that Eq. (5.43) is equivalent to the Landauer-Büttiker formula. Their derivation is similar but different from the one of Eq. (5.42) in two points. First, they considered only propagating Bloch states in asymptotic regions, whereas here also the evanescent waves in bulk regions are taken into account. Secondly, Eq. (5.35) was derived using a Green's theorem, while Baranger and Stone used another equation that holds for a wave function of a scattered state.

Before closing this section, an interesting aspect of the formalism should be pointed out. Even though the left and right lead volumes attached to region Ω as semi-infinite bulk regions were referred to as bulk so far, this is not a necessary condition. In fact the potential in these regions only has to be that of a periodic bulk crystal far away from the embedding surfaces. If the potential differs from the bulk potential near the embedding surface, Eq. (5.42) can still be applied. The only change in the derivation of the equation would be the naming of the states. One would no longer speak of Bloch and evanescent waves of the bulk but instead of states which carry a current (do not carry a current) and are obtained from Bloch states (evanescent states) by integrating those from the bulk towards the embedding plane, respectively. Thus, by shrinking region Ω and with new boundaries, Eq. (5.42) can still be applied on these boundaries by transferring the embedding potentials to the new embedding surfaces using the embedding method itself [Ish97, CvHNI92]. A particularly simplified limit of this procedure is reached when S_L and S_R coincide with each other.

For simplicity, one might consider S_L and S_R to be planar interfaces with the z axis pointing normal to both the planes. S_L and S_R are chosen as $z = z_L$ and $z = z_R$, respectively, where the limit of $z_R - z_L \rightarrow 0$ is taken in the very end. Integrating Eq. (4.11) along the surface normal direction leads to the cusp condition,

$$\left[\lim_{z \rightarrow z'+0} - \lim_{z \rightarrow z'-0} \right] \partial_z G(\vec{x}, z, \vec{x}', z') = 2 \delta(\vec{x} - \vec{x}'), \quad (5.45)$$

where $z_L < z' < z_R$, and $\vec{x} = (x, y)$ are the planar coordinates. In the limit of $z_R - z_L \rightarrow 0$, the first term of the left-hand side of Eq. (5.45) may be replaced by $\partial_{z_R} G(\vec{x}, z_R, \vec{x}', z_L)$, while the second term by $\partial_{z_L} G(\vec{x}, z_L, \vec{x}', z_R)$. Then, expressing the normal derivatives of the Green function in terms of the embedding potentials

yields

$$\begin{aligned}
 & \int_{S_R} d\vec{x}'' G_{S_R}^{-1}(\vec{x}, \vec{x}'') G(\vec{x}'', z_R, \vec{x}', z_L) \\
 & + \int_{S_L} d\vec{x}'' G_{S_L}^{-1}(\vec{x}, \vec{x}'') G(\vec{x}'', z_L, \vec{x}', z_R) \\
 & = \delta(\vec{x} - \vec{x}').
 \end{aligned} \tag{5.46}$$

Furthermore, in the limit of $z_R - z_L \rightarrow 0$, $G(\vec{x}'', z_R, \vec{x}', z_L)$ in the first term of the left-hand side of Eq. (5.46) becomes identical with $G(\vec{x}'', z_L, \vec{x}', z_R)$. Thus, Eq. (5.46) reads in matrix form as

$$[G_{S_L}^{-1} + G_{S_R}^{-1}] G_{LR} = 1. \tag{5.47}$$

By combining Eqs. (5.42) and (5.47), one obtains

$$\Gamma = \frac{2}{\pi} \text{Tr} \left\{ [G_{S_L}^{-1} + G_{S_R}^{-1}]^{-1} \Im G_{S_R}^{-1} [G_{S_L}^{-1} + G_{S_R}^{-1}]^{*-1} \Im G_{S_L}^{-1} \right\}. \tag{5.48}$$

As expected, the conductance for ballistic transport in this limit can be expressed only in terms of the embedding potentials of the two bulk crystals on both sides of the boundary surface. As the simplest example, let us consider a one-dimensional step potential where $v(z) = 0$ for $z < 0$ and $v(z) = v_0$ for $z > 0$. First, one chooses the boundary surface for the embedding potentials as $z = 0$. Then, for an electron with energy ϵ ($> v_0 > 0$), $G_{S_L}^{-1} = ik_L/2$ and $G_{S_R}^{-1} = ik_R/2$, where $k_L = \sqrt{2\epsilon}$ and $k_R = \sqrt{2(\epsilon - v_0)}$, Eq. (5.48) reproduces a result of elementary quantum mechanics for the transmission probability T ,

$$T = 2\pi\Gamma = \frac{4k_L k_R}{(k_L + k_R)^2}. \tag{5.49}$$

As discussed above, the boundary surface between the two half-spaces do not need to be located at the boundary of the two bulk regions. If it is shifted to $z = -d$ as measured from the potential step, $G_{S_L}^{-1}$ remains the same, whereas the embedding potential for the right half-space now becomes

$$G_{S_R}^{-1} = \frac{ik_L k_R \cos(k_L d) - ik_L \sin(k_L d)}{2 k_L \cos(k_L d) - ik_R \sin(k_L d)}. \tag{5.50}$$

It should be emphasized that in this case the space to the right of $S_L (= S_R)$, i.e. $z > -d$ can not be regarded as a bulk region anymore because of the potential step at $z = 0$. In spite of this, by inserting Eq. (5.50) in Eq. (5.48), one obtains for

Γ exactly the same expression (5.49).

5.6 Green Function formulation of Bardeen's Approach to Tunneling

The rigorous derivation of the Bardeen approach from a Green function formalism is not straight forward. Different approaches to this problem can be found in [Feu74b, Feu74a] and in [AB69]. Here, a somewhat more handwaving approach is presented by showing how to reformulate the Bardeen expression for tunneling derived in section (3.4) in terms of Green functions and how to use the embedding method in this context. The final result however, will be identically to that of the more rigorous treatments. The starting point will be the expression of the tunneling conductance in the Bardeen approximation for zero bias voltage

$$\Gamma = \frac{\pi}{2} \sum_{\mu\nu} \delta(e_F - \epsilon_\mu) \delta(e_f - \epsilon_\nu) \left[\int_S (\psi_L^\mu(\vec{r}) \partial_n \psi_R^\nu(\vec{r})^* - \psi_R^\nu(\vec{r})^* \partial_n \psi_L^\mu(\vec{r})) dS \right]^2, \quad (5.51)$$

which can be rewritten after introducing the operator $J_B = \overrightarrow{\partial}_n - \overleftarrow{\partial}_n$, with the arrow indicating the direction the operator should be applied,

$$\Gamma = \frac{\pi}{2} \sum_{\mu\nu} \delta(e_F - \epsilon_\mu) \delta(e_f - \epsilon_\nu) \int_S \int_{S'} \psi_L^{\mu*}(\vec{r}) J_B \psi_R^\nu(\vec{r}) \psi_L^\mu(\vec{r}') J'_B \psi_R^{\nu*}(\vec{r}') dS dS'. \quad (5.52)$$

In this transformation the square has been rewritten into the double integral which is possible since all the quantities involved are real. The sum and the integral in this equation can be interchanged. Furthermore, the first operator J_B does not operate on the $\psi_L^\mu(\vec{r}')$ and the second operator J'_B does not act on the $\psi_R^\nu(\vec{r})$, and these terms therefore can be interchanged. Thus Eq. (5.52) can be rewritten to

$$\Gamma = \frac{\pi}{2} \int_S \int_{S'} \sum_{\mu\nu} \delta(e_F - \epsilon_\mu) \psi_L^{\mu*}(\vec{r}) \psi_L^\mu(\vec{r}') J_B \delta(e_F - \epsilon_\nu) \psi_R^{\nu*}(\vec{r}') \psi_R^\nu(\vec{r}) J'_B dS dS'. \quad (5.53)$$

In these equations one can identify

$$\sum_{\mu} \delta(e_F - \epsilon_\mu) \psi_L^{\mu*}(\vec{r}) \psi_L^\mu(\vec{r}') = -\frac{1}{\pi} \Im G_L(\vec{r}, \vec{r}'; e_F), \quad (5.54)$$

which is similar to the equation used in the derivation of the local density of states from the Green function in section (4.7) without the requirement that only the

diagonal elements are considered, i.e. the two spacial arguments in the wavefunctions and in the Green function are not the same. Finally one obtains an expression for the conductance in Bardeen's approximation in terms of the two Green functions G_L and G_R

$$\Gamma = \frac{1}{2\pi} \int_S \int_S \Im G_L(\vec{r}, \vec{r}'; e_F) J_B \Im G_R(\vec{r}', \vec{r}; e_F) J'_B dS dS', \quad (5.55)$$

or in the matrix notation, suppressing the energy argument of the Green function,

$$\Gamma = \frac{1}{2\pi} \text{Tr} \Im G_{LL} J_B \Im G_{RR} J_B. \quad (5.56)$$

Before continuing, the significance of the Green functions appearing in this equation should be clarified. Going back to the derivation of Bardeen's model, one remembers that the wavefunctions ψ_L and ψ_R have been defined to be the solutions of the Schrödinger equations of the two separate systems containing only the left/right lead and a semi-infinite barrier. The same now applies to the two Green functions $G_{L/R}$. Replacing the operator J_B by its definition, Eq. (5.56) can now be transformed into

$$\Gamma = \frac{1}{2\pi} \text{Tr} \left[\Im G_{LL} \overrightarrow{\partial}_n \overrightarrow{\partial}_{n'} \Im G_{RR} + \Im G_{LL} \overleftarrow{\partial}_n \overleftarrow{\partial}_{n'} \Im G_{RR} - \Im G_{LL} \overleftarrow{\partial}_n \overrightarrow{\partial}_{n'} \Im G_{RR} - \Im G_{LL} \overrightarrow{\partial}_{n'} \overleftarrow{\partial}_n \Im G_{RR} \right], \quad (5.57)$$

where the prime denotes a normal derivative acting on the second argument of the Green function. When using the embedding method to evaluate Eq. (5.57) one can take advantage of the fact that the normal derivative can be expressed through the embedding potential by Eq. (4.19), and thus one obtains

$$\Gamma = \frac{2}{\pi} \text{Tr} \left[\Im G_{LL} \Im (G_{S_R}^{-1} G_{RR} G_{S_R}^{-1}) + \Im (G_{S_L}^{-1} G_{LL} G_{S_L}^{-1}) \Im G_{RR} - \Im (G_{S_L}^{-1} G_{LL}) \Im (G_{RR} G_{S_R}^{-1}) - \Im (G_{LL} G_{S_L}^{-1}) \Im (G_{S_R}^{-1} G_{RR}) \right], \quad (5.58)$$

with $G_{S_{L/R}}^{-1}$ denoting the matrix of the embedding potential of the barrier region of the left/right system.

Chapter 6

The FLAPW-Method

In the previous chapters only the fundamental framework of the theory was described. All details concerning the actual implementation have been omitted and are described in this chapter. I will now show in detail how the theoretical concepts developed so far are realized in the context of the **F**ull-potential **L**inearized **A**ugmented-**P**lane-**W**aves (FLAPW) method in order to perform realistic calculations. In this chapter three main issues are discussed: (i) The first five sections deal with the introduction of the basis set, the modifications of the computational setup needed for the embedding calculations and the setup of the matrix elements of the Hamiltonian and the overlap matrix. (ii) In the following three sections (6.6-6.8), the embedding and T-matrix formalism presented in a rather general notation in the previous chapters is reformulated in terms of the FLAPW-method. (iii) The last two sections deal with the computational procedure needed for a self-consistent embedding scheme.

One approach to solve a differential equation like the Kohn-Sham equation relies on the introduction of a basis set into function-space and thus of the transformation of the differential-equation into a matrix eigenvalue problem. The wavefunction expanded into these basis functions $\phi_{i,\vec{k}}$ is written as

$$\Psi_{\vec{k},\nu} = \sum_i^N c_{\vec{k},\nu}^i \phi_{i,\vec{k}}, \quad (6.1)$$

where \vec{k} and ν denote the quantum numbers labeling the wavefunction, i.e. the Bloch wave-vector \vec{k} and the band index ν in the case of a crystal, and the index i labels the expansion of the wavefunction in basis functions $\phi_{i,\vec{k}}$. N denotes the total number of basis functions included and defines the dimension of the eigenvalueproblem

introduced below. Many methods use plane-waves as basis functions

$$\phi_{\vec{g},\vec{k}}(\vec{r}) = \frac{1}{\sqrt{V}} e^{i(\vec{k}+\vec{g})\vec{r}}, \quad (6.2)$$

where the prefactor ensures the normalization over a unit cell of volume V . In those methods the index i labeling the basis functions corresponds to the wave-vector \vec{g} of the plane-wave, which is chosen from the reciprocal lattice to ensure translational symmetry. The \vec{k} -dependence of the Bloch-wave is incorporated in the definition of the space spanned by the plane-wave basis. Plane-waves are orthogonal and normalized. Hence, the Kohn-Sham equations can be written as a matrix eigenvalue problem of dimension $N \times N$ for the eigenvalue $\epsilon_{\vec{k},\nu}$ and the eigenvector $c_{\vec{k},\nu}^{\vec{g}}$

$$\left(H_{\vec{k}}^{\vec{g}\vec{g}'} - \epsilon_{\vec{k},\nu} \right) c_{\vec{k},\nu}^{\vec{g}'} = 0, \quad (6.3)$$

where $H_{\vec{k}}^{\vec{g}\vec{g}'} = \langle \phi_{\vec{g},\vec{k}} | H_{\vec{k}} | \phi_{\vec{g}',\vec{k}} \rangle$ denote the matrix elements of the Hamiltonian of the Kohn-Sham equation. An implicit summation over the inner index \vec{g}' is assumed. Usually, Eq. (6.3) is solved only for a few of the lowest eigenvalues corresponding to the occupied states.

This transformation of the differential equation into a matrix eigenvalue problem shows very clearly how the numerical approximations come in. Any complete basis set in function-space would be infinitely large, giving rise to an infinitely large matrix ($N \rightarrow \infty$). Such a matrix cannot be diagonalized in general and therefore one has to introduce a cutoff and restrict the number of basis functions. It is very obvious that both the number of basis functions N used and the actual functional form of the basis functions is of importance when it comes to the accuracy of the solution. If one could choose the eigenfunctions of the matrix as basis functions, for example, one would obtain correct results for the eigenvalues and eigenvectors described by these functions.

These general considerations make it rather obvious that pure plane-waves are a bad choice for the basis functions. The wavefunctions oscillate strongly near the positions of the atoms and therefore a huge number of plane-waves would be necessary to describe this behavior. This large basis set would lead to a huge matrix problem which could not be handled. Therefore, two approaches are frequently used. Either the potential is modified near the nuclei to avoid this oscillatory behavior of the wavefunctions which makes them accessible to an approximation by plane-waves. This idea, which leads to the pseudo-potential methods, will not be applied in this work.

The second successful idea is to modify the basis functions. Instead of simple plane-waves a set of functions is constructed which is better adapted to describe the wavefunctions. This idea leads to the group of **A**ugmented **P**lane-**W**aves (APW) based methods of which one realization is used in this work.

6.1 The FLAPW Basis Set

It follows a short description of the full-potential linearized augmented-plane-waves method as implemented in the FLEUR-code used for the calculations presented in this work. More general information on the FLAPW-method can be found in the book by Singh [Sin94] and in [Kur97, Pen96].

As a first step the space is partitioned into different regions. To treat bulk systems the unit-cell is divided into two regions: spheres around the atom positions, the so-called muffin-tin spheres and the region between these muffin-tin spheres, the so-called interstitial region (Fig. 6.1). In the interstitial region the potential is much flatter than near the nuclei. Therefore, plane-waves should form a rather good basis set in this region.

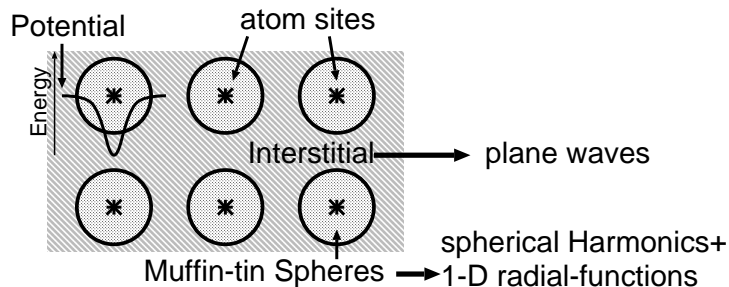


Figure 6.1: The APW setup of a unit-cell. The muffin-tin spheres around the atoms and the interstitial region are shown

In the muffin-tin spheres on the other hand the potential is dominated by the large Coulomb potential of the nucleus

$$V_{nucl} = -\frac{Ze^2}{r}, \quad (6.4)$$

where r denotes the distance from the nucleus and Z is the atomic number. Thus, the differential equation in this region looks very much like an spherically symmetric atomic potential and one expects that the wavefunctions is also similar to atomic wavefunctions. Hence, the goal of using functions in the basis which describe the

physical eigenfunctions with great accuracy can be reached by using a product of spherical harmonics $Y_{lm}(\hat{r})$, where \hat{r} is the direction unit-vector, and radial wavefunctions $u_l(r)$ which solve the spherically symmetric problem. Augmenting the plane-wave basis in the interstitial region with the localized functions $u_l(r)Y_{lm}(\hat{r})$ in the muffin-tin spheres as at the heart of the augmented plane-wave (APW) method. As known from any quantum-mechanics textbook (see for example [LLP79]), the radial part $u_l(r)$ of the Schrödinger equation of a particle in a spherically symmetric potential is the solution of the following one-dimensional differential equation

$$\left\{ -\frac{1}{2} \frac{\partial^2}{\partial r^2} + \frac{1}{2} \frac{l(l+1)}{r^2} + V_{l=0}(r) - \epsilon_l \right\} r u_l(r) = 0. \quad (6.5)$$

From this differential equation the functions $u_l(\epsilon_l, r)$ are determined using an energy-parameter ϵ_l and the spherically averaged potential $V_{l=0}(r)$. The functions $u_l(\epsilon_l, r)$ will only approximate the radial part of the correct unknown wavefunction reasonably well, if the energies ϵ_l correspond to the band energies $\epsilon_{\vec{k}, \nu}$ of the problem. Since these energies are not known in advance, this imposes a significant additional problem. This is one of the central problems of the augmented plane-waves method, which makes use of the approach presented so far to construct the basis functions. Since the band-energies are not known, these energies have to be determined iteratively in each step of the self-consistence cycle used to find the solution of the Kohn-Sham equation. However, compared to the pure plane-wave basis the APW basis set has the huge advantage to be optimized to describe the valence state solutions of the Schrödinger equation. Besides the high possible accuracy in the expansion of the solution in the muffin-tin spheres the construction of the basis set separates the valence from the core states. The different radial solutions of the radial Schrödinger equation (6.5) for very different energies (i.e. for different shells) are orthogonal, the space spanned by the APW basis set can be chosen orthogonal to the low energy solutions (core states) and the application of the APW basis can be restricted to the valence band. The core states are very localized and can be treated separately in a pure atomic-like problem.

In the Linearized Augmented Plane-Waves method (LAPW), which was suggested by Andersen [And75], the problem of determining the energies used in the construction of the APW basis is overcome by introducing a linearization of this energy dependence of the $u_l(\epsilon)$ around the energy parameters ϵ_l

$$u_l(\epsilon) = u_l(\epsilon_l) + \dot{u}_l(\epsilon_l)(\epsilon - \epsilon_l), \quad \dot{u}_l = \frac{\partial u_l}{\partial \epsilon}. \quad (6.6)$$

The additional energy derivative of the radial function u_l used in this expansion can be easily obtained by deriving Eq. (6.5) with respect to ϵ_l

$$\left\{ -\frac{1}{2} \frac{\partial^2}{\partial r^2} + \frac{1}{2} \frac{l(l+1)}{r^2} + V_{l=0}(r) - \epsilon_l \right\} r \dot{u}_l(r) = r u_l(r). \quad (6.7)$$

In the actual implementation as used in the **FLEUR** code not a Schrödinger type equation as written in Eqs. (6.5) and (6.7) is used but the so called scalar-relativistic approximation is implemented [KH77]. In this way all relativistic effects except the spin-orbit interaction are included. The radial basis functions u_l and \dot{u}_l become composed of a small and a large component, of which the small component in general can be neglected at some distance from the nuclei. In standard applications of the **FLEUR** code spin-orbit coupling can also be included in a second variation procedure, however, this approach is not yet implemented in the Green function part of the code. More details on the scalar-relativistic approximation can be found in [Kur01].

Concluding, the basis function in the interstitial region and in the muffin-tin spheres have the following form

$$\phi_{\vec{g}, \vec{k}}(\vec{r}) = \frac{1}{\sqrt{V}} \begin{cases} e^{i(\vec{k}+\vec{g})\vec{r}} & , \text{ interstitial region} \\ \sum_{lm} \left[A_{lm}^{\alpha\vec{g}}(\vec{k}) u_l^\alpha(r_\alpha) + B_{lm}^{\alpha\vec{g}}(\vec{k}) \dot{u}_l^\alpha(r_\alpha) \right] Y_{lm}(\hat{r}_\alpha) & , \alpha^{th} \text{ muffin - tin} \end{cases} \quad (6.8)$$

where the basis functions are labeled by the vectors \vec{g} from reciprocal space. The normalisation factor includes the volume V of the unit-cell and the index α of the coordinates r and \hat{r} should indicate that these coordinates are relative to the center of the α^{th} muffin-tin sphere. The coefficients $A_{lm}^{\alpha\vec{g}}$ and $B_{lm}^{\alpha\vec{g}}$ are determined by the condition that each basis function and its first radial derivative are continuous across the muffin-tin boundary.

The basis functions as defined by Eq. (6.8) are not orthogonal. Therefore the overlap matrix

$$S_{\vec{k}}^{\vec{g}\vec{g}'} = \int \phi_{\vec{g}, \vec{k}}(\vec{r})^* \phi_{\vec{g}', \vec{k}}(\vec{r}) d\vec{r} \quad (6.9)$$

is not diagonal and has to be included in many matrix equations. In particular, the eigenvalue equation Eq. (6.3) is modified to

$$\left(H_{\vec{k}}^{\vec{g}\vec{g}'} - \epsilon_{\vec{k}, \nu} S_{\vec{k}}^{\vec{g}\vec{g}'} \right) c_{\vec{k}, \nu}^{\vec{g}'} = 0. \quad (6.10)$$

6.2 The Boundary Conditions

Using the LAPW basis functions to expand the Hamiltonian, the Green function or other operators one has to take care of the boundary conditions. While at the first glance the two formulations

$$(\epsilon - H(\vec{r})) G(\vec{r}, \vec{r}') = \delta(\vec{r}, \vec{r}') \quad (6.11)$$

and

$$\left(\epsilon S_{\vec{k}}^{\vec{g}\vec{g}'} - H_{\vec{k}}^{\vec{g}\vec{g}'} \right) G_{\vec{k}}^{\vec{g}'\vec{g}''} = \delta_{\vec{g}\vec{g}''}, \quad (6.12)$$

(with I denoting the unit matrix) might seem identically, they actually differ in one very important aspect. Since the basis functions $\phi_{\vec{g},\vec{k}}(\vec{r})$ are Bloch functions, i.e. except for the factor $\exp(i\vec{k}\vec{r})$ they are periodic within the reciprocal lattice, the matrices $H_{\vec{k}}^{\vec{g}\vec{g}'}$ and $G_{\vec{k}}^{\vec{g}'\vec{g}''}$ can only include the periodic contribution of the operators. In other words, in Eq. (6.12) the boundary conditions are already included in the basis set, while they can be specified separately in Eq. (6.11). In a more mathematical language, the introduced basis set might only span a subspace of the Hilbert space in which one seeks a solution of Eq. (6.11).

Hence, additional care has to be taken when the FLAPW basis set is applied to the systems dealt with in this work. These systems are periodic only in two dimensions. In the third direction the periodicity is broken. Hence, while the periodicity of the plane-waves in the basis set is appropriate for the in-plane component of the basis if the corresponding \vec{g}_{\parallel} vectors are from the two-dimensional reciprocal lattice, the third component perpendicular to the surfaces has to be treated differently. Two conditions have to be fulfilled for this perpendicular component of the basis function. Firstly, it must not impose any unwanted periodicity or symmetry into the system. Secondly, it should be flexible to treat any boundary condition as these boundary conditions are no longer assumed fixed but included in the variational principle by the embedding scheme.

Starting from the bulk FLAPW-functions one writes for the interstitial

$$\phi_{n_{\parallel}, n_{\perp}, \vec{k}_{\parallel}}(\vec{r}) = \frac{1}{\sqrt{V}} e^{i(\vec{k}_{\parallel} + \vec{g}_{\parallel}^n)\vec{r}_{\parallel}} \zeta_{n_{\perp}}(z). \quad (6.13)$$

This product ansatz already take the remaining two-dimensional periodicity into account. Many different choices for the z -dependent part $\zeta_{n_{\perp}}(z)$ of the basis can be thought of [Ish97, KS97, SH88]. In this work these functions also have been chosen to be exponential functions as this makes it possible to treat all coordinates on the

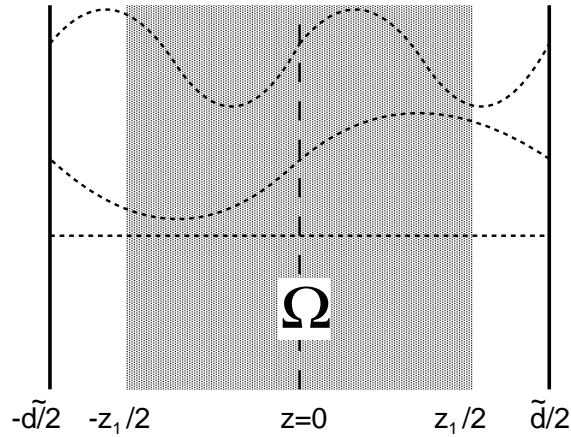


Figure 6.2: Construction of the basis functions perpendicular to the interfaces. The periodicity of the plane-waves \tilde{d} is chosen to be larger than the distance between the two boundary planes z_1 to ensure sufficient variational freedom to treat the boundary conditions on these planes. The real part of three plane-waves $\exp\left(in_{\perp}\frac{2\pi}{\tilde{d}}z\right)$ ($n = 0, 1, 2$) is shown.

same footing at many instances. However, to fulfill the criteria discussed above, the g_z values of these exponential functions have been chosen not to impose periodicity within the region Ω . As illustrated in Fig. 6.2 this was achieved by choosing

$$g_{z,j} = \frac{2\pi}{\tilde{d}} n_{\perp}, \quad (6.14)$$

where n_{\perp} is some integer (positive, zero or negative) and \tilde{d} is larger than the distance between the two boundary surfaces at $\pm z_1/2$. Furthermore, the coordinate system has been defined such that the $z = 0$ plane is centered between the two boundaries. By means of this construction, the values at the boundary

$$\dots, e^{-i\frac{2\pi}{\tilde{d}}z_1}, e^{-i\frac{\pi}{\tilde{d}}z_1}, 1, e^{i\frac{\pi}{\tilde{d}}z_1}, e^{i\frac{2\pi}{\tilde{d}}z_1}, \dots \quad (6.15)$$

do not impose any restriction on the boundary values which can be described. The same procedure is successfully applied in the film version of the FLEUR code to treat the boundary between the interstitial and the vacuum region (see for example [Kur01]). The total basis function can still be written in the form given by Eq. (6.8), however, with the z -component of the \vec{g} vector no longer taken from a bulk reciprocal lattice, but of the form given by Eq. (6.14). In order to simplify the notation, the indices n_{\parallel} and n_{\perp} labeling the parallel and perpendicular part of the plane wave \vec{g} -vectors, respectively, will often be combined to a single index n labeling the basis function. The normalisation volume used in the construction of

the basis is modified to be

$$V = \tilde{d}A, \tag{6.16}$$

where A is the area of the two-dimensional unit cell of the system, i.e. it is slightly larger than volume Ω .

To improve the basis set, it can be supplemented by local orbitals [Sin91] or alternatively an APW+LO basis set could have been chosen as suggested by Sjöstedt et al. [SNS00]. The higher efficiency of these basis functions can be used in cases in which high lying core states exist or in which different bands with the same l -character in different energy ranges must be described beyond the possibility provided by the linearisation in the LAPW. In some cases the use of APW+LO can also lead to accurate results with a smaller basis set. These extensions are implemented in the FLEUR code and can be used in the Green function code. Since these modifications do only affect the representation of the basis in the muffin-tin spheres these additional basis functions do not modify most of the discussion to follow.

6.3 Two regions

Although the formulation of the embedding Green function, the T-matrix and all transport properties has been given for arbitrary embedding and scattering surfaces, for any practical application planar surfaces are easiest to work with. In this respect the choice of the FLAPW basis set creates a significant difficulty not discussed so far. Using the well established choices for the size of the muffin-tin spheres, it is in general not possible to define a planar surface between adjacent monolayers which does not cut through muffin-tin spheres. Cutting through muffin-tin spheres introduces limitations in the numerical accuracy of the final results and should preferably be avoided. Also the reduction of the radius of the muffin-tin sphere is no suitable option as one frequently loses the efficiency of the basis set and thus has to use a much larger set of functions without being able to keep the desired precision. Using a curved surface, on the other hand would make the formulation of the scheme extremely cumbersome as many quantities like the embedding potential, the T-matrix and its eigenstates are defined on the surface only and one wants to expand them in a basis as simple as possible. Furthermore, the use of a curved surface would make the formulation of the projections of the three-dimensional quantities on the boundaries complicated. One option to overcome the difficulty is a technique developed by Krasovskii [KSS99] in which the LAPW basis is expressed in a plane-wave basis except in regions described by very small spheres. An other one is a

setup introduced by Ishida [Ish01], which is used in this work.

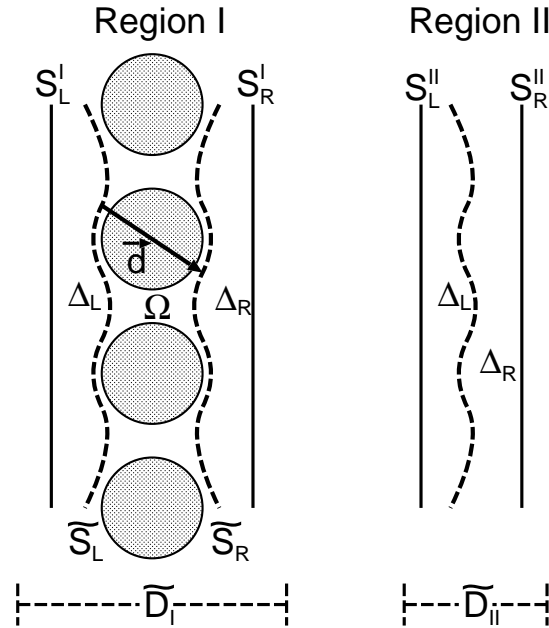


Figure 6.3: Setup used to generate planar boundary surfaces. Two additional volumes are added (Δ_R and Δ_L) to region Ω to obtain region I. The second region consists only of these additional volumes.

As illustrated in Fig. 6.3 two auxiliary volumes Δ_R and Δ_L are added to the right and left of the curved boundary surfaces \tilde{S}_R and \tilde{S}_L of the slab Ω , respectively, until planar surfaces S_b^I can be constructed. The slab Ω and the attached auxiliary volumes Δ_R and Δ_L constitute the region I. Additionally, a second region between the planar surfaces S_b^{II} is introduced containing no muffin-tin spheres but only the volumes Δ_L and Δ_R (region II). These two auxiliary volumes can be joined together without voids as the curved surface \tilde{S}_R and \tilde{S}_L are simply shifted by the lattice vector \vec{d} .

Region I is the primary target of the calculation containing the physical problem of region Ω . Here, the FLAPW basis set is used to expand the Hamiltonian and the Green functions. The treatment of region II on the other hand can be different. Depending on the choice of the potential in the auxiliary volumes and in region II two different modes to treat region II have been implemented.

The use of the auxiliary volumes enables the embedding plane to cut only through the interstitial region. Thus the representation of the two-dimensional quantities like the embedding potential or the T-matrix can be expanded in a two-dimensional basis set which is defined by the restriction of the LAPW basis functions to the embedding

plane. Since this plane is contained in the interstitial, these two-dimensional basis functions are simple two-dimensional plane-waves

$$\phi_{\vec{g}_{\parallel}, \vec{k}_{\parallel}}(\vec{r}_{\parallel}) = \frac{1}{\sqrt{A}} e^{i(\vec{k}_{\parallel} + \vec{g}_{\parallel})\vec{r}_{\parallel}}. \quad (6.17)$$

How these two regions can be used to actually construct the T-matrix of region Ω will be demonstrated in Sec. 6.7.

6.4 Auxiliary volumes

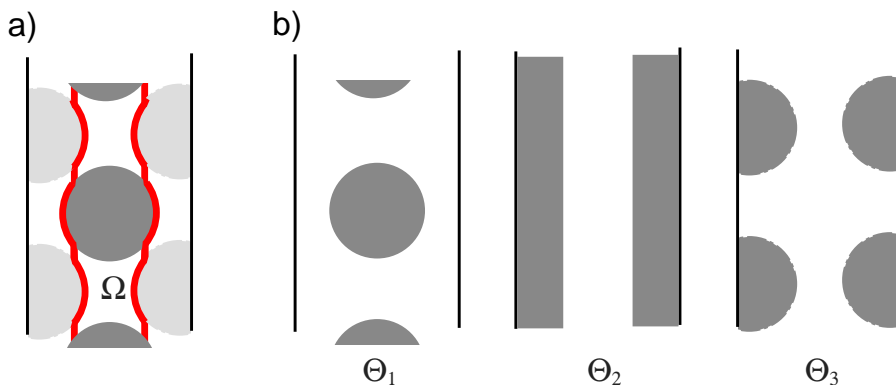


Figure 6.4: a) Definition of a curved boundary surface (thick line) by the intersection of a plane with the muffin-tin spheres. The dark circles denote muffin-tin spheres at atoms in Ω , the lighter muffin-tin spheres of the next bulk monolayer outside Ω which are cut by a plane. b) Corresponding definition of the three step function θ_{1-3} which are assumed to be zero in the shaded regions.

The most efficient treatment of the auxiliary volumes and of region II is possible if the potential in these volumes is set to some constant. This is possible if the curved boundary surface is thought to be composed of a plane in the interstitial region joined to the caps of the muffin-tins intersected by the plane. Fig 6.4 shows this setup. The potential is now chosen to be constant (zero for simplicity) in the auxiliary regions between the embedding plane and the curved boundary surface. In practice this is achieved by setting up three different step functions. The first, well known from usual FLAPW calculations is zero in the muffin-tin spheres around the atoms

$$\theta_1(\vec{r}) = \begin{cases} 1 & \text{in interstitial of region I} \\ 0 & \text{in muffin-tin spheres.} \end{cases} \quad (6.18)$$

In this step function only the remaining muffin-tin spheres in Ω are taken into account. The second step function θ_2 simply cuts off all space beyond the plane as defined in Fig. 6.4. The third function θ_3 is defined similar to the first, however, this time the muffin-tin spheres of the next monolayers cutted by the plane are the areas of space where θ_3 is set to zero. With the help of the three step functions the matrix elements of the interstitial potential are calculated in the following form

$$V_{\text{int}}^{\vec{g}\vec{g}'} = \frac{1}{V} \int_V e^{-i\vec{g}\vec{r}} V_{\text{int}}(\vec{r}) \theta_1(\vec{r}) \theta_2(\vec{r}) \theta_3(\vec{r}) e^{i\vec{g}'\vec{r}} d^3r. \quad (6.19)$$

In the code the potential V_{int} is actually first given in reziprocal space so that Eq. (6.19) is evaluated in three steps. First the potential is transformed to real space using a fast Fourier transform. Then it is multiplied with the step functions and in the last step a back fast Fourier transform is performed.

Due to the constant potential in region II it can be treated completely analytically. For free electrons one can obtain the well known equation for the Green function

$$G(\vec{r}, \vec{r}'; \epsilon) = \frac{1}{2\pi} \frac{e^{ik|\vec{r}-\vec{r}'|}}{|\vec{r}-\vec{r}'|}, \quad (6.20)$$

where $k = \sqrt{2\epsilon}$. For the calculation of the T -matrix T_{II} , the Green function with von-Neumann boundary condition on the embedding planes is needed. This Green function can most easily be written after performing a Fourier transform parallel to the embedding plane

$$G(\vec{g}_{\parallel}, z; \vec{g}'_{\parallel}, z'; \epsilon) = \delta(\vec{g}_{\parallel}, \vec{g}'_{\parallel}) \frac{2}{k} \frac{\cos(kz^-) \cos(k(d_{II} - z^+))}{\sin(kz_1)}, \quad (6.21)$$

where now $k = \sqrt{2\epsilon - |\vec{k}_{\parallel} + \vec{g}_{\parallel}|^2}$, $z^- = \min(z, z')$, $z^+ = \max(z, z')$ and d_{II} being the distance between the two embedding planes. The projections of this Green function onto the embedding planes can now be easily written as

$$G_{LL}(\vec{g}_{\parallel}, \vec{g}'_{\parallel}) = G_{RR}(\vec{g}_{\parallel}, \vec{g}'_{\parallel}) = \delta(\vec{g}_{\parallel}, \vec{g}'_{\parallel}) \frac{2}{k} \cot(k d_{II}) \quad (6.22)$$

and

$$G_{RL}(\vec{g}_{\parallel}, \vec{g}'_{\parallel}) = G_{LR}(\vec{g}_{\parallel}, \vec{g}'_{\parallel}) = \delta(\vec{g}_{\parallel}, \vec{g}'_{\parallel}) \frac{2}{k} \frac{1}{\sin(k d_{II})}. \quad (6.23)$$

While the substitution of the potential in the auxiliary region by a constant makes it possible to treat region II analytically, it at the same time introduces a discontinuity of the potential into the system. This would not affect the continuity of the Green

function or its derivative, but higher derivatives of the Green function would have a discontinuity. This cannot be represented adequately by the basis functions and thus especially in systems in which the auxiliary volumes have to be large, a second approach can lead to higher accuracy. In this second method the interstitial potential is simply continued into the auxiliary region leading to a smooth total potential. In that case one has to solve the problem for region II using the same numerical approach as for region I except that one can use pure plane-waves as basis functions due to the fact that no muffin-tins are contained within region II.

6.5 Construction of the Hamiltonian

The construction of the FLAPW Hamiltonian of region I consists of several parts. The starting point is the embedding Hamiltonian as defined in Eqs. (4.16) and (4.17)

$$H_{\text{emb}}(\vec{r}) = -\frac{1}{2}\nabla^2 + V(\vec{r}) + \delta(n - n_s) \left[\frac{1}{2} \frac{\partial}{\partial n_s} + G_S^{-1} \right], \quad (6.24)$$

where G_S^{-1} denotes the non-local integral operator of the embedding potential which will be dealt with in the next section. Hence, one first has to construct the matrix elements of

$$H_0(\vec{r}) = -\frac{1}{2}\nabla^2 + V(\vec{r}) + \delta(n - n_s) \frac{1}{2} \frac{\partial}{\partial n_s}. \quad (6.25)$$

When evaluating the corresponding integrals over region I

$$H_0^{\vec{g}\vec{g}'} = \int_{\text{I}} \phi_{\vec{g}}^*(\vec{r}) H_0(\vec{r}) \phi_{\vec{g}'}(\vec{r}) dV \quad (6.26)$$

one can first use Green's theorem

$$\int (\nabla \phi_{\vec{g}}(\vec{r}))^* \nabla \phi_{\vec{g}'}(\vec{r}) dV = \int \phi_{\vec{g}}^*(\vec{r}) \nabla^2 \phi_{\vec{g}'}(\vec{r}) dV - \int \phi_{\vec{g}}^*(\vec{r}) \frac{\partial}{\partial n_s} \phi_{\vec{g}'}(\vec{r}) dS \quad (6.27)$$

to transform Eq. (6.26) to

$$H_0^{\vec{g}\vec{g}'} = \int \left[-\frac{1}{2} (\nabla \phi_{\vec{g}}(\vec{r}))^* \nabla \phi_{\vec{g}'}(\vec{r}) + \phi_{\vec{g}}^*(\vec{r}) V(\vec{r}) \phi_{\vec{g}'}(\vec{r}) \right] dV. \quad (6.28)$$

This transformation to include the normal derivative at the boundary by modifying the kinetic energy operator of the Hamiltonian, is used in the same way as in the APW method. In the APW method the fact that the basis functions can only assumed to be continuous at the muffin-tin boundaries and that no continuity of the derivative can be imposed, leads to the appearance of the same surface terms in

the Hamiltonian as in Eq. (6.28) when one interprets the surface S as the muffin-tin boundary.

The matrix elements of the Hamiltonian and those of the overlap matrix $S_{\vec{k}_{\parallel}}^{\vec{g}\vec{g}'}$ = $\int_{\text{I}} \phi_{\vec{g}\vec{k}_{\parallel}}^*(\vec{r}) \phi_{\vec{g}'\vec{k}_{\parallel}}(\vec{r}) dV$ can now be evaluated by splitting the volume integral into two different integrals, one over the muffin-tin spheres and the other over the remaining interstitial region of region I.

Concluding, the matrix elements of the overlap matrix given by

$$\begin{aligned} S^{\vec{g}\vec{g}'} &= \frac{1}{\tilde{d}A} \int_{\text{I}} \theta_1(\vec{r}) e^{-i(\vec{g}-\vec{g}')\vec{r}} dV \\ &= \tilde{\theta}_1(\vec{g}' - \vec{g}), \end{aligned} \quad (6.29)$$

where $\tilde{\theta}_1(\vec{g}' - \vec{g})$ is the Fourier transform of the first step function defined. Combining Eqs. (6.28) and (6.19) one obtains the matrix elements of the Hamiltonian in the interstitial region

$$\begin{aligned} H_{0,\vec{k}_{\parallel}}^{\vec{g}\vec{g}'} &= \int_{\text{I}} \frac{1}{2} (\vec{k}_{\parallel} + \vec{g})(\vec{k}_{\parallel} + \vec{g}') \theta_1(\vec{r}) e^{-i(\vec{g}-\vec{g}')\vec{r}} dV + V_{\text{int}}^{\vec{g}\vec{g}'} \\ &= \frac{1}{2} (\vec{k}_{\parallel} + \vec{g})(\vec{k}_{\parallel} + \vec{g}') S^{\vec{g}\vec{g}'} + V_{\text{int}}^{\vec{g}\vec{g}'} . \end{aligned} \quad (6.30)$$

A very detailed description of the actual calculations of the matrix elements in the muffin-tin spheres can be found in [Kur01]. The embedding method actually does not modify the FLEUR code generating these matrix elements, except that the APW-version of the routines must be used. This version modifies the calculation of the matrix elements of the kinetic energy in the muffin-tin spheres to take the different form of the kinetic energy operator into account. By making use of Eq. (6.27) these matrix elements are calculated by evaluating $\int_{\text{MT}} \phi_{\vec{g}}^*(\vec{r}) \nabla^2 \phi_{\vec{g}'}(\vec{r}) dV$ as described in Ref. [Kur01] and adding the integrals $-\int \phi_{\vec{g}}^*(\vec{r}) \frac{\partial}{\partial n_S} \phi_{\vec{g}'}(\vec{r}) dS$ over the surfaces of the muffin-tin spheres which can easily be expressed in terms of the normal derivative of the radial functions.

6.6 Calculation of the Green Function

After the FLAPW Hamiltonian and the overlap matrices have been constructed, Eq. (4.18) defining the Green function to the embedding Hamiltonian transforms into a matrix equation for the Green function matrix that can be calculated by a straight forward matrix inversion for each \vec{k}_{\parallel} -point in the two-dimensional Brillouin-

zone and each energy grid-point ϵ

$$G_{\vec{k}_{\parallel}, \epsilon}^{\vec{g}\vec{g}'}[n] = \left[\epsilon S_{\vec{k}_{\parallel}}^{\vec{g}\vec{g}'}[n] - H_{0, \vec{k}_{\parallel}}^{\vec{g}\vec{g}'}[n] - (G_S^{-1})_{\vec{k}_{\parallel}, \epsilon}^{\vec{g}\vec{g}'} \right]^{-1}, \quad (6.31)$$

where $(G_S^{-1})_{\vec{k}_{\parallel}, \epsilon}^{\vec{g}\vec{g}'}$ denote the matrix elements of the embedding potentials of the two surfaces. It should be noted, that S and H , and thus also G , depend on the charge density n and change during self-consistency iterations. According to Eq. (4.16) these matrix elements are defined by

$$(G_S^{-1})_{\vec{k}_{\parallel}, \epsilon}^{\vec{g}\vec{g}'} = \sum_{S=L,R} \int_I \phi_{\vec{g}\vec{k}_{\parallel}}(\vec{r})^* \delta(n - n_S) \delta(n' - n_S) G_S^{-1}(\vec{r}, \vec{r}'; \vec{k}_{\parallel}, \epsilon) \phi_{\vec{g}'\vec{k}_{\parallel}}(\vec{r}') dV dV', \quad (6.32)$$

which can be written as

$$(G_S^{-1})_{\vec{k}_{\parallel}, \epsilon}^{\vec{g}\vec{g}'} = \frac{1}{\tilde{d}} \left[e^{-i g_z z_L} e^{i g'_z z_L} G_{S_L}^{-1}(\vec{g}_{\parallel}, \vec{g}'_{\parallel}; \vec{k}_{\parallel}, \epsilon) + e^{-i g_z z_R} e^{i g'_z z_R} G_{S_R}^{-1}(\vec{g}_{\parallel}, \vec{g}'_{\parallel}; \vec{k}_{\parallel}, \epsilon) \right], \quad (6.33)$$

by using the interstitial representation of the LAPW basis functions and the expansion of the embedding potential into the two-dimensional plane wave basis set

$$G_S^{-1}(\vec{r}_{\parallel}, \vec{r}'_{\parallel}; \vec{k}_{\parallel}, \epsilon) = \sum_{\vec{g}_{\parallel}, \vec{g}'_{\parallel}} e^{i \vec{g}_{\parallel} \vec{r}_{\parallel}} G_S^{-1}(\vec{g}_{\parallel}, \vec{g}'_{\parallel}; \vec{k}_{\parallel}, \epsilon) e^{-i \vec{g}'_{\parallel} \vec{r}'_{\parallel}}. \quad (6.34)$$

The inversion in Eq. (6.31) is computationally the most expensive part of the Green function version of the FLEUR code. The number of operations scales proportional to N^3 , N being the total number of \vec{g} -vectors. It is in principle similarly expensive as the matrix diagonalization in a standard FLAPW calculation, although the matrix diagonalisation is generally cheaper as only a few eigenvectors are calculated in the diagonalization. Furthermore, as one can see from Eq. (6.33) the matrix of the embedding potential $(G_S^{-1})_{\vec{k}_{\parallel}}^{\vec{g}\vec{g}'}$ is a complex matrix even in cases in which the Hamiltonian and the overlap matrix are real. Such a real Hamiltonian can be chosen in systems having inversion symmetry. Thus, in the Green function code one has to invert a general complex matrix not being hermitian or of any other simpler form, which increases the requirement for computer time as well as the memory needed to store the matrices.

In some instances it might be computational advantageous to interpret the de-

termination of $G_{\vec{k}_{\parallel}, \epsilon}^{\vec{g}\vec{g}'}[n]$ in terms of a set of linear equations

$$\left[\epsilon S_{\vec{k}_{\parallel}}^{\vec{g}\vec{g}'}[n] - H_{0, \vec{k}_{\parallel}}^{\vec{g}\vec{g}'}[n] - (G_S^{-1})_{\vec{k}_{\parallel}, \epsilon}^{\vec{g}\vec{g}'} \right] G_{\vec{k}_{\parallel}, \epsilon}^{\vec{g}\vec{g}'}[n] = \delta^{\vec{g}\vec{g}'}. \quad (6.35)$$

For example this can be that case during self-consistency iterations where the charge density and magnetisation density change. Assume the Green function $G_0[n_0]$ is known for a charge density n_0 , which is not yet the self-consistent one. Then any improved charge density $n = n_0 + \Delta n$ changes the Hamiltonian to $H_0 + \Delta H$, the overlap matrix to $S_0 + \Delta S$. The Green function $G[n_0 + \Delta n]$ may then be calculated according to

$$[1 + G^0(\epsilon \Delta S - \Delta H)] G[n] = G^0 \quad (6.36)$$

using a basis set with a reduced number of basis functions.

Except for the self-consistency, only the projections of the total, three-dimensional Green function are needed. These projections are given in the following form

$$G_{bb'}(\vec{g}_{\parallel}, \vec{g}'_{\parallel}) = \frac{1}{A} \sum_{g_z g'_z} e^{i g_z z_b} G(\vec{g}, \vec{g}') e^{-i g'_z z_{b'}}. \quad (6.37)$$

One should note that these matrices of the boundary surface Green-functions $G_{bb'}$ are contractions of the total Green-function matrix over the basis functions describing the variational degrees of freedom normal to the surface S . These matrices $G_{bb'}$ are defined only in the two-dimensional basis with N_{\parallel} basis functions and therefore are considerably smaller than the total Green function matrix ($N_{\parallel} \sim N^{2/3}$). Beside these projections all further two-dimensional quantities like the embedding potential and the T-matrix are defined within this much smaller basis set and no significant computer time must be spend in any of the parts of the code calculating the complex bandstructure or evaluating the equations for the conductance.

6.7 The Transfer-Matrix

Using the projections of the Green function $G_{bb'}(\vec{g}_{\parallel}, \vec{g}'_{\parallel})$ calculated with zero embedding potential to obtain a Green function with von-Neumann boundary condition, one can very easily apply Eq. (5.13) to calculate the T-matrix. Due to the presence of the additional auxillary volumes, the T-matrix in both region I and II is calculated. Here a short discussion of the significance of these T-matrices might be appropriate. The T-matrix is a linear operator. Therefore, if one has several slab-like volumes which are connected by common boundaries as in the case of re-

gion I consisting of volume Ω and the two auxillary volumes Δ_L and Δ_R , one can construct a T-matrix of the total system by simple multication of the T-matrices of the individual subvolumes. Hence, one can write

$$\begin{aligned} T_I &= T_{\Delta_R} T_{\Omega} T_{\Delta_L} \\ T_{II} &= T_{\Delta_R} T_{\Delta_L}, \end{aligned} \quad (6.38)$$

for the T-matrices of region I and II, respectively. Of course, these submatrices are never actually calculated. Strictly speaking the T-matrix of interest is neither T_I nor T_{II} , but T_{Ω} since this is the quantity which contains the physical region Ω . Instead of T_{Ω} one can define

$$T = T_I T_{II}^{-1} = T_{\Delta_R} T_{\Omega} T_{\Delta_R}^{-1}. \quad (6.39)$$

As the matrix T_{Δ_R} is not singular, the matrices T and T_{Ω} are related by a similarity transformation. The eigenvalues of the matrices T and T_{Ω} are identical, i.e. the matrix T can be used to obtain the complex bandstructure. This can easily be derived from the eigenvalue equation

$$T\Psi = T_{\Delta_R} T_{\Omega} T_{\Delta_R}^{-1} \Psi = \lambda \Psi, \quad (6.40)$$

by multiplication with $T_{\Delta_R}^{-1}$

$$T_{\Omega} T_{\Delta_R}^{-1} \Psi = \lambda T_{\Delta_R}^{-1} \Psi. \quad (6.41)$$

One can now identifying $T_{\Delta_R}^{-1} \Psi$ with the eigenvectors of T_{Ω} . Hence, the eigenvectors Ψ of T are simply those of T_{Ω} transfered by T_{Δ_R} to the boundary plane S_R^{II} . Applying the matrix T_{II}^{-1} on the eigenvectors Ψ they can be transfered to the boundary plane S_L^{II} which can be identified with the boundary plane S_L^I . Hence using the matrices T_I and T_{II} , one constructs the matrix T , whose eigenvectors on the planar surfaces S_L^I and S_R^I of the setup shown in Fig. 6.3 correspond to the vector of boundary values associated with the complex bandstructure of region Ω only. Correspondingly, all argument presented so far hold, if the T -matrix is defined according to Eq. (6.39). The additional transfer to the planar surfaces can be viewed as a pure simplification. Due to the construction of the embedding potential from the eigenvectors of the T -matrix the same transfer is applied to the embedding potential later on, i.e. the embedding potential is also constructed on the planar surfaces.

Some extra care has to be taken when the lattice vector \vec{d} is not normal to the sur-

face S , i.e. when its projection \vec{d}_{\parallel} onto the surface S does not vanish. This leads to a phaseshift of the two-dimensional plane-wave basis functions between the two surfaces of Ω . In this case an additional phase matrix $P(\vec{g}_{\parallel}, \vec{g}'_{\parallel}) = \delta_{\vec{g}_{\parallel}, \vec{g}'_{\parallel}} \exp(i\vec{g}_{\parallel} \vec{d}_{\parallel})$ is included in both the generalized Bloch condition $T\Psi = \lambda P\Psi$ and in $T_{II} = P^{-1}T_{\Delta_R} P T_{\Delta_L}$.

Using a two-dimensional basis set consisting of N_{\parallel} plane-waves both $\psi(\vec{r}_b)$ and $\partial_n \psi(\vec{r}_b)$ are expressed as a vector of N_{\parallel} components. Since the T -matrix acts on the combined vector of boundary values (Eq. (5.1)) it is a $(2N_{\parallel} \times 2N_{\parallel})$ -matrix. Correspondingly, it has $2N_{\parallel}$ eigenvectors each of dimension $2N_{\parallel}$. According to Eq. (5.1) these eigenvectors specify the vectors of boundary conditions for the eigenstates of the T -matrix in region I. By construction, the first N_{\parallel} components of the eigenvectors form the plane-wave representation $\psi(\vec{g}_{\parallel})$ of $\psi(\vec{r}_b)$ and the second N_{\parallel} components form the plane-wave expansion coefficients $\partial_n \psi(\vec{g}_{\parallel})$ of $\partial_n \psi(\vec{r}_b)$. One can write these boundary values for each eigenvalue $\lambda(\vec{k}_{\parallel}, \epsilon)$ of the T -matrix concisely in the form defined by Eq. 5.1 as

$$\Psi_{\lambda(\vec{k}_{\parallel}, \epsilon)} = \begin{pmatrix} \Psi_1 \\ \dots \\ \Psi_{N_{\parallel}} \\ \Psi_{N_{\parallel}+1} \\ \dots \\ \Psi_{2N_{\parallel}} \end{pmatrix}_{\lambda(\vec{k}_{\parallel}, \epsilon)} = \begin{pmatrix} \psi(\vec{g}_{\parallel}^1) \\ \dots \\ \psi(\vec{g}_{\parallel}^{N_{\parallel}}) \\ \partial\psi(\vec{g}_{\parallel}^1) \\ \dots \\ \partial\psi(\vec{g}_{\parallel}^{N_{\parallel}}) \end{pmatrix}_{\lambda(\vec{k}_{\parallel}, \epsilon)}. \quad (6.42)$$

6.8 Embedding Potential

Having obtained the T -matrix, its eigenvalues and eigenvectors one can classify the different sets of states as described in section 5.2. Most easily is the identification of the evanescent states, since these can be separated on the basis of the corresponding eigenvalues λ of the T -matrix. For the calculation of the embedding potential on the left hand side boundary plane one collects those evanescent states ($|\lambda| \neq 1$) with $|\lambda| > 1$ since these states decay to the left. Additionally, one has to indentify from the Bloch states ($|\lambda| = 1$) those states, which propagate to the left by evaluating the current of these states perpendicular to the plane. The current j through the boundary planes per area of the surface unit cell of each eigenstate labeled by λ is

given by Eq. (5.29), which is written in the plane-wave basis as

$$j_\lambda = \Im \int \left(\begin{array}{c} \Psi_1 \\ \dots \\ \Psi_{N_\parallel} \end{array} \right)_\lambda^\dagger \left(\begin{array}{c} \Psi_{N_\parallel+1} \\ \dots \\ \Psi_{2N_\parallel} \end{array} \right)_\lambda dS. \quad (6.43)$$

It should be negative for Bloch states propagating to the left. Recalling the discussion of section 5.2 there exist always pairs of eigenvalues with $\lambda\lambda' = 1$. Thus N_\parallel boundary values Ψ_λ will correspond to states propagating or decaying to the right and N_\parallel to the left. Combining all left propagating Bloch states and evanescent states decaying to the left, one can define the two matrices needed for the calculation of the embedding potential

$$[\psi] = \left(\begin{array}{ccc} \Psi_1^1 & \dots & \Psi_1^{N_\parallel} \\ \dots & & \dots \\ \Psi_{N_\parallel}^1 & \dots & \Psi_{N_\parallel}^{N_\parallel} \end{array} \right) \text{ and } [\partial\psi] = \left(\begin{array}{ccc} \Psi_{N_\parallel+1}^1 & \dots & \Psi_{N_\parallel+1}^{N_\parallel} \\ \dots & & \dots \\ \Psi_{N_\parallel+N_\parallel}^1 & \dots & \Psi_{N_\parallel+N_\parallel}^{N_\parallel} \end{array} \right), \quad (6.44)$$

where the superscripts runs over all N_\parallel states propagating/decaying to the left. These matrices are $(N_\parallel \times N_\parallel)$ non-singular matrices which can be used to obtain the $(N_\parallel \times N_\parallel)$ matrix of the embedding potential according to Eq. (5.25).

6.9 Construction of the Charge Density

In a numerical application, the energy integration of Eq. (4.25) is transformed into a sum over discrete energy points z_n with corresponding weights w_n and finally the charge density $n(\vec{r})$ in the region Ω is calculated as

$$n(\vec{r}) = -\frac{1}{\pi} \Im \sum_n w_n G(\vec{r}, \vec{r}; z_n). \quad (6.45)$$

The energy points z_n are now chosen on a circle in the complex energy plane which encloses all occupied states. The energy points z_n and the weights w_n are constructed according to a modified Gauss-Chebyshev technique. As the LAPW basis is independent of the energy z at which the Green function is evaluated, this summation can be performed for all the energies z_n for each \vec{k}_\parallel used in the \vec{k}_\parallel -integration. In the following, the \vec{k}_\parallel -index will be suppressed having in mind that actually all quantities are subject to a standard two-dimensional \vec{k}_\parallel -integration in the end. Thus, one

starts with an energy-integrated Green-function matrix

$$G = \sum_n w_n G(z_n). \quad (6.46)$$

The calculation of the charge density can now be carried out for the interstitial region and the muffin-tin spheres independently which will be discussed now. For the sake of a readable presentation, the use of a symmetry-adapted representation of the density will not be introduced and no extra indices will be defined for the bookkeeping of different muffin-tin spheres.

6.9.1 Interstitial region

In the interstitial of region Ω , the Green function is expressed in a plane-wave representation. The charge density will also be expanded into plane-waves, with their \vec{g} -vectors taken from the reciprocal lattice but from a sphere in reciprocal space with a diameter larger than twice the largest \vec{g} -vector used for the Green function. Thus, one starts with the following two equations for the charge density $n(\vec{r})$ expressed by the imaginary part of the Green function

$$\begin{aligned} n(\vec{r}) &= -\frac{1}{\pi V} \Im \sum_{\vec{g}\vec{g}'} e^{i(\vec{g}+\vec{k})\vec{r}} \tilde{G}(\vec{g}, \vec{g}') e^{-i(\vec{g}'+\vec{k})\vec{r}} \\ &= -\frac{1}{\pi V} \Im \sum_{\vec{g}\vec{g}'} e^{i(\vec{g}-\vec{g}')\vec{r}} \tilde{G}(\vec{g}, \vec{g}') \\ &= -\frac{1}{2i\pi V} \sum_{\vec{g}\vec{g}'} e^{i(\vec{g}-\vec{g}')\vec{r}} \tilde{G}(\vec{g}, \vec{g}') - e^{-i(\vec{g}-\vec{g}')\vec{r}} \tilde{G}^*(\vec{g}, \vec{g}') \end{aligned} \quad (6.47)$$

and the charge density expansion into plane waves

$$n(\vec{r}) = \frac{1}{V} \sum_{\vec{g}} e^{i\vec{g}\vec{r}} n(\vec{g}). \quad (6.48)$$

Comparing these two equation one obtains an expression for $n(\vec{g})$. For easier notation, one first defines the contraction

$$\tilde{G}(\vec{g}'') = \sum_{\vec{g}-\vec{g}'=\vec{g}''} \tilde{G}(\vec{g}, \vec{g}'). \quad (6.49)$$

Now the expansion coefficients for the interstitial charge density is given by

$$n(\vec{g}) = -\frac{1}{2i\pi} \left(\tilde{G}(\vec{g}) - \tilde{G}^*(-\vec{g}) \right). \quad (6.50)$$

6.9.2 Muffin-tin spheres

The charge density in the muffin-tin spheres of region Ω is expanded in terms of spherical harmonics Y_{lm} and given in a local coordinate system centered at the muffin-tin sphere under consideration

$$n(\vec{r}) = \sum_{lm} n_{lm}(r) Y_{lm}(\hat{r}), \quad (6.51)$$

where the vector \vec{r} in this local coordinate system has been decomposed into a unit-vector \hat{r} being relative to the muffin-tin center and a scalar r measuring the distance to this center. The expansion coefficients $n_{lm}(r)$ become dependent on the orbital quantum numbers l and m and the distance r for which the same radial mesh will be used as for the LAPW-basis functions. The fact that not only the $l = 0$ component of the charge is used in the potential generation is a typical feature of a full-potential method.

The diagonal part of the (energy integrated) Green function in the muffin-tins is given by

$$\begin{aligned} \tilde{G}(\vec{r}, \vec{r}) = \sum_{\vec{g}, \vec{g}'} \sum_{lm} \sum_{l'm'} & \left[A_{lm}^{\vec{g}} u_l(r) Y_{lm}(\hat{r}) + B_{lm}^{\vec{g}} \dot{u}_l(r) Y_{lm}(\hat{r}) \right]^* \tilde{G}(\vec{g}, \vec{g}') \times \\ & \left[A_{l'm'}^{\vec{g}'} u_{l'}(r) Y_{l'm'}(\hat{r}) + B_{l'm'}^{\vec{g}'} \dot{u}_{l'}(r) Y_{l'm'}(\hat{r}) \right], \end{aligned} \quad (6.52)$$

where the \vec{k} -dependence has not been explicitly denoted in the A and B coefficients.

First one transforms the Green function matrix to the orbital basis by the following definitions

$$\tilde{G}_{lm'l'm'}^{AA} = \sum_{\vec{g}, \vec{g}'} A_{lm}^{*\vec{g}} \tilde{G}(\vec{g}, \vec{g}') A_{l'm'}^{\vec{g}'}, \quad (6.53)$$

$$\tilde{G}_{lm'l'm'}^{AB} = \sum_{\vec{g}, \vec{g}'} A_{lm}^{*\vec{g}} \tilde{G}(\vec{g}, \vec{g}') B_{l'm'}^{\vec{g}'}, \quad (6.54)$$

$$\tilde{G}_{lm'l'm'}^{BA} = \sum_{\vec{g}, \vec{g}'} B_{lm}^{*\vec{g}} \tilde{G}(\vec{g}, \vec{g}') A_{l'm'}^{\vec{g}'}, \quad (6.55)$$

$$\tilde{G}_{lm'l'm'}^{BB} = \sum_{\vec{g}, \vec{g}'} B_{lm}^{*\vec{g}} \tilde{G}(\vec{g}, \vec{g}') B_{l'm'}^{\vec{g}'}. \quad (6.56)$$

To determine the coefficients $n_{lm}(r)$ one can use the orthogonality relation of the Y_{lm} when integrated over the whole solid angle

$$\int Y_{lm}(\hat{r}) Y_{l'm'}(\hat{r}) d\Omega = \delta_{l,l'} \delta_{m,m'}. \quad (6.57)$$

With the Gaunt coefficients defined as

$$C_G(l, l', l''; m, m', m'') = \int Y_{lm}^*(\hat{r}) Y_{l'm'}(\hat{r}) Y_{l''m''}(\hat{r}) d\Omega \quad (6.58)$$

one obtains

$$\begin{aligned} n_{l''m''}(r) = & \frac{-1}{\pi} \left[\sum_{lm} \sum_{l'm'} \Im \left(C_G(l, l', l''; m, m', m'') \tilde{G}_{lm'l'm'}^{AA} \right) u_l(r) u_{l'}(r) \right. \\ & + \sum_{lm} \sum_{l'm'} \Im \left(C_G(l, l', l''; m, m', m'') \tilde{G}_{lm'l'm'}^{AB} \right) u_l(r) \dot{u}_{l'}(r) \\ & + \sum_{lm} \sum_{l'm'} \Im \left(C_G(l, l', l''; m, m', m'') \tilde{G}_{lm'l'm'}^{BA} \right) \dot{u}_l(r) u_{l'}(r) \\ & \left. + \sum_{lm} \sum_{l'm'} \Im \left(C_G(l, l', l''; m, m', m'') \tilde{G}_{lm'l'm'}^{BB} \right) \dot{u}_l(r) \dot{u}_{l'}(r) \right] \quad (6.59) \end{aligned}$$

In deriving this equation one has to use the fact that the Gaunt coefficients are real numbers and that $C_G(l', l, l''; m', m, m'') = C_G(l, l', l''; m, m', m'')$. Hence for any complex c one has

$$\begin{aligned} \int \Im (c Y_{lm}^* Y_{l'm'}) Y_{l''m''} d\Omega &= \frac{1}{2i} \left(\int c Y_{lm}^* Y_{l'm'} Y_{l''m''} d\Omega - \int c^* Y_{lm} Y_{l'm'}^* Y_{l''m''} d\Omega \right) \\ &= \frac{1}{2i} (c C_G(l, l', l''; m, m', m'') - c^* C_G(l', l, l''; m', m, m'')) \\ &= \Im (c C_G(l, l', l''; m, m', m'')). \quad (6.60) \end{aligned}$$

Besides the calculation of the Green-function matrix by matrix inversion, the calculation of the non-spherical charge density is the second expensive part in the self-consistency cycle of a FLAPW Green function method as it scales proportional to $N_{\text{at}} l_{\text{max}}^6 N^2$, where N_{at} is the number of inequivalent atoms in the unit cell. A significant speedup can be gained by exploiting the point group symmetry of the atom as the contractions Eqs. (6.53-6.56) will be only carried out for the irreducible representation.

6.10 Potential Setup

In a self-consistent embedding scheme the potential in the region Ω must be calculated from the obtained charge density. In the DFT the potential consists of two density-dependent contributions: the Coulomb or Hartree potential V_H and the exchange-correlation potential V_{xc} . In the LDA and GGA the exchange-correlation

potential is local in the density and the derivative of the density and no difference exists to standard FLAPW methods to evaluate this contribution. However, the Coulomb potential requires some additional care as this contribution is non-local and therefore the effect of the outer volume has to be taken into account. The remaining of this section therefore describes the calculation of the Coulomb potential. In practice, this contribution to the potential is obtained by solving boundary value problem of the Poisson equation with the boundary condition given by the potential of the outer volume. In detail, this boundary condition is the value of the Coulomb potential at both curved boundary surfaces of region Ω .

To demonstrate the algorithm for the construction of the Coulomb potential, first the interstitial region is considered. Analogously to the film calculation (see Ref. [Kur01]) the charge in the muffin-tin spheres is replaced by a pseudo-charge having the same multipole moments to obtain a charge n_{pseudo} in all space which equals the true charge in the interstitial of region Ω . Using this charge, the Poisson equation is solved

$$\Delta V_{H,\text{Int}}^0(\vec{r}) = 4\pi n_{\text{pseudo}}(\vec{r}). \quad (6.61)$$

This can be done most easily in Fourier space by

$$V_{H,\text{Int}}^0(\vec{g}) = 4\pi \frac{n_{\text{pseudo}}(\vec{g})}{|\vec{g}|^2} \text{ for } \vec{g} \neq 0. \quad (6.62)$$

While this potential $V_{H,\text{int}}^0$ solves the Poisson equation for the correct interstitial charge in Ω , in general it does not fulfill the required boundary condition. As mentioned above, the following condition must be satisfied for the Coulomb potential on the curved boundary \tilde{S}_b of region Ω

$$V_H(\vec{r}_b) = V_H^{\text{bulk}}(\vec{r}_b), \quad (6.63)$$

where $V_H^{\text{bulk}}(\vec{r}_b)$ is Coulomb potential of the attached bulk volumes. To satisfy this condition, $V_{H,\text{Int}}^0$ must be corrected by a solution $V_{H,\text{Int}}^1$ of the homogeneous Poisson equation

$$\Delta V_{H,\text{Int}}^1(\vec{r}) = 0. \quad (6.64)$$

This solution is constructed such that it satisfies the boundary condition

$$V_{H,\text{Int}}^1(\vec{r}_b) = V_H^{\text{bulk}}(\vec{r}_b) - V_{H,\text{Int}}^0(\vec{r}_b), \quad (6.65)$$

on the boundary \tilde{S}_b . In order to calculate $V_{H,\text{Int}}^1$ the following approach is imple-

mented: The homogeneous Poisson equation can be solved easily if the boundary condition would be specified on the planar surfaces S_b . Using a two-dimensional Fourier transform, the solutions of Eq. (6.64) are given in this case by

$$V_H^1(\vec{g}_{\parallel}, z) = \begin{cases} a z + b & \text{for } \vec{g}_{\parallel} = 0 \\ a e^{|\vec{g}_{\parallel}|z} + b e^{-|\vec{g}_{\parallel}|z} & \text{for } \vec{g}_{\parallel} \neq 0, \end{cases} \quad (6.66)$$

where the coefficients a and b must be chosen independently for each \vec{g}_{\parallel} to fulfill the boundary condition on the planar surfaces. To solve Eq. (6.64) with the boundary conditions given by Eq. (6.65) on \tilde{S}_b one solves iteratively the non-linear problem defined by

$$\text{boundary condition on } S_b \rightarrow V_{H,\text{Int}}^1 \rightarrow \text{potential values on } \tilde{S}_b,$$

i.e. one searches for a boundary condition on the planar surface S_b which leads to the same solution of Eq. (6.64) within region Ω . Once this boundary condition on S_b is found, the sum $V_{H,\text{Int}} = V_{H,\text{Int}}^0 + V_{H,\text{Int}}^1$ solves the boundary value problem of the Poisson equation with the correct charge density and the correct boundary values V_H^{bulk} in the interstitial of region Ω . The Coulomb potential within the muffin-tin spheres of region Ω can then be determined by using $V_{H,\text{Int}}$ as a boundary condition as in usual film FLAPW calculations [Kur01].

Codes in which such an approach has successfully been implemented exist and on this basis the self-consistent calculation of surfaces of semi-infinite crystals has been performed.

Chapter 7

First results

To demonstrate the methods and ideas introduced so far I will now present and discuss some results for test systems. However, before the results are discussed, the first section of this chapter will give some instructions or recipes how to actually apply the code and how all the different formulas and ideas presented so far interoperate. The focus then will switch to the calculation of the complex bandstructures. A special focus will be the requirement to modify the construction of the basis set in T-matrix calculations. Finally, the conductance of some simple systems will be studied and the differences obtained in using the Landauer formula or Bardeen's approach for tunneling will be demonstrated.

7.1 Some Recipes

Up to now a lot of different topics like the fundamentals of electronic transport, its formulation using the embedding method, the T-matrix formalism, the complex bandstructure and details of the implementation have been discussed. It might be appropriate to show how all these bits and pieces are linked together and to give some recipes for actual calculations of the conductance of a realistic system. In general the following procedure is applied to calculate the conductance:

1. The potential used to calculate the FLAPW Hamiltonian is obtained using a supercell setup. As discussed in section 4.1 the potential and the charge density rapidly approach their bulk values at short distance from the interface. Therefore, the potential of the interface region Ω containing the actual barrier or the monolayers of non-bulk material with some additional buffer monolayers of the leads attached can easily be obtained from a supercell setup as indicated

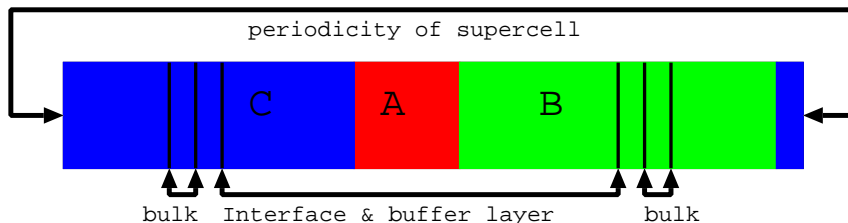


Figure 7.1: Symbolic supercell setup. The material A is sandwiched between materials B and C. This stacking is repeated periodically. The interface region containing material A and buffer volumes of bulk material can be cut from this. Both bulk potential for materials B and C can also be obtained.

in Fig. 7.1. After this bulk system is converged in a standard FLAPW calculation performed with the FLEUR code the (possibly spin-dependent) potential of the interface region can be cut from the total supercell. Additionally, the potential from a bulk-like layer of the lead materials can be obtained which extends the potential of the interface region smoothly to the left or right.

2. In a second step the potential of the bulk is used to create the FLAPW Hamiltonian of a principle layer of bulk material. Using this Hamiltonian H and the corresponding overlap matrix S and adding zero embedding potential G_S^1 on both boundary surfaces, the Green function of the bulk principle layer with von-Neumann boundary condition can be obtained by inverting $z*S - H - G_S^{-1}$ as described in chapter 6. Again one should note that in this procedure the Green function will depend on the energy z and the parallel \vec{k}_{\parallel} vector and that therefore this inversion has to be performed for every energy and \vec{k}_{\parallel} vector in question. Using the projections of the Green function onto the embedding planes one can obtain the T-matrix and from this the complex bandstructure and the embedding potential. This procedure is shown symbolically in the left part of Fig. 7.2. The key result is of course the embedding potential of the bulk systems, but in principle also the boundary vectors of the states of the complex bandstructure, i.e. the eigenvectors of the T-matrix, can be used for wavefunction matching or the calculation of non-equilibrium charge densities as shortly discussed in section 4.7. Furthermore the complex bandstructure itself can be of interest even though in most cases the complex bandstructure of the barrier material and not of the bulk electrodes is more useful when discussing the transmission properties in terms of the evanescent states in the barrier.
3. In the third step one now calculates the Green function of the interface region.

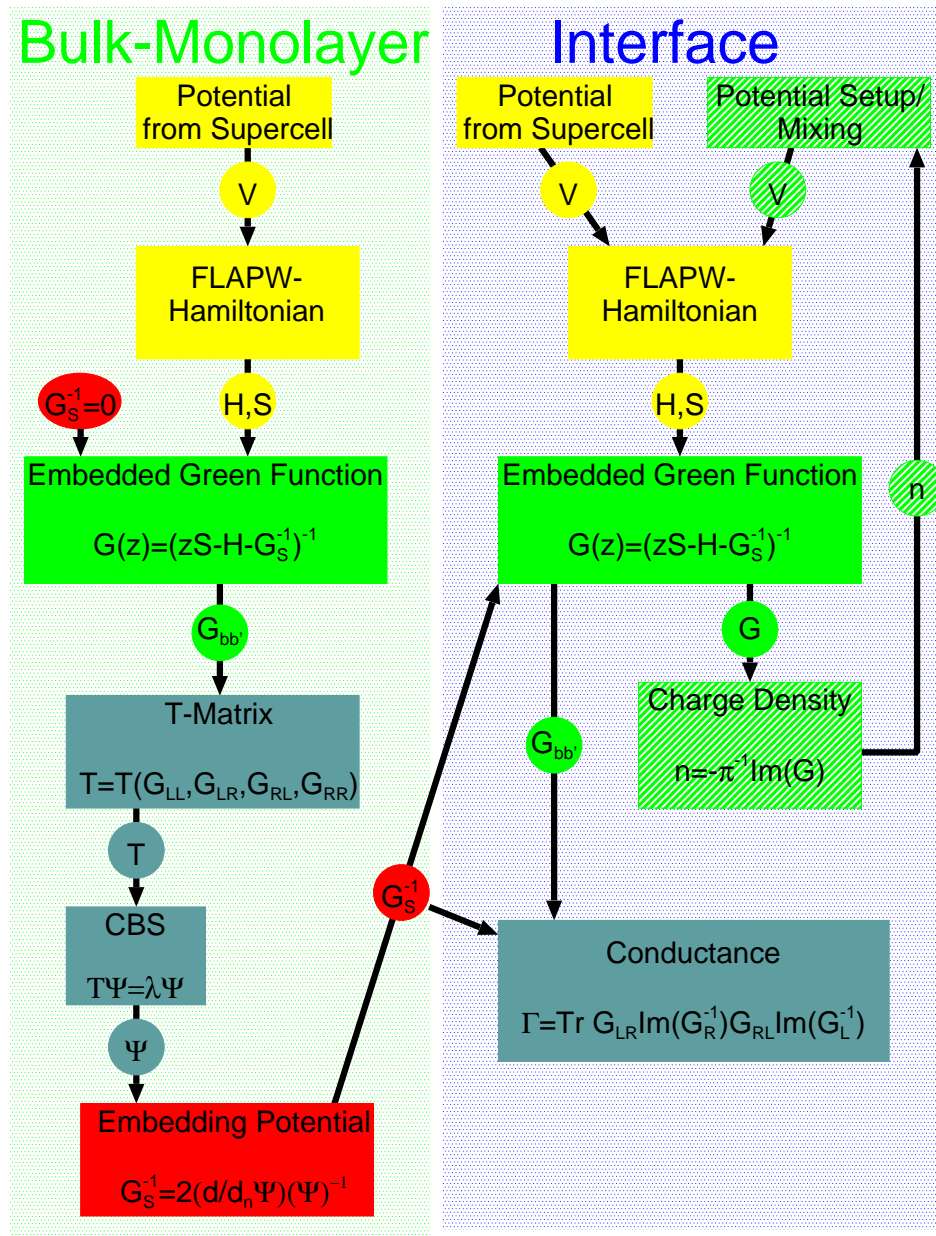


Figure 7.2: Symbolical representation of conductance calculation. See text for details.

The Hamiltonian setup is analogous to the procedure discussed in step 2 except of course the use of a different potential. The Green function, however, is not calculated with zero embedding potential but instead the embedding potential of the bulk leads as obtained in step 2 is added to obtain the Green function of the interface sandwiched between the two semi-infinite leads. One should note, that even though the potential was calculated from a supercell in step 1, the Green function one obtains here is the Green function corresponding to a system without artificial periodicity perpendicular to the interface. The only approximation made is the restriction of the perturbation of the potential to the interface region. But as some buffer layers can be included this approximation is reasonable and its effect on the final results can easily be neglected. The projections of the Green function obtained in this step can now be used for the calculation of the ballistic conductance using Eq. (5.42). Alternatively, if the interface calculated in this step is actually the interface between a metal and a semi-infinite barrier region the embedding potential of the barrier and the surface projection of the Green function onto the embedding surface on the barrier side can be used to obtain the conductance according the Bardeen's formula as reformulated in Eq. (5.58). These steps are visualized on the right hand side of Fig. 7.2. Additionally, as discussed in section 4.7 the Green function of the interface can be used to calculate the charge density and from this a new potential for the embedded volume can be constructed. Driving this procedure to self consistency would remove the approximation imposed by the use of the supercell potential, but much more important, it could be used to construct the non-equilibrium charge density for an junction with an applied bias voltage.

7.2 Complex Bandstructures

The first test case to study is the calculation of different complex bandstructures. In order to obtain a complex bandstructure the procedure visualized on the left hand side of Fig. 7.2 is applied.

I will now present three examples of complex bandstructure calculations. The simplest example is the complex bandstructure of free electrons. The complex bandstructure of Cu, which will be discussed afterwards, has been extensively studied before and allows a comparison of the results with those obtained previously. The complex bandstructure of Fe will be shown to give an example of a magnetic system.

Figure 7.3 shows the complex bandstructure of free electrons. This has been obtained using the T -matrix of region II with a constant potential. Because of the finite thickness d of the region which directly enters in the calculation of the k_z component of the complex \vec{k} -vector

$$k_z = \frac{\log \lambda}{i d} \quad (7.1)$$

from the eigenvalues λ of the T -matrix and because of the choice of a single sheet of the complex log-function one obtains a one-dimensional Brillouin-zone with the bands folded into it. We will first focus on the right panel of Fig. 7.3a) showing the black dots. These dots denote the well known free electron Bloch-band with $\Im k_z = 0$. As $\vec{k}_{\parallel} = 0$ has been chosen, this band starts at energy $\epsilon = 0$ and forms the open parabola given by $\epsilon = \frac{1}{2}k_z^2$. Additionally, the left panel of 7.3a) shows parabolas with negative curvature which represent evanescent states with $\Re k_z = 0$. Fig. 7.3b) illustrates how the two panels shown in Fig. 7.3a) can be thought of as two planes in the perpendicular to the complex k_z plane. In this simple plot one can already see several important general properties of the complex bandstructure. The bands are always continuous and do not start or end. As one can show analytically [Hei64], it is a general feature, that at all points where the bands have zero slope, i.e. at points where the band is parabolic in k_z around a minimum or a maximum, one finds another band crossing at right angle in \vec{k} , for example at extrema of the real bandstructure a band with the same $\Re \vec{k}$ but varying $\Im \vec{k}$ is also found. The simplest example for this can be found at $\epsilon = 0$ and $k_z = 0$ in the bandstructure of the free electrons. Furthermore the bands crossing at right angle can be shown to have opposite curvature as also seen in the case of free electrons. The second interesting aspect in Fig. 7.3a) is the appearance of not only one but of several bands denoting evanescent states. This is due to the fact that the system is assumed to have a two-dimensional unit-cell and that therefore a two-dimensional basis set of \vec{g}_{\parallel} vectors was used. Of course, in the free electron case these different \vec{g}_{\parallel} vectors could also be labeled \vec{k}_{\parallel} vectors and these other bands correspond to parabolas defined by $\epsilon = \frac{1}{2}k_z^2 + \frac{1}{2}|\vec{k}_{\parallel}|^2$.

More complicated structures than the complex bandstructure of free electrons can of course be discussed in the case of realistic metals.

Figure 7.4 shows the complex bandstructure of Cu in the [001] direction. The \vec{k}_{\parallel} vector has been chosen to be $(0.5, 0.5) 2\pi/a_{\text{Cu}}$ ($a_{\text{Cu}} = 3.61 \text{ \AA}$). The energy scale was chosen relative to the Fermi level e_F . Again, Fig. 7.4 shows both Bloch states and evanescent states. However, here the representation must be more involved. Bloch states with $\Im k_z = 0$ are again plotted in the central panel as black dots. Different from the case of free electrons, now two panels showing $\Im k_z$ of evanescent bands

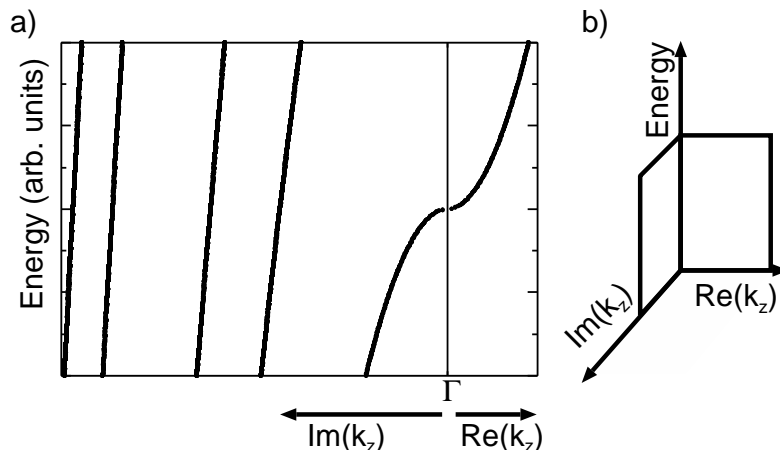


Figure 7.3: Complex bandstructure of free electrons. The left plot (a) shows the complex bandstructure for $\Re(k_z) = 0$ (evanescent states) on the left and for $\Im(k_z) = 0$ (Bloch states) on the right. The corresponding planes in a three-dimensional plot of the energy over the complex k_z planes are indicated in part (b) of the figure.

(complex bands) are added. As both boundaries (X and W) of the Brillouin-zone the bands in the real part of the complex bandstructure have zero slope, at these points complex bands leave the real axis at right angle, i.e. complex bands with $\Re k_z = 0$ or $\Re k_z = 0.25 \times 2\pi/a_{\text{Cu}}$. The imaginary part of these complex bands are indicated by red and green dots in the right and left panel of Fig. 7.4 in units of $a.u.^{-1}$. The bands in the left panel leave the real k_z -axis at the X-point, i.e. they have $\Re k_z = 0$, while those in the right panel have $\Re k_z = 0.25 \times 2\pi/a_{\text{Cu}}$ corresponding to the W-point. In principle two different kinds of complex bands can be identified. These bands might either form open parabolas like in the free electron case where for $\epsilon \rightarrow -\infty$ also $\Im k_z \rightarrow \infty$, or loops are formed connecting maxima and minima of other bands. As the complex bands in Fig. 7.4 have further maxima and minima not lying on the $\Im k_z = 0$ plane other general complex bands exist in Fig. 7.4. For these bands two dots are plotted corresponding to a projection of k_z onto the real and the imaginary plane. The real component of k_z is plotted in the central panel and the imaginary component is shown in the left panel. For example such general complex bands leave the extrema of the complex bands in the left panel and connect them with the small ring in the right panel. Due to the finite energy mesh very flat bands are hard to obtain as can be seen for the band crossing the real bands at ~ -2.3 eV as indicated by the dashed line. When comparing the complex bandstructure with the results obtained in [KS95, Wac86] one finds good agreement. All features of the complex bands in the $\Im k_z$ range plotted here can easily be found in these previous calculations. However, a closer inspection reveals

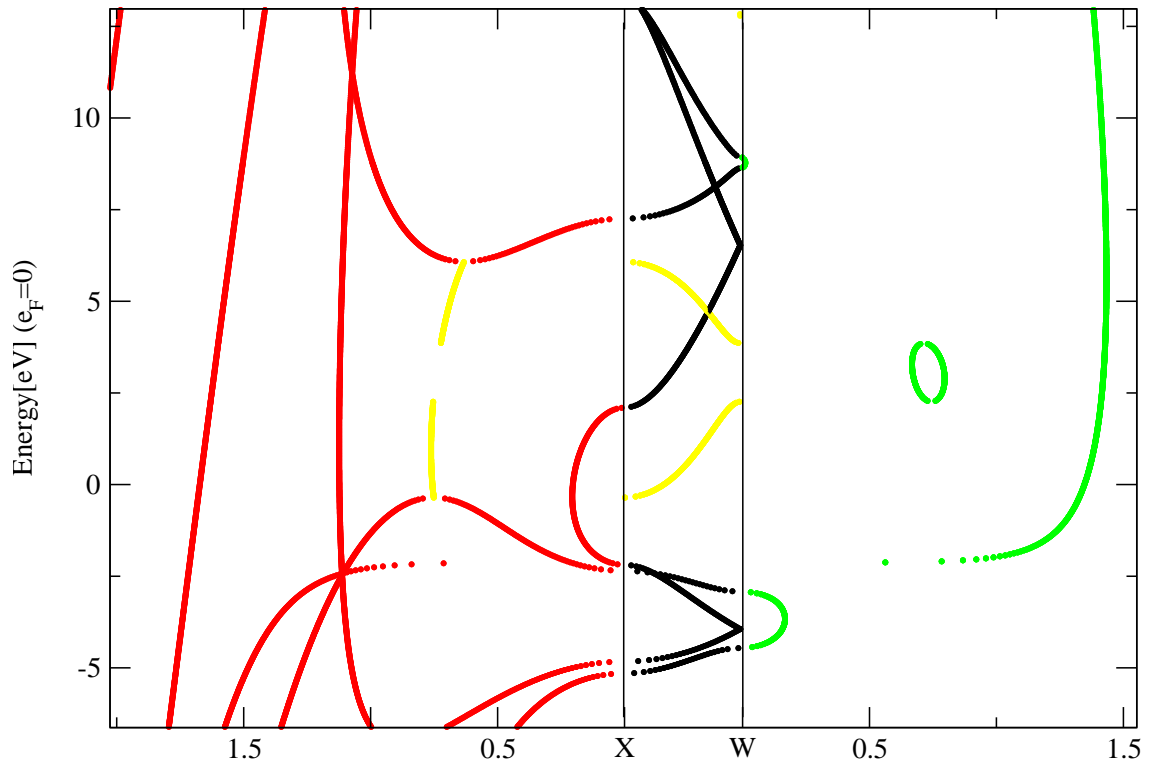


Figure 7.4: Complex bandstructure of Cu. The parallel component of \vec{k} was chosen to be at the \bar{M} -point of the two-dimensional Brillouin-zone. The left panel shows states with $\Re k_z = 0$, the center with $\Im k_z = 0$ and the right panel states with $a_{\text{Cu}} \Re k_z = \pi/2$. The imaginary part of k_z is given in units of $a.u.^{-1} = 1.89 \text{\AA}^{-1}$. See text for more details.

some differences in the complex part of the bandstructure. In particular differences can be found for the band described above having very small dispersion at ~ -2.3 eV. In Ref. [KS95] this band has a minimum in the left panel while in the present calculation as in the one of Wachutka [Wac86] one only finds a very flat band up to $\Im k_z \sim 1.2 a.u.^{-1}$. Another difference can be found for the same band in the left panel. While in both Ref. [Wac86] and this calculation three bands do intersect at $\Im k_z \sim 1.2 a.u.^{-1}$, this accidental degeneracy is not observed in the results of Krasovskii and Schattke [KS95]. As stated by these authors this differences might be due to the overestimation of the dispersion of the flat band by their **kp**-method.

As a third example the complex bandstructure of Fe in the [001] direction is presented in Fig. 7.5. In this case $\vec{k}_{\parallel} = 0$ has been chosen. As Fe is a ferromagnet, the two spins are no longer degenerate and both a complex bandstructure for the majority and the minority spin are displayed. Comparing the two spins one finds the main difference in an energy shift of some bands. The relatively flat real bands

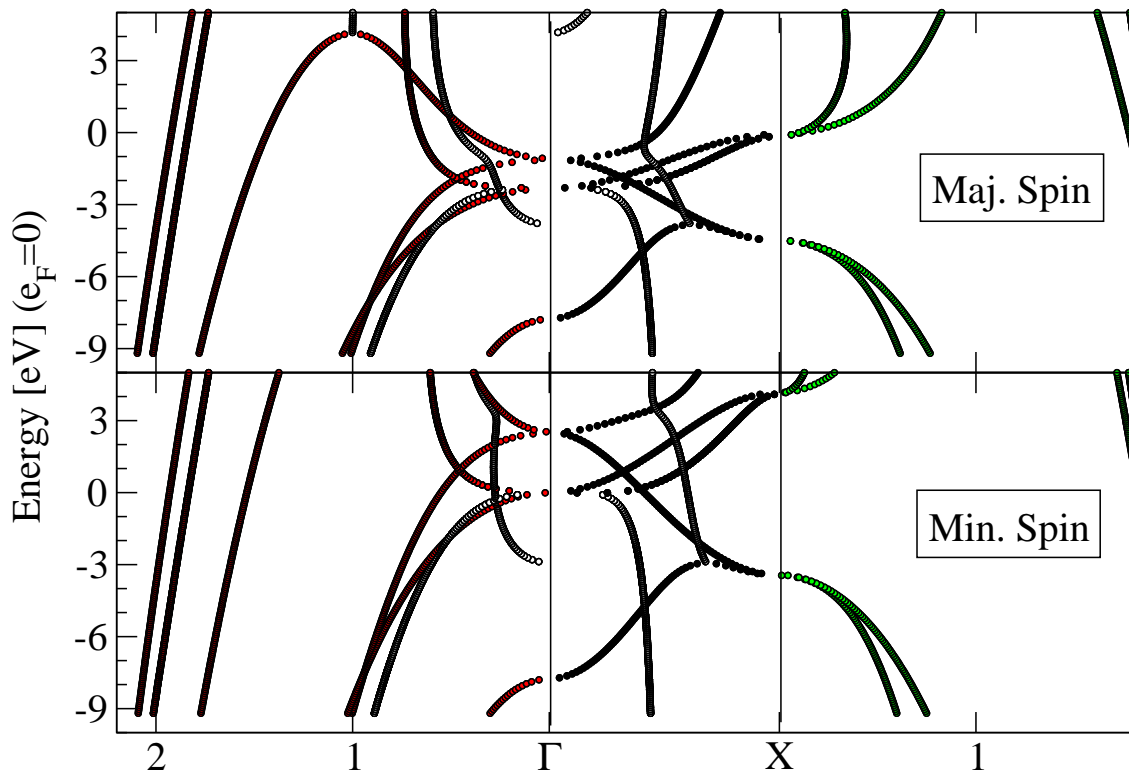


Figure 7.5: Spin dependent complex bandstructure of bcc Fe. \vec{k}_{\parallel} was chosen to be at the $\bar{\Gamma}$ -point of the two-dimensional Brillouin-zone.

in the energy range between -3 eV and 0 eV in the case of the majority spin are shifted to higher energy in the minority spin. These states are occupied by the 3d electrons of Fe and the corresponding energy splitting is the well known magnetic exchange splitting. Except for this effect no large difference between the majority and minority complex bandstructure can be spotted.

Before closing this section one further point remains to be mentioned. In (complex) bandstructure plots very often degeneracy of bands at high-symmetry \vec{k} -points can be expected. Many examples for this can already be seen in the plots shown so far. However, if one inspects for example Fig. 7.5 very carefully, one will notice, that this degeneracy is broken. For example the two majority Bloch bands do not coincide exactly at the X-point at e_F but instead a band crossing can be seen before that \vec{k} -point. This loss of symmetry can have two different origins. Sometimes, if the potential is actually taken from a supercell calculation and not from a separate bulk calculation, the potential used might very slightly deviate from the perfect periodic bulk potential and therefore breaks the symmetry. However, in the (complex) bandstructures shown so far, this can not be the case as the potential is taken from a bulk calculation. Additionally, the computational approach itself in some way

breaks the symmetry. While all two-dimensional (parallel to the interface) symmetry operations are included exactly in the setup of the Hamiltonian by construction, the symmetry operations acting also on the z -component are treated purely numerically. Since the basis is constructed differently perpendicular and parallel to the interface no perfect degeneracy can be expected at the high symmetry points any more.

7.3 Basis set in CBS calculations

When calculating the complex bandstructure some attention has to be applied to the choice of the basis set. As the T -matrix is calculated from the two-dimensional projected Green functions the accuracy of these quantities is of uttermost importance. The projection of the three-dimensional Green function onto the boundary surfaces requires the summation over the z -dependent part of the basis function. For the larger parallel \vec{g}_{\parallel} -vectors this projection can not be performed if the \vec{g} values are taken from the standard sphere $\{\vec{g} \mid |\vec{g} + \vec{k}| \leq g_{3D}^{max}\}$, as for $|\vec{g}_{\parallel}| \sim g_{3D}^{max}$ one would only obtain few (or even only a single) g_z -value and hence the projection could not be reliable.

Fig. 7.6 shows the complex bandstructure of Al. In this example such a basis set leads to the appearance of wrong eigenvalues of the T -matrix. As the boundary vectors of the Bloch states and the very slowly decaying evanescent states can be described by the small \vec{g}_{\parallel} -vectors, these bands can still be identified in Fig. 7.6. However, the strongly decaying solutions with large \vec{g}_{\parallel} -vectors are described incorrectly and some of these solutions even appear as additional unphysical Bloch states.

To ensure a sufficient accuracy of the two-dimensional surface Green functions $G_{bb'}$, the basis functions must be chosen such that the \vec{g} are taken from within a cylinder $\{\vec{g} \mid |\vec{g}_{\parallel} + \vec{k}_{\parallel}| \leq g_{\parallel}^{max}, g_z = \frac{2\pi}{D}n\}$ and not from the sphere. This leads to the inclusion of some unusually high \vec{g} vectors in the plane-wave basis set, which requires additional attention. The basis functions with high \vec{g} vectors add contributions to the Hamiltonian matrix with high kinetic energy. For a proper description these contributions have to be included from the muffin-tin spheres as well. Two different methods have been tested to accomplish this. The first was the use of a modification of the basis as discussed by Soler and Williams [SW89]. In their approach one basically changes the construction of the LAPW basis functions in the following way. First, the plane-waves are used in all space. In the muffin-tin spheres, one then subtracts the plane-wave component again and adds the usual LAPW basis functions. This

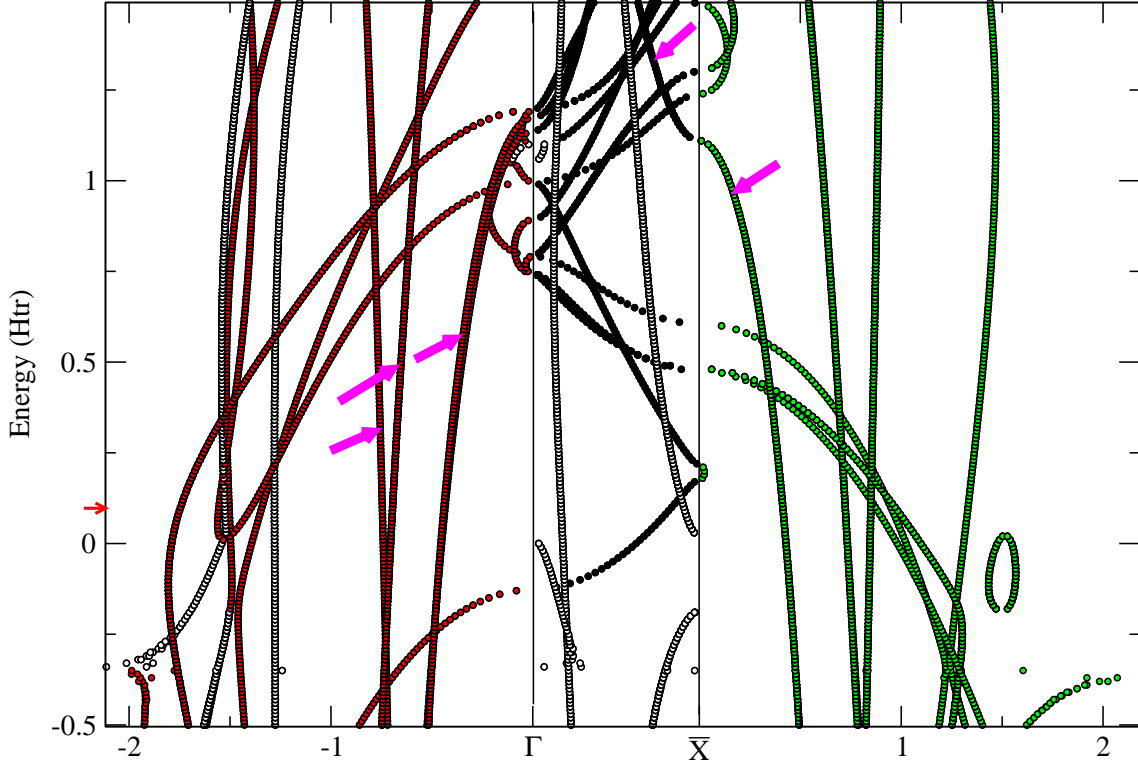


Figure 7.6: Complex Bandstructure of Al in the (001)-direction at $\vec{k}_{\parallel} = 0$ using the sphere construction of the basis set. Additional unphysical bands are marked by arrows.

subtraction is done by using the expansion of the plane-waves into products of radial Bessel functions and spherical harmonics. It is incomplete because the same finite l_{max} cutoff as for the radial LAPW basis is used. Hence, for basis functions with a large \vec{g} -vector a considerable contribution of the plane-waves to the basis functions in the muffin-tin spheres remains, which describes the free electron character of the basis. As demonstrated by Fig. 7.7 this modification can drastically improve the results, however, it proved to be computationally more demanding than the following approach.

In the second approach one simply improves the description inside the muffin-tins spheres by increasing the angular momentum l_{max} cutoff of the spherical harmonics expansion. It turned out that values of $l_{max} \sim 20 - 30$ have to be used. However, as the basis functions with high \vec{g} describe nearly free electrons, the higher l_{max} cutoff is only necessary in the calculation of the matrix elements of the kinetic energy of the Hamiltonian and the overlap matrix. Since these parts are diagonal in l (and spherically symmetric) no significant additional computing time is consumed due to these high cutoffs. Fig. 7.8 shows that in fact the most important improvement is

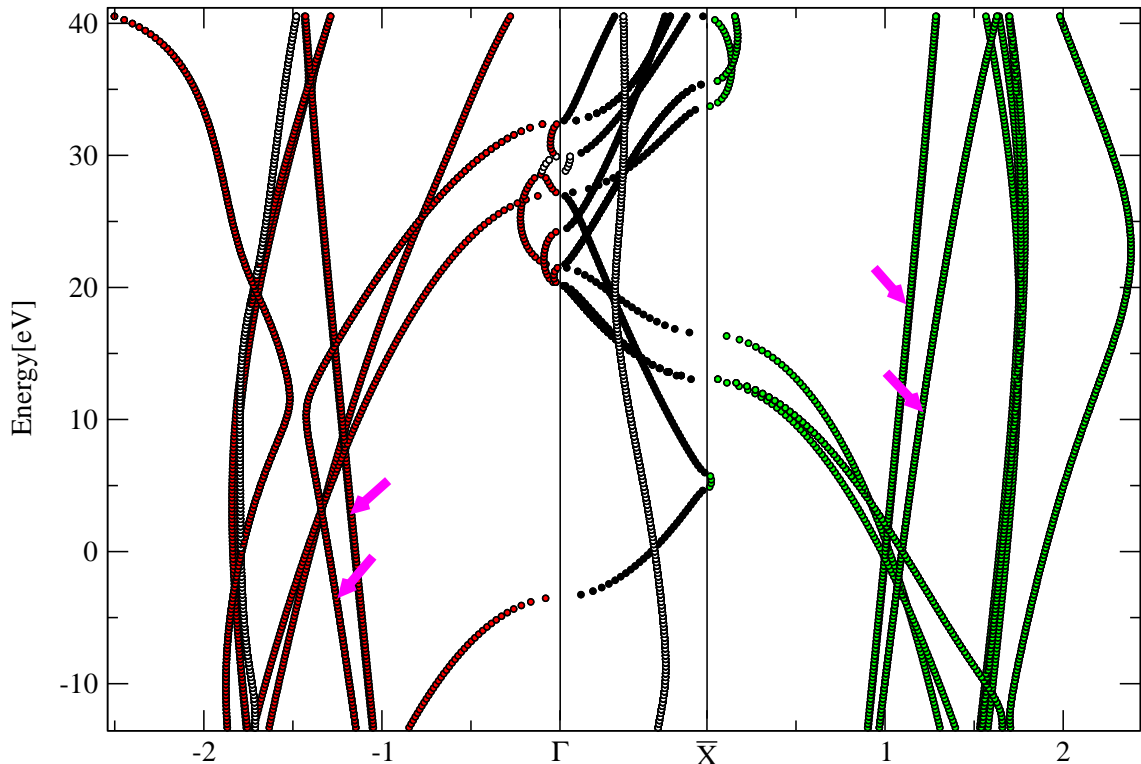


Figure 7.7: Complex bandstructure of Al (see also Fig. 7.6). The ill-converged states (arrows) are shifted to have large $\Im k_z$ by the use of the Soler-Williams modification of the basis.

made by the better description of the kinetic energy in the Hamiltonian. While the increase of the l_{max} cutoff for the calculation of the overlap matrix alone (Fig. 7.8a)) does not improve the results, the use of the higher l_{max} cutoff for the Hamiltonian only (Fig. 7.8b)) already removes the unphysical Bloch states and gives a stable complex bandstructure for the slowly decaying evanescent states. Fig. 7.8c) shows the result with the same large $l_{max} = 30$ cutoff for both S and H . This approach will be used in all further calculations involving the T-matrix.

One should note that the switch from the sphere to the cylinder in the construction of the \vec{g} -vectors leads to a much larger basis set. However, this large basis set does not always have to be used in the Green function calculations. The calculation of the T-matrix depends only on projections of the Green functions of which some have to be inverted. This requires high accuracy. On the other hand, when calculating the charge density from the bulk Green function no projection is performed and the \vec{g} vectors of the basis can be chosen from the standard sphere. The application of the conductance formulas are somewhat in between these two cases. While one also has to project the Green function of the interface region onto the surfaces to apply these formulas, in some cases no cylindrical setup of \vec{g} vectors is needed if the

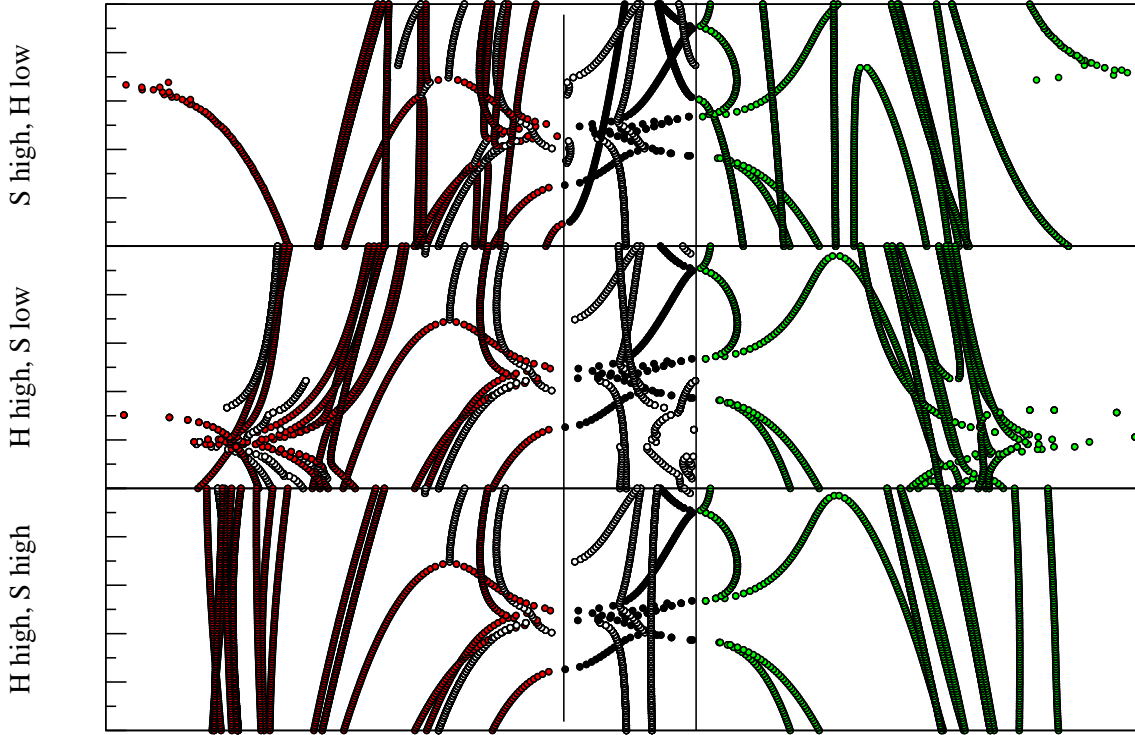


Figure 7.8: Complex bandstructure of Fe, majority spin only. The results in the three panels have been obtained with different l_{max} cutoffs for the S and H matrices. In the upper panel (a), the cutoff for S was chosen to be $l_{max} = 30$ (high) and for H to be $l_{max} = 9$ (low). In the central panel (b), this was reversed and the lower panel (c) both S and H were obtained with the high cutoff.

multiplication with the embedding potential selects only well converged elements of this projected Green function. This frequently occurs in the case of one electrode being a vacuum barrier like in field emission calculations [Ish].

7.4 Transmission from the Green Function

In general the formalisms for the calculation of the electronic transport presented in this work allows to calculate the conductance $\Gamma(\vec{k}_{\parallel}; \epsilon)$ for each energy ϵ and each vector \vec{k}_{\parallel} from the two-dimensional Brillouin-zone for arbitrary numbers of incoming Bloch waves. However, if at most one single incoming Bloch state propagates toward the interface the absolute values of reflection and transmission coefficients $|r(\vec{k}_{\parallel}; \epsilon)|$ and $|t(\vec{k}_{\parallel}; \epsilon)|$ for this state and the conductance we obtain from Eq. (5.42) are related by

$$|r(\vec{k}_{\parallel}; \epsilon)| = \sqrt{1 - 2\pi \Gamma(\vec{k}_{\parallel}; \epsilon)}. \quad (7.2)$$

$$|t(\vec{k}_{\parallel}; \epsilon)| = \sqrt{2\pi \Gamma(\vec{k}_{\parallel}; \epsilon)} \quad (7.3)$$

Very similar in the case of many incoming Bloch states one can view $\Gamma(\vec{k}_{\parallel}; \epsilon)$ as a transmission probability summed over all these states. In such a context the following plots showing the transmission coefficient, the reflection coefficient or the conductance over some energy range for some selected \vec{k}_{\parallel} should be understood. While these are not directly related to the conductance of the system at some finite bias voltage, they can be interpreted as linked to the transmission probabilities of states of different energy, which might become significant for the conductance in a very basic approximation in which one simply shifts the Fermi level without taking any further effect of an applied bias voltage into account.

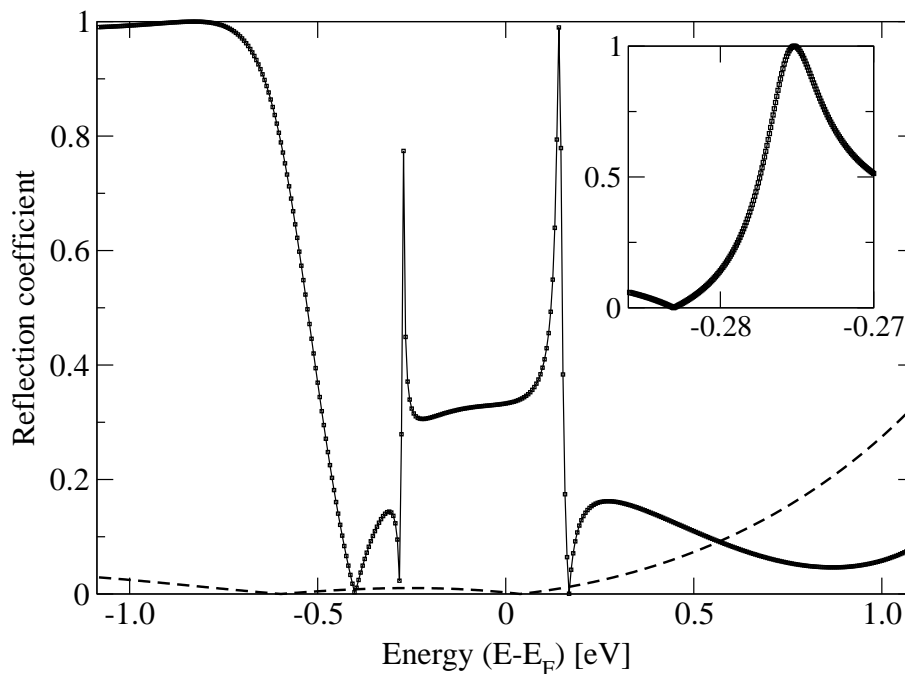


Figure 7.9: Spin-resolved reflection coefficient for a ferromagnetic Cu/5 ML Co/Cu(001) layer for $\vec{k}_{\parallel} = 0$. The zero of energy was chosen to be the Fermi level. Note that the resonance peaks actually reach a value of one as shown in the inset. The difference between two energy grid points was 5.5 meV (inset: 0.08 meV).

Figure 7.9 depicts the spin-resolved reflection coefficients for Cu electrons scattered by 5 monolayers of ferromagnetic Co determined by this equation. The dashed line corresponds to the majority spin channel while results for the minority spin are shown by the squares connected by solid lines. Only states with normal incidence ($\vec{k}_{\parallel} = 0$), i.e. states from the $\bar{\Gamma}$ point of the 2D-Brillouin-zone have been considered. In the majority spin channel the reflectivity of the Co layers is low and varies smoothly over a wide energy range. To interpret the features in this plot the bulk

bandstructure of Cu and Co in the [100] direction, i.e. along the line from the Γ to the X -point, can be used as shown in Fig. 7.10.

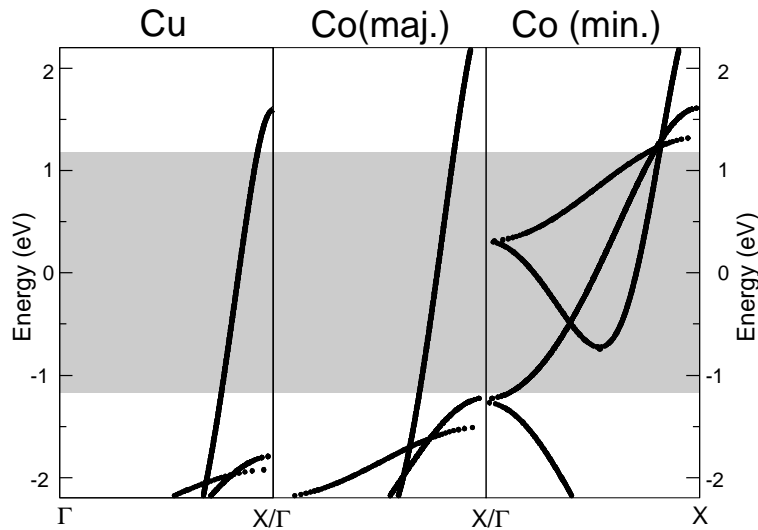


Figure 7.10: Bandstructures of bulk Cu and Co in the [100] direction. This plot was produced by using the Bloch states of the corresponding complex bandstructure plots to overcome the limitation of the FLEUR code which requires a two atom unit-cell for fcc bulk. The left panel shows the Cu band, the middle and right panel the majority and minority Co bands. The energy range used in Fig. 7.9 is shaded.

First, one can see that indeed only a single Cu band contributes to the conductance in the energy range investigated and that therefore the application of Eq. (7.2) is justified. This single band of mostly s -character can be classified according to the two-dimensional symmetry to be a Δ_1 -band [Bur63]. Since the majority Co bandstructure as shown in Fig. 7.10 shows a very similar band of the same symmetry classification the nearly perfect transmission of the majority electrons through the multilayer can be easily understood. Obviously the Cu wavefunctions also form a reasonable good solution for the majority Co electrons and hence no scattering takes place.

The situation is very different in the minority spin case. The bulk bandstructure of Co shows three different bands for the energy range in question. The first, starting at the Γ point at about -1.2 eV with positive slope and the second band starting at the gamma point at 0.4 eV with positive slope belong to a different representation of the two-dimensional symmetry group of the multilayer and therefore can not couple to the Δ_1 -band of Cu. The third band with the minimum at -0.7 eV is

also a Δ_1 -band. From this the features of the reflectivity for the majority spin in Fig. 7.9 can easily be understood. The nearly perfect reflectivity below -0.7 eV is due to the absence of Co states which can couple to the incoming Cu wavefunction. The most pronounced features in Fig. 7.9, however, are the sharp peaks at around -0.28 eV and 0.15 eV. These are due to Fano resonances in the Co layers [Fan61]. Fano resonances essentially occur in the presence of a localized state interacting with a delocalized continuum of states. In this case the following situation has to be considered: In the energy range between ~ 0.4 eV and the minimum of the band at -0.7 eV two solutions with the same energy and different k_z values exist. Of course both of these states can be superimposed to form two solutions (which then is no longer a Bloch state) of the Schrödinger equation. Since now the Co layer is only a finite 5 monolayers slab, in some cases the two states can be combined to form a localized state within the slab. Basically, this can be viewed as a quantum resonance occurring if the phase of one Bloch wave integrated over 5 monolayers equals the phase of the other Bloch wave. In these cases a Fano resonance is formed with the typical change in the transmission from perfect transmission to total reflection as seen twice in Fig. 7.9.

The same Figure as presented here, has been discussed in the paper of Wildberger et al. [WZD⁺98] and Riedel et al. [WZD⁺98, RZM01]. Comparing the results presented here and previous ones, one can conclude that the results shown here are in good overall agreement with those previously obtained [WZD⁺98, RZM01] for the same Cu/Co/Cu setup using the KKR method. A stringent test of the quality of the results is the verification of the reflectivity behavior at the resonances, which varies strongly from zero, i.e. total transmission, to exactly one, i.e. total reflection. The inset of Fig. 7.9, which shows only a small energy interval around the peak lower in energy but resolved with a high density of energy grid points, confirms that this behavior is reproduced very accurately in the present calculation. The deviation from total transmission or reflection at the peak positions is less than 10^{-2} . This is different to the KKR results. They are obtained by carrying out calculations on the complex energy plane. This introduces a computational broadening of the resonances and simultaneously a reduction of the peak height from the ideal value. Instead, the results in this work are obtained at real energies where the broadening of the peaks can be avoided.

7.5 Landauer conductance versus Bardeen's tunneling

One might wonder what is the difference between the results of the Bardeen formula of tunneling and of the Landauer approach. Of course, as stressed in Sec. 3.4 the results will differ significantly as soon as localized states are present in the vicinity of the barrier region. However, it remains to be clarified what should be expected in the absence of these states. Before the difference between these two transport formulas will be investigated for more realistic systems, it is instructive to look at a very simple model that can be treated analytically.

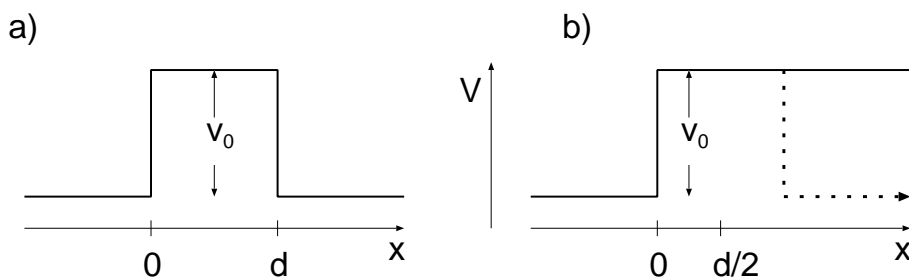


Figure 7.11: a) Setup of a one-dimensional rectangular barrier used for the analytic evaluation of the Landauer equation. b) Corresponding system for the Bardeen formula. The two sides are separated by extending the barrier to infinity. Only the left system of Bardeen's setup is shown, the right is constructed mirrored.

Fig. 7.11 shows the setup chosen for this simple model, a rectangular barrier of height V_0 and width d between leads in which the electrons are described by free electron wavefunctions. In the Landauer picture of transport, the wavefunction is constructed as

$$\psi(x) = \begin{cases} \frac{1}{k} (e^{ikx} + r e^{-ikx}) & x < 0 \text{ in left region} \\ a e^{-\kappa x} + b e^{\kappa x} & 0 < x < d \text{ in barrier} \\ \frac{1}{k} t e^{ikx} & x > d \text{ in right region.} \end{cases} \quad (7.4)$$

The decay constant is given by $\kappa = \sqrt{2V_0 - k^2}$, the coefficients a, b and r, t can be determined by wavefunction matching, i.e. by the requirement that the wavefunction and its derivative are continuous at $x = 0$ and $x = d$. The normalization factor $\frac{1}{k}$ has been chosen such that the Bloch states carry unit current as required. Simple algebra reveals the well known formula

$$t = \frac{4i\kappa k e^{-ikd}}{(ik + \kappa)^2 e^{-\kappa d} + (k + i\kappa)^2 e^{\kappa d}}. \quad (7.5)$$

For wide or heigh barriers, i.e. for large κd , one obtains the well-known dependence

$$\Gamma_{\text{Landauer}} \cong \frac{1}{2\pi} \left| \frac{4\kappa k}{k^2 + \kappa^2} \right|^2 e^{-2\kappa d}. \quad (7.6)$$

If one wants to treat the same system using Bardeen's formula, one has to separate the two systems by extending the barrier to infinity as indicated in Fig. 7.11b. The wavefunctions of the two systems are of course equal except for the transformation $x \leftrightarrow d - x$ and can be written, e.g. for the left side, as

$$\phi_L = \begin{cases} e^{ikx} + \frac{ik+\kappa}{ik-\kappa} e^{-ikx} & x \text{ in leads} \\ \frac{2ik}{ik-\kappa} e^{\kappa x} & x \text{ in barrier.} \end{cases} \quad (7.7)$$

This formula does not depend on the barrier thickness as they describe completely decoupled systems. The conductance in Bardeen's approach is now given by inserting a separation surface at $x = d/2$ and to evaluate the transition probabilities of Eq. (3.23) to obtain

$$\begin{aligned} P_{\text{Bardeen}} &= \frac{\pi}{2} \left| 2 \frac{2ik}{ik-\kappa} e^{-\kappa d/2} \kappa \frac{2ik}{ik-\kappa} e^{-\kappa d/2} \right|^2 \\ &= 2\pi k^2 \left| \frac{4\kappa k}{k^2 + \kappa^2} \right|^2 e^{-2\kappa d}. \end{aligned} \quad (7.8)$$

Comparing Eqs. (7.6) and (7.8) these equations are identical with the exception of the additional prefactor of $4\pi^2 k^2$. This prefactor can be understood from the difference in the deffinition of the two models. While in the case of the Landauer formula an energy integration is performed when subtracting the left and right current, the derivation used for the Bardeen approach one integrates in k-space. Hence, when evaluating the conductance or the current in Bardeen's model as in Eq. (3.24), having in mind that $d\epsilon = k dk$, and that one has to integrate over states at the left and the right system, one obtains the factor k^2 in this transformation. The additional factor of $(2\pi)^2$ is the usual phase-space factor from the two k-integrations. Analogously to this discussion, the difference in the prefactor can also be viewed as a result of the different normalization of the wavefunctions. While in Eq. (7.4) the wavefunctions had to be normalized to carry unit current, in Eq. (7.7) the standard volume based normalization was used. One should stress again that Eq. (7.6) is only valid for the limit of large κd , i.e. for a small conductance. Thus, in the limit of high conductance the formulas differ. This is expected since Bardeen's approach will not be valid in this limit as it does not treat the multiple scattering events correctly

which become important in the case of thin barriers.

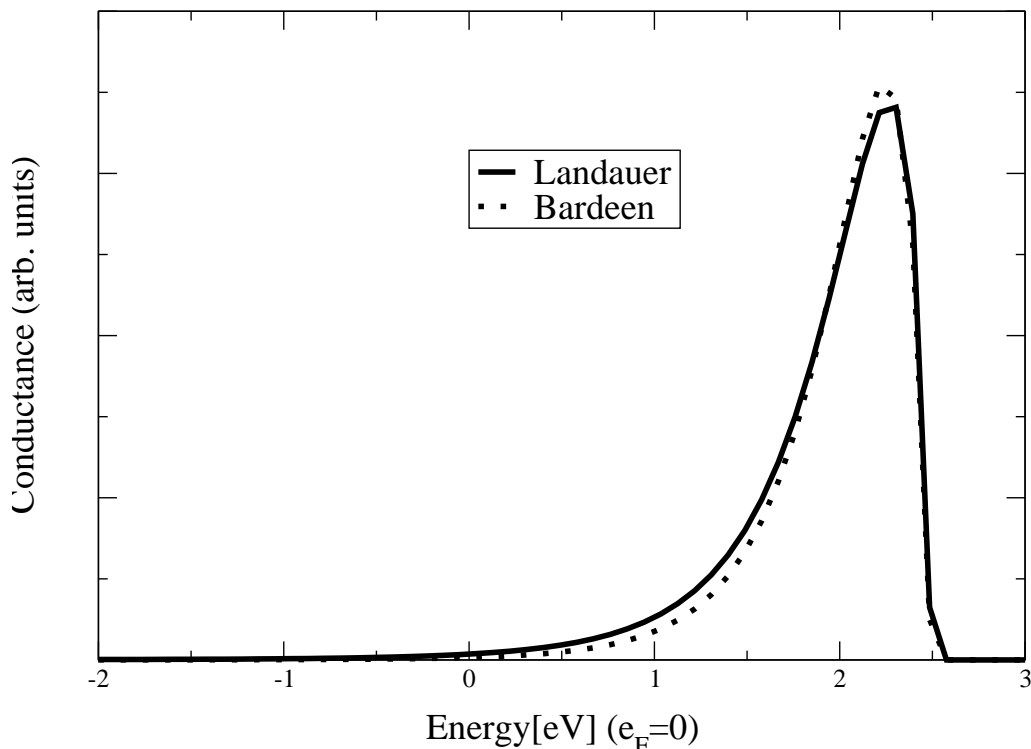


Figure 7.12: Conductance through a vacuum barrier separating two Cu(001) surfaces. Only electrons with normal incidence are considered.

To demonstrate the two formulas for a more realistic, but still simple case a vacuum barrier separating two Cu surfaces will be demonstrated is now being considered. At first a 7.2 \AA vacuum barrier (Cu-Cu distance) between two Cu(001) surfaces is investigated. The ideal surface without any surface relaxation is used and the potential is obtained from a supercell containing five monolayers of Cu. In the calculation of the conductance the uppermost two surface atoms are included in the region defining the barrier. For simplicity only the $\bar{\Gamma}$ -point, i.e. normal incidence of the incoming electrons, is considered. Fig. 7.12 shows the result of both the Landauer and the Bardeen formula for this barrier. As the decay of the Green function into the vacuum is very steep, the different formulas do not agree in the absolute value of the conductance which consequently was adjusted in Fig. 7.12 by using different arbitrary units for the different methods. Even though some further deviations can be seen, the main feature of these curves agree very well indeed. This is due to the fact that in this case both formulas only give small corrections to the most basic tunneling theory, which simply claims the tunneling current being proportional to the local density of states in the barrier. To be more precise, only a single Bloch band with normal incidence $\vec{k}_{\parallel} = 0$ is present in the energy range up to

~ 2.5 eV. Since the vacuum barrier decreases exponentially with increasing energy one expects a strong (exponential) increase of the conductance due to this band up to the point where it vanishes, as seen in Fig. 7.12.

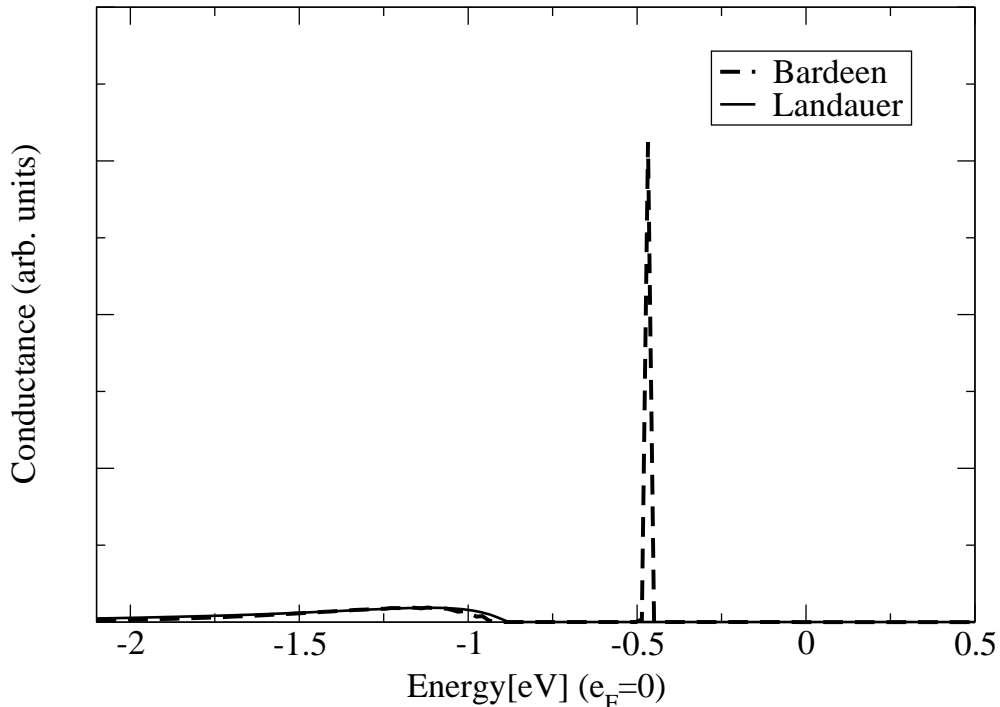


Figure 7.13: Conductance through a vacuum barrier separating two Cu(111) surfaces. The second panel shows the bandstructure of Cu along the [111] direction in the same energy interval.

The situation is very different in the case of the Cu(111) surface as a surface state is formed for this surface orientation. This surface state is very dependent on the surface potential and therefore a thicker slab of 7 monolayer for the bulk supercell calculation and correspondingly a thicker surface buffer layer of 3 monolayers in the conductance calculation has been used. The thickness of the vacuum has also been increased to 8.3 \AA . In this setup one obtains a good agreement of the position of the surface state at ~ 0.4 eV below the Fermi energy with experimental values [WEK⁺01]. Fig. 7.13 shows the result of the Landauer formula as well as the result of Bardeen's approach. As expected, the Landauer formula does not lead to any conductivity in the energy range starting at -0.7 eV since no propagating Bloch states are present. In contrast the result of the Bardeen formula, which agrees pretty well with the Landauer result in the rest of the plot shows an additional huge peak at -0.4 eV in the conductance at the position of the surface state. One should note that the finite broadening of the peak in Fig. 7.13 is due to the introduction of an imaginary contribution to the energy of $\delta = 0.03$ eV. With a real energy grid the peak becomes

extremely narrow and hard to sample. Of course the physical relevant quantity is the area under this peak, i.e. the energy integral.

Chapter 8

The Fe/MgO/Fe Tunneljunction

In this chapter the method developed so far, will be applied to study a realistic tunneljunction. Magnetic tunneljunctions turned to the focus of interest recently, since they became one of the key ingredients in many proposed new devices of magnetoelectronic. The most prominent of those is probably the magnetic random access memory (MRAM). In these MRAM-cells the information is stored in the relative orientation of the magnetization of the two ferromagnetic metallic sides of the junctions and it can be accessed by using the tunnel-magneto resistance (TMR) effect, i.e. the strong dependence of the resistance of the junction on this relative orientation.

In contrast to the widely used but amorphous barrier material Al_2O_3 , MgO allows to grow well-defined tunneljunctions. The Fe/MgO/Fe(100) system represents an ideal candidate for a comparison with a theoretical description. Because of the small lattice mismatch between MgO and Fe, it is possible to grow MgO epitaxially on the Fe substrate [KUB⁺01, WKU⁺01, VDM⁺96]. Thus one might expect the MgO/Fe(100) interfaces obtained experimentally to be very close to the ideal theoretical structure. Unfortunately, while the structure has been prepared and characterized quite successfully, so far little experimental data for electron transport through Fe/MgO/Fe is available. Theoretical studies using the (L)KKR technique [BZSM01, Mat97] have been performed on the Fe/MgO/Fe junction. These studies generally predict a very high degree of spin polarization in the current leading to an optimistic TMR ratio of over 1000%. In 2001 Bowen et al. [BCP⁺01] measured a TMR ration of about 60% for the Fe/MgO/FeCo junction which seem to be at odds with these predictions.

In this chapter I will focus on the influence of the atomic arrangement of the interface formed by MgO on Fe(100) on electronic properties. While the previous theoretical studies already investigated the dependence of the current on the barrier

thickness, I will concentrate on the details of the very interface configuration. My calculations use a MgO barrier of usually 3 monolayers which seems to be the lower end of reasonable values. While experimental junctions are usually thicker, in thick junctions the problem of the structure of the junction becomes even more difficult to deal with. Experimental studies [KUB⁺01] claim that a perfect layer by layer growth can only be archived up to a MgO thickness of about 7 monolayers. Above that, the MgO layers start to relax by forming dislocations. Hence, it might be questionable if the model of coherent transport can be applied to junctions thicker than that. Probably impurities or defects in the barrier become increasingly important and some model of hopping conductance might be more appropriate in the limit of thick barriers.

8.1 Structure

Bulk MgO crystallizes in the rock-salt structure with a lattice constant of 4.21 Å. The surface unit cell of the MgO(001) surface is quadratic with a lattice constant of 2.98 Å with two atoms per unit cell. In this surface both the Mg and the O are placed on simple square grids shifted such that one atom kind is placed in the center of a square of atoms of the other kind. Since the two-dimensional lattice constant of 2.98 Å is close to that of the (001) surface of bcc Fe (2.87 Å) epitaxial growth of MgO on Fe(001) can be expected. The basic structure of the Fe(100)/MgO interface is shown in Fig. 8.1. The MgO layers grow 45° rotated with respect to the Fe layers. The O atom is located on top of the Fe positions, the Mg can be found over the four-fold hollow site of the Fe(100) surface. Different atomic geometries of the MgO/Fe(100) interface were considered. At first an ideal unrelaxed structure is considered. Using ideal bulk positions for all atoms, the most simple structure will be called the unrelaxed Fe/MgO/Fe setup. The two-dimensional lattice constant is determined by the lattice constant of bulk Fe to be $a = 5.42 \text{ a.u.}$. Correspondingly, the interlayer spacing of the Fe layers is $d_{\text{Fe}} = 2.71 \text{ a.u.}$. The interlayer spacing of the MgO was chosen to be $d_{\text{MgO}} = 4.15 \text{ a.u.}$. This is slightly larger than the value one would obtain for bulk MgO to compensate for the smaller two-dimensional lattice constant such that the volume of the three-dimensional unit cell is kept constant. The same spacing was also used for the distance between the interface MgO layer and the interface Fe layer. A schematic, two-dimensional representation of the interface setup is shown in Fig. 8.2.

Starting from the unrelaxed setup force and total energy calculations have been performed to relax the interlayer distance of the interface layers and to allow an in-

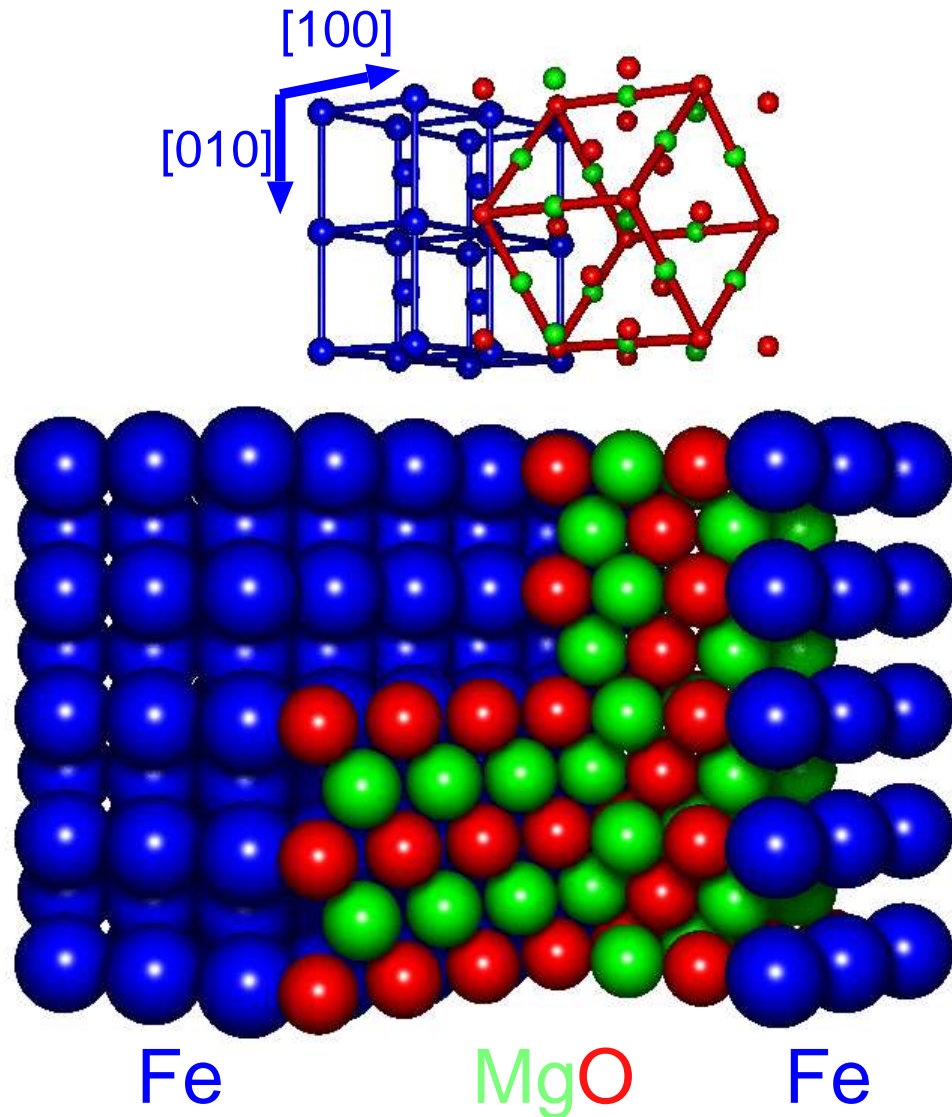


Figure 8.1: Three-dimensional crystal structure of the Fe/MgO interface.

plane relaxation of the interface MgO layer. These calculations have been performed in a supercell containing 7 monolayers of Fe and 3 monolayers of MgO. This supercell mimics a Fe/MgO/Fe junction. The GGA exchange-correlation potential of Perdew and Wang [PCV⁺92] has been used in the relaxation steps, and k-point sampling was done using a set of 90 points in the irreducible wedge of the Brillouin-zone.

Table (8.1) gives the interface relaxations obtained in this procedure. The positions of the O atoms can be considered to be roughly constant and also the Fe-O distance is only slightly modified. The Fe-Fe interlayer distance is slightly reduced near the interface as one would also expect for a free Fe surface. The most pronounced effect can be seen in the corrugation of the interface MgO layer. The reduced coordination

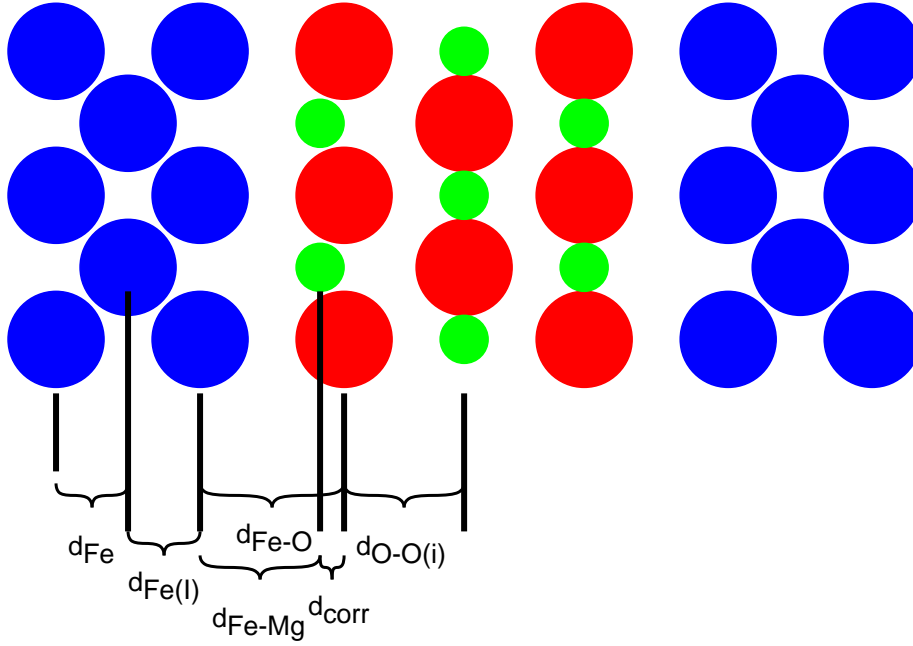


Figure 8.2: Two-dimensional geometry of the Fe/MgO interface

	d_{Fe}	$d_{\text{Fe(I)}}$	$d_{\text{Fe-O}}$	$d_{\text{Fe-Mg}}$	d_{corr}	$d_{\text{O-O(I)}}$	d_{MgO}
ideal	2.71 a.u.	2.71 a.u.	4.15 a.u.	4.15 a.u.	0	4.15 a.u.	4.15 a.u.
relaxed	2.71 a.u.	2.55 a.u.	4.17 a.u.	4.06 a.u.	0.11 a.u.	4.16 a.u.	

Table 8.1: Interface relaxations. A supercell of 7ML Fe and 3ML MgO was used to perform the calculation. The ideal positions were assumed to be given by the bulk values and by using the same Fe-MgO spacing as the bulk MgO-MgO interlayer distance.

of the small Mg ions is compensated by a movement of these ions towards the hollow site of the Fe interface layer. The positions of the interface atoms obtained in the relaxation process have been used for a different setup, in which the number of MgO layers was modified.

	1.layer	2. layer	3. layer	4. layer
(0.0, 0.0)	-	Fe: 3.19 a.u.	O: 7.63 a.u.	Mg: 11.87 a.u.
(0.5 ,0.5)	Fe: 0 a.u.	O: 3.57 a.u.	Mg: 7.63 a.u.	O: 11.87 a.u.

Table 8.2: Atomic positions of the Fe/FeO/MgO interface. The occupancy of the two different positions in the two-dimensional unit-cell for four interface layers are given, starting with the last pure Fe layer. The interlayer distances are given with respect to this last Fe layer. All positions have been chosen according to [MPJ⁺02].

There is some experimental evidence for the formation of an FeO layer at the interface between the Fe and MgO monolayers. The actual atomic arrangement at the

interface in this case is unknown. In Ref. [MPJ⁺02] the authors claim that in the interface Fe-layer about 60% of all hollow side positions are occupied by additional O atoms. Using surface x-ray diffraction the atomic positions have been determined by Meyerheim et al. in that experimental work. To investigate the influence of FeO on the tunnel characteristics an additional setup using positions according to these experimental results has been used. Of course the actual atomic arrangement of the FeO layer at the interface could also be determined by ab-initio calculations. However, since experimental evidence for the formation of the FeO is not conclusive and since such a calculation must also reflect the relaxation of the magnetic properties and the determination of the influence of the coverage of only 60%, this relaxation was not performed in this work. Instead experimental positions have been used. Table 8.2 shows the actual geometry used in the junctions including an FeO layer.

8.2 Electronic Structure

Fig. 8.3 shows the majority (positive) and minority (negative) contribution to the local density of states (LDOS) at different positions for the MgO/Fe interface. The energy range $e_F - 3eV < \epsilon < e_F + 3eV$ in the plots was chosen to include only states near the Fermi energy e_F which are relevant for transport. The LDOS was calculated from the relaxed 7ML Fe/3ML MgO supercell. The uppermost panel displays the Fe-LDOS. To the left the LDOS of the central Fe layer is plotted, to the right the LDOS of the interface Fe is shown. The central layer can be considered as bulk Fe. In both plots arrows at the Fermi level ϵ_F are used to indicate the value of the LDOS in both spins. One can see that for the bulk Fe the LDOS at Fermi level is slightly larger for the majority spin contribution, hence the spin polarization at Fermi level is positive in bulk Fe. The spin polarization at the Fermi level becomes negative at the interface Fe layer. In simple theories of tunneling like the Julliere model [Jul] one assumes that the basic quantity defining the tunneling process is the density of states. Basically in these theories the conductance is determined by the product of the spin-resolved density of states of both sides. Applied on this Fe/MgO/Fe junction one would expect a big contribution from the minority spin states due to their high density of states at the Fermi level.

The two central panels of Fig. 8.3 display the LDOS in the MgO interface layer, the lower two panels the LDOS in the central MgO layer. At the energy range shown here, bulk MgO has a bandgap and therefore the LDOS in these plots are purely due to the decaying LDOS induced by the Fe. This can be seen very clearly in the right panel showing the O LDOS. The LDOS in these plots corresponds nicely to

the Fe LDOS at the interface. Furthermore one can see an exponential decay of this interface Fe LDOS into the MgO. While the LDOS in the interface MgO layer is about a factor of 10 smaller than that of the Fe layer, it decays by another factor of ~ 10 in the center MgO layer.

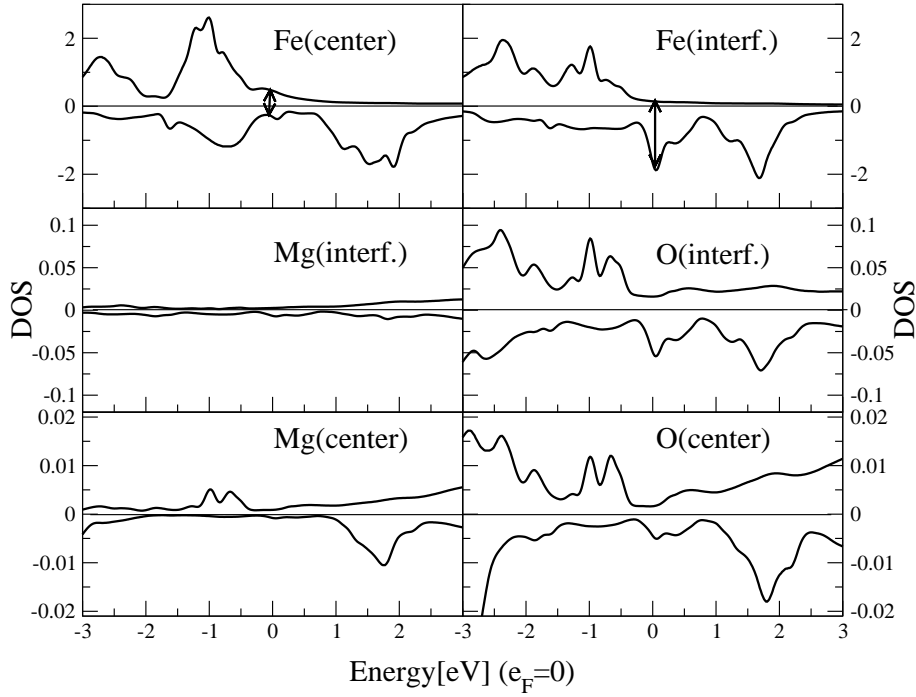


Figure 8.3: Local density of states at different atomic positions of the Fe/MgO/Fe junction

For reference Figs. 8.4 shows the bandstructure of bulk Fe. Only the bands of normal incidence ($\vec{k}_{\parallel} = 0$) are displayed, i.e. the line from Γ to X is plotted. This figure actually shows the subset of Bloch bands of a complex bandstructure calculation as given in Fig. 7.5. However, this time the potential of the supercell calculation has been used to check the convergence of the potential in this setup to the Fe bulk value at the central Fe layer. The overall agreement of the bandstructure plotted in Fig. 8.4 with that of bulk Fe is a very good indicator for a well converged potential. Only the slightly larger splitting of the otherwise degenerated levels at high symmetry points is due to some little difference to bulk Fe.

The complex bandstructure of MgO is shown in Fig. 8.5. The bandgap has a value of about 4.5 eV as typical for LDA calculations and reaches from about -2.5 eV up to 2 eV. The Fermi energy in this system is chosen according to its position in a Fe/MgO junction. At $\vec{k}_{\parallel} = 0$ the highest occupied band of the valence band is connected by a complex band forming a loop with purely imaginary k_z to the lowest unoccupied band. This complex band is the slowest decaying evanescent state within

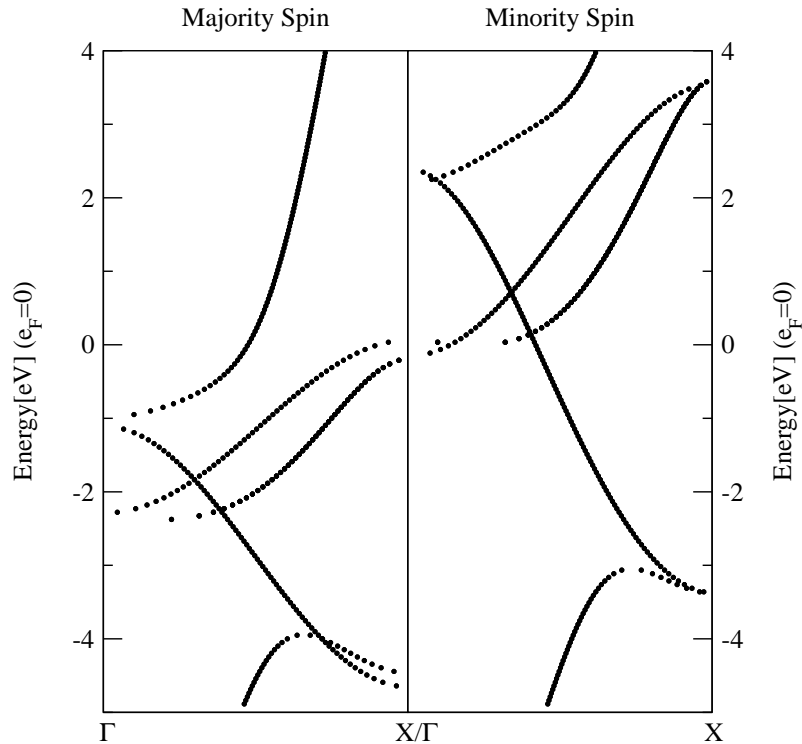


Figure 8.4: Bandstructure of Fe along the Γ -X direction.

the band gap. At Fermi energy the red line shows that this slowest decaying band has a k_z value of $k_z = 0 + i 0.18 a.u.$ leading to an decay proportional to $\exp(-0.18 d)$ where d is the thickness of the barrier in $a.u.$. This is the expected asymptotic decay constant if no interface effects are present, i.e. it is the decay expected in the limit of very thick barriers.

8.3 Ferromagnetic Fe/MgO/Fe junction

The first system to study is the Fe/MgO/Fe junction as described in Sec. 8.1. The direction of the magnetization of both Fe leads is parallel, i.e. the two sides couple ferromagnetically. Hence, the majority spin electrons on the one side correspond to the majority electrons on the other side and the same is true for the minority electrons.

If one first focuses on the electrons with normal incidence ($\vec{k}_{\parallel} = 0$) on the barrier one can try to deduce some information from the bandstructures of these Fe-states as shown in Fig. 8.4. One might assume that the conductance due to the minority electrons should be higher than that due to the majority electrons in the vicinity of the Fermi level since more Bloch states are present in the minority spin. This

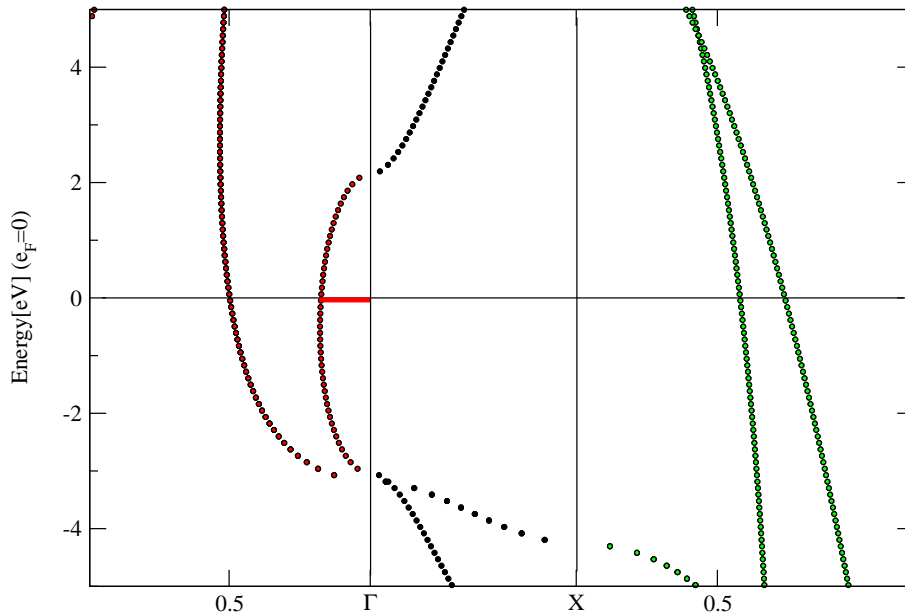


Figure 8.5: Complex bandstructure of MgO.

argument should be applicable especially if one considers the conductance due to states slightly higher than the Fermi level in which only a single Fe band is present in the majority spin while three different bands (of which is one two-fold degenerate) can be seen in the minority spin. However, as it was pointed out by Wunnicke et al. [WMZ⁺02] this simple explanation might fall short to describe the system correctly if not all of the states involved are allowed to couple to the slowly decaying MgO band discussed in the previous section.

In the Landauer picture of ballistic transport a single wavefunction throughout the whole junction is assumed. Since the junction has a two-dimensional symmetry corresponding its square two-dimensional lattice (space-group p4m) these wavefunctions must correspond to some representation of this group. Due to this not all incoming Fe states are allowed to couple to all decaying states within the MgO barrier. This effect can be seen very clearly in Fig. 8.6 showing the conductance through the junction due to states with $\vec{k}_{\parallel} = 0$ and energy close to the Fermi level.

From the arguments presented so far one might be surprised by the results shown in Fig. 8.6. Opposite to the density of states argument presented, the minority spin does not lead to any significant conductance. The majority spin however, shows a clear feature of strong conductance starting at about -0.9 eV below the Fermi energy. Some closer inspection of the bandstructure of Fe and of the complex bands of MgO reveal the origin of this effect. The Fe minority bands present in the energy range discussed here do not couple to the slowest decaying state within the MgO layers.

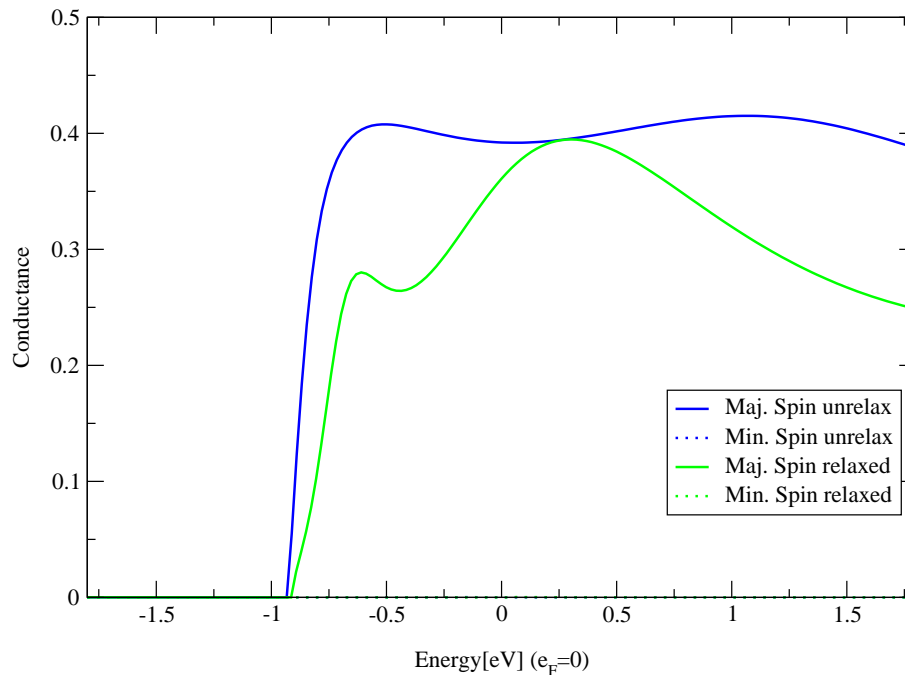


Figure 8.6: Landauer-conductance (in units of $\frac{e^2}{h}$) through a ferromagnetic Fe/MgO/Fe junction with 3 monolayer of MgO. Only electrons with normal incidence are considered. The plot shows both the relaxed and the unrelaxed structure. Only the majority spin channel leads to any significant conductance, the dotted lines corresponding to the minority spin are indistinguishable from the $\Gamma = 0$ line.

The same applies for most bands in the Fe majority spin. The only exception is the Fe majority band starting at about -0.9 eV. This leads to a pronounced increase of the conductance. Interestingly, the relative small difference between the relaxed and the unrelaxed structure leads to a clear variation of the energy dependence of the conductance. This effect however is a pure quantitative one, the basic features of the curves coincide.

Until now only electrons of normal incidence have been considered. While this might be an obvious choice due to the fact that the bandgap in MgO is smallest at the Γ -point, of course the presented symmetry argument only holds for this special high symmetry point. Hence, the conductance should be calculated for all \vec{k}_{\parallel} values within the two-dimensional Brillouin-zone. The two-dimensional Brillouin-zone of the Fe/MgO interface is depicted in Fig. 8.7 including the high symmetry points and the irreducible wedge. Fig. 8.8 shows the conductance through the ferromagnetically aligned barrier plotted over the square two-dimensional Brillouin-zone of the system. In this plot, only states at the Fermi-level have been taken into account, hence the conductance of the junction at zero bias can be obtained from this plot by a simple integration over all two-dimensional \vec{k}_{\parallel} values. The results for both the relaxed and

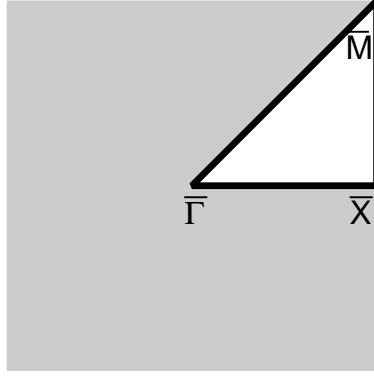


Figure 8.7: Square symbolizing the two-dimensional Brillouin-zone of the setups used for the various junctions in this chapter. The white triangle denotes the irreducible part with three high symmetry points at its corners.

the unrelaxed junction are shown. Qualitatively, one can see little difference between the two structures. The total conductance is clearly dominated by a broad peak in the conductance of the majority spin channel around $\vec{k}_{\parallel} = 0$. As already seen in the plot showing the energy-dependent conductance of this point only, the conductance is very much the same in the relaxed and unrelaxed structure at the $\bar{\Gamma}$ -point. In the minority spin, Fig. 8.8 shows a very low conductance for all different \vec{k}_{\parallel} -points. Its maximum is about two orders of magnitude smaller than that of the majority spin. The maximum of the conductance for this spin is not found for the $\bar{\Gamma}$ point but around the \bar{X} -point. This small conductance in the minority spin at the \bar{X} -point can be confirmed by the energy dependent conductance at this \vec{k}_{\parallel} -point as shown in Fig. 8.9 for the unrelaxed junction setup.

As a further test, the influence of a thicker MgO barrier has been modeled by including two additional layers of MgO into the barrier leading to a total barrier thickness of 5 monolayer. Fig. 8.10 shows the result corresponding to that of Fig. 8.6 for this thicker barrier using the relaxed interface positions. One can see the expected strong decay of the transmission due to the increased barrier thickness. However, the qualitative features of the curve remain largely unaffected with the exception of the relative increase of the conductance at higher energies. This increase can be understood from the fact that the barrier height for these energies decreases strongly due to the onset of the conduction bands of MgO at about 2 eV. For thicker barriers this decrease of the barrier is expected to be even more important in these energy dependent plots.

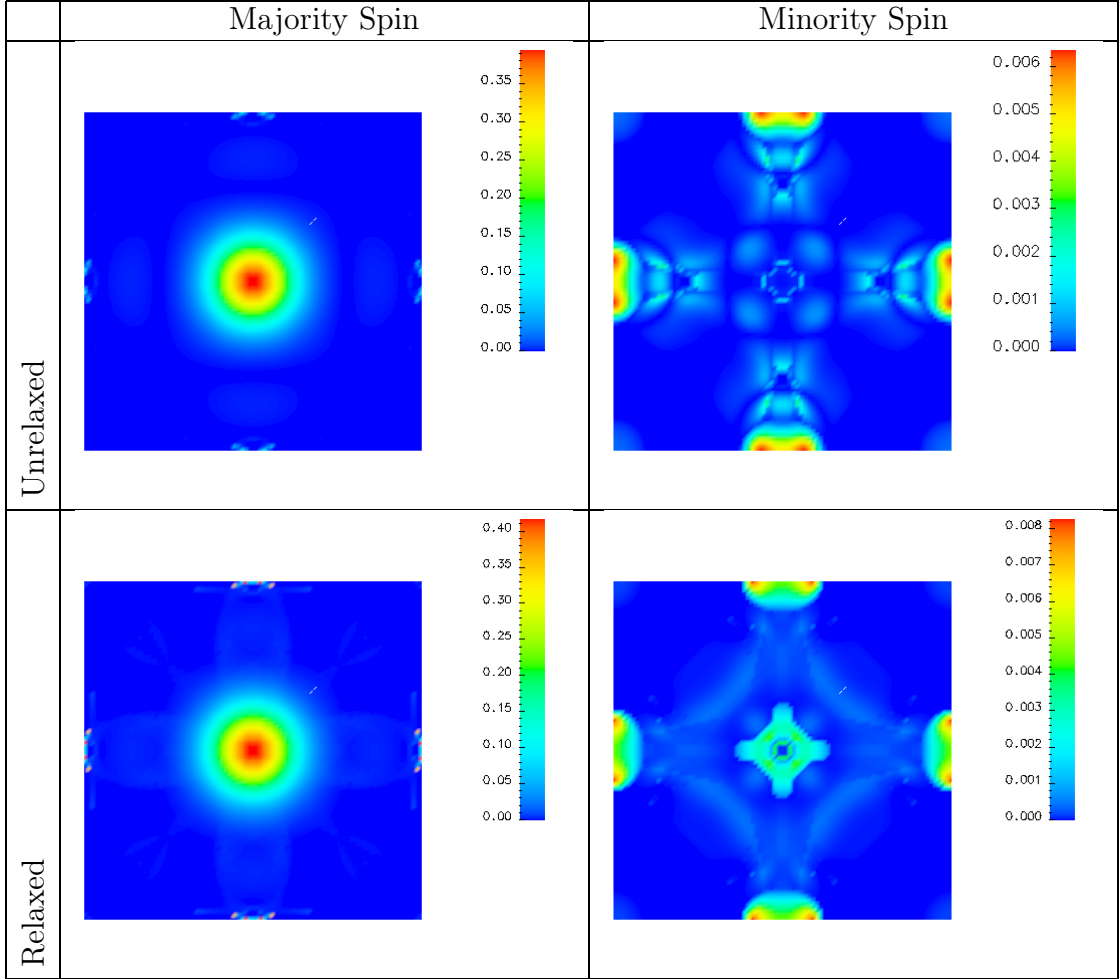


Figure 8.8: \vec{k}_{\parallel} -resolved conductance of the Fe/MgO/Fe junction through a 3 monolayer MgO barrier. Only states at Fermi energy are taken into account. The first row shows the spin-resolved conductance for the unrelaxed junction, the second row for the relaxed junction.

8.4 Bardeen's approach applied to the Fe/MgO

The results presented so far were all obtained using the Landauer formula of conductance. This model might fail to describe the system correctly in two respects. First, in the presence of slowly decaying evanescent states in the MgO, the underlying assumption of Bardeen's approach might not be satisfied. Second, there might be some localized states at the Fe/MgO interface which do contribute to the tunneling but not to the Landauer type of transport as it was discussed in the previous chapter.

To estimate the reliability of the Landauer results with respect to these effects the conductance has been evaluated using Bardeen's approach. Fig. 8.11 shows the resulting conductance. The setup in this system was chosen according to the relaxed

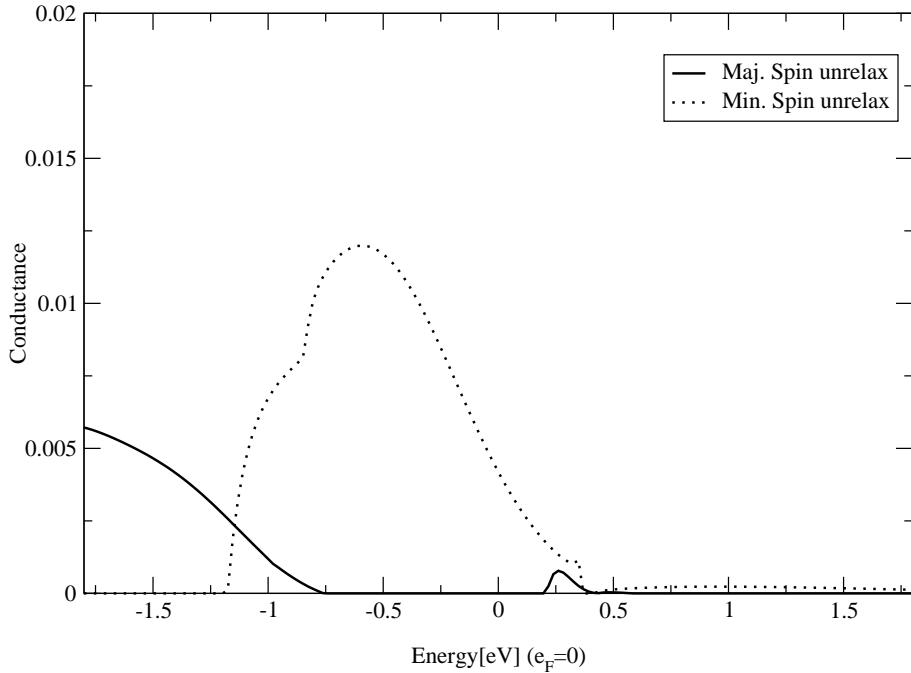


Figure 8.9: Landauer-conductance (in units of $\frac{e^2}{h}$) through an unrelaxed ferromagnetic Fe/MgO/Fe junction with 3 monolayers of MgO. In contrast to Fig. 8.6 the \vec{k}_{\parallel} -vector has been chosen from the \bar{X} -point in this plot.

positions. Three Fe layers and the interface MgO layer have been used in the calculation of the Green function of the Fe/MgO setup. The resulting energy depended conductance for the system is very similar to the result obtained in the Landauer scheme. Obviously, the different processes described by Bardeen's approach do not lead to additional conduction channels in this plot. This finding is confirmed by Fig. 8.12 showing the conductance not only of the $\bar{\Gamma}$ -point but of the whole two-dimensional Brillouin-zone. Compared to Fig. 8.8 little changes can be found. The conductance of the majority spin channel clearly dominates the total conductance due to a broad peak at the $\bar{\Gamma}$ -point, while the conductance of the minority spin channel is at least an order of magnitude lower and mostly due to states near the \bar{X} -point.

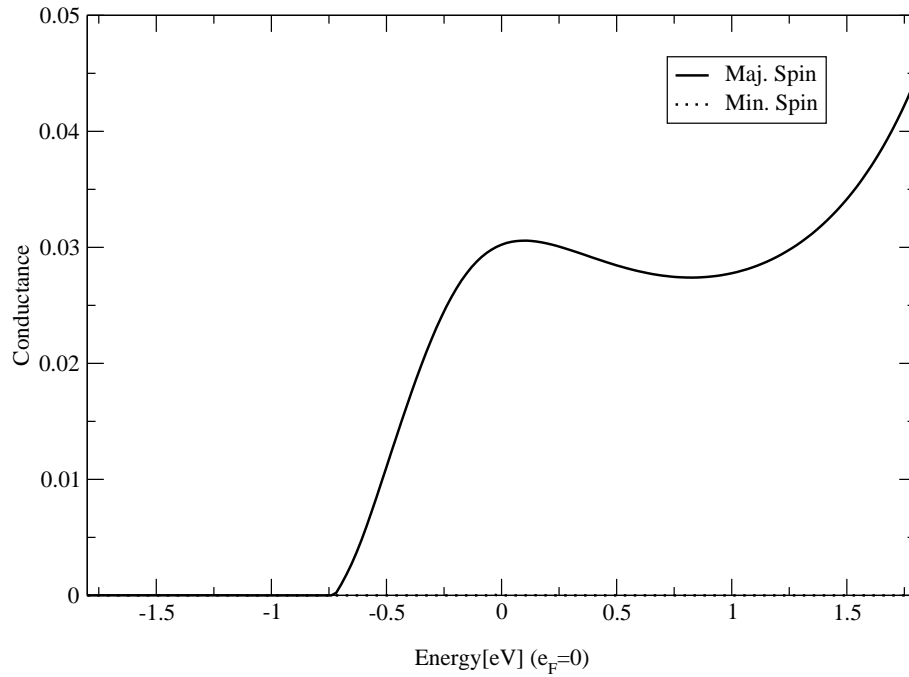


Figure 8.10: Landauer-conductance (in units of $\frac{e^2}{h}$) through a ferromagnetic Fe/MgO/Fe junction with 5 monolayers of MgO. Again, only electrons with normal incidence are considered.

8.5 LDA+U for MgO

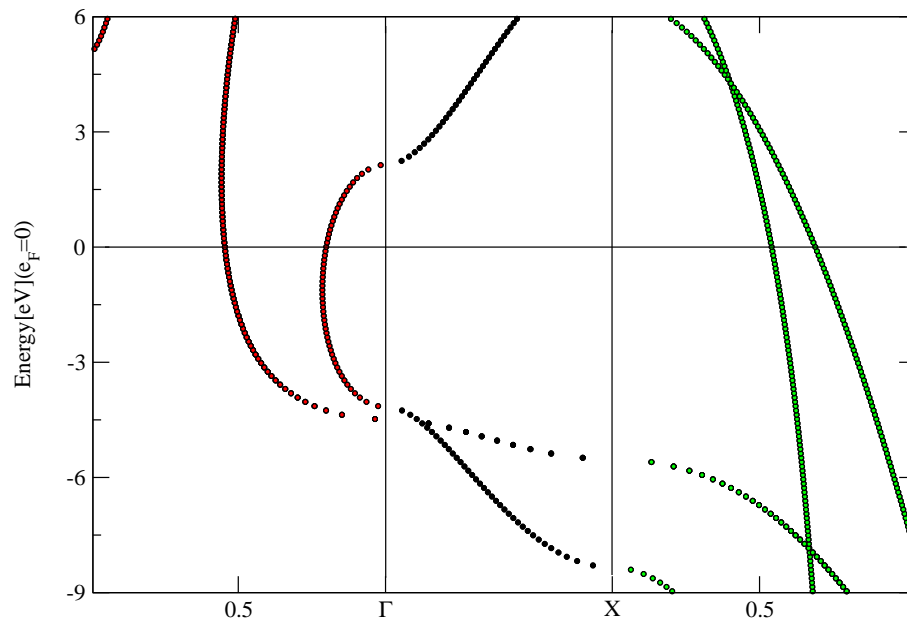


Figure 8.13: Complex bandstructure of MgO using LDA+U to correct the bandgap.

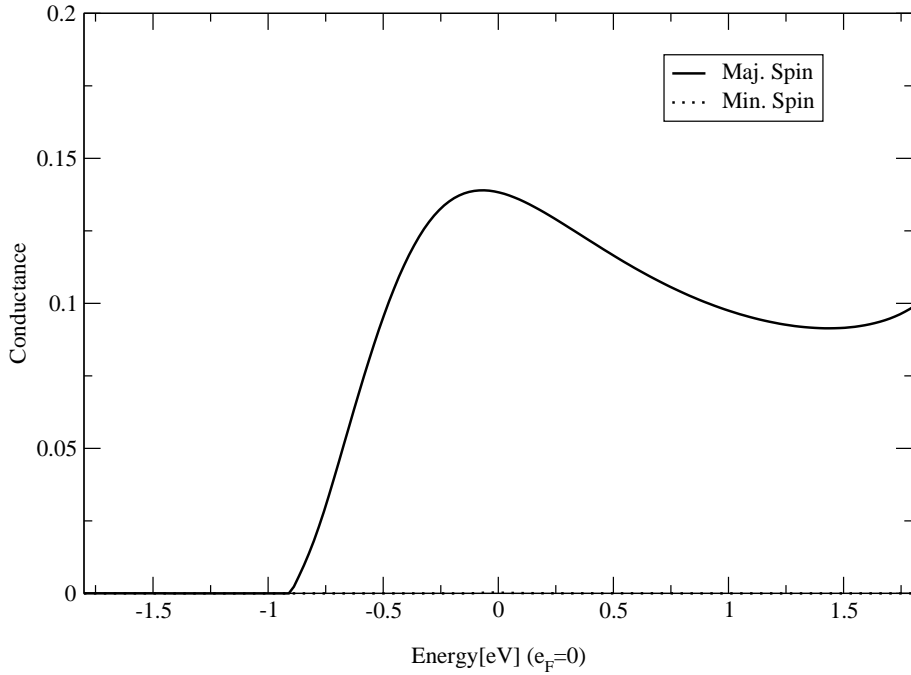


Figure 8.11: Bardeen-conductance through a relaxed ferromagnetic Fe/MgO/Fe junction. Only the $\vec{k}_{\parallel} = 0$ contribution is shown for both spins. Again the minority spin does not lead to any significant conductance.

Until now, the usual generalized gradient approximation (GGA) to the exchange-correlation potential has been used. As demonstrated in Fig. 8.5 this approximation leads to a band gap of ≈ 4.5 eV within the MgO layers. Due to the well known deficiency of the GGA (or LDA) exchange-correlation potential this value is considerably smaller than the experimental value of ≈ 7.8 eV. To investigate the influence of this discrepancy the LDA+U scheme has been applied to correct the band gap in

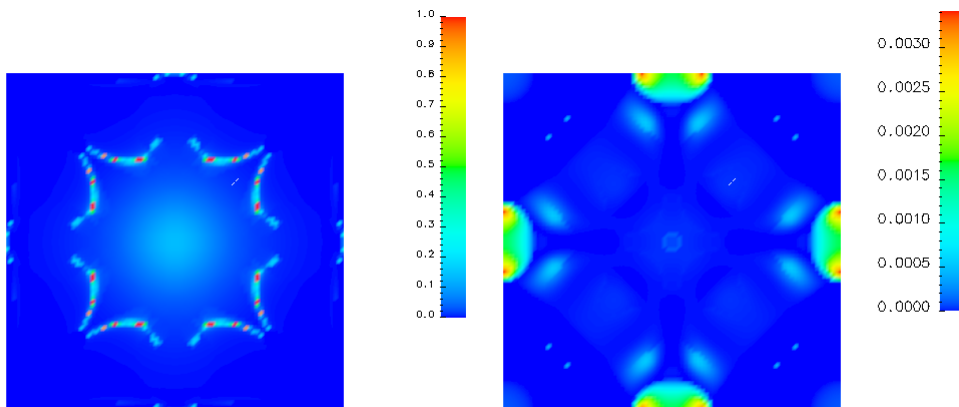


Figure 8.12: \vec{k}_{\parallel} -resolved conductance of the Fe/MgO/Fe junction through a 3 monolayer MgO barrier. In contrast to Fig. 8.8 the conductance is calculated from Bardeen's formula.

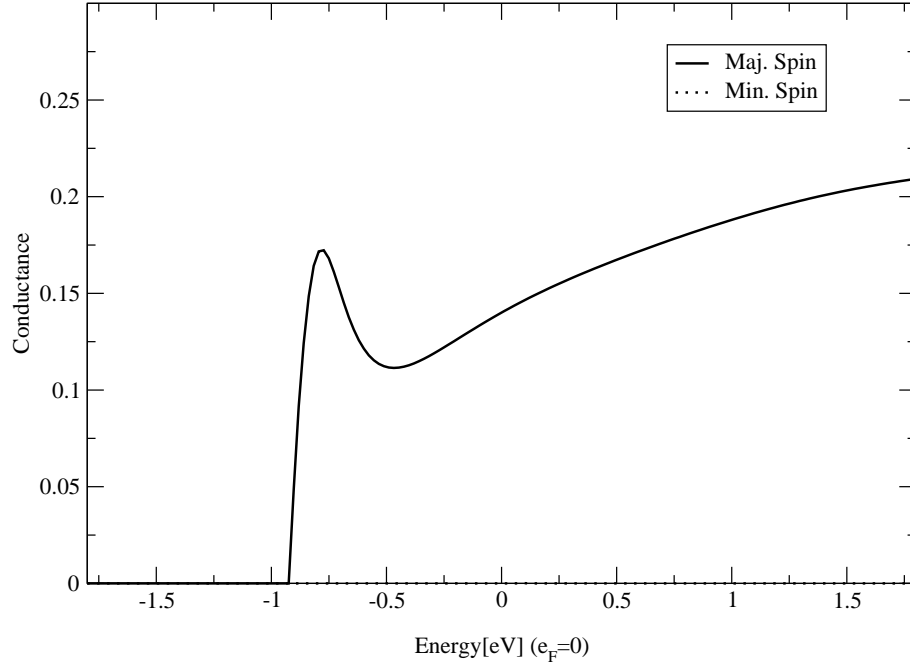


Figure 8.14: Landauer-conductance (in units of $\frac{e^2}{h}$) through an unrelaxed ferromagnetic Fe/MgO/Fe junction with 3 monolayer of MgO. In contrast to the results presented in Fig. 8.6 the LDA+U method has been applied to correct for the band-gap of MgO.

the MgO layers.

Fig. 8.13 shows the complex bandstructure of MgO as obtained with a value of $U=7.8$ eV applied to the p-electrons of the O-atoms in the MgO. When comparing this bandstructure with that of Fig. 8.5 one can easily identify the increased band gap. However, except from this, which can be considered as being caused by a

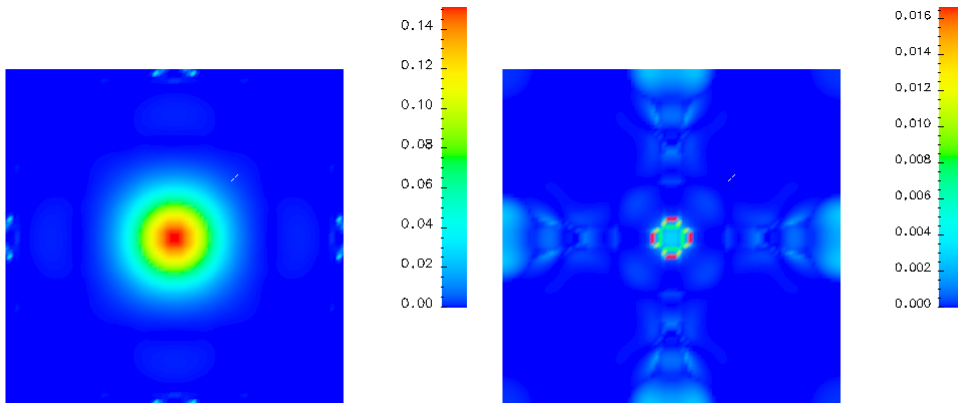


Figure 8.15: \vec{k}_{\parallel} -resolved conductance of the Fe/MgO/Fe junction through a 3 monolayer MgO barrier taking the LDA+U correction of the MgO bandgap into account. As in Fig. 8.8 only states at Fermi energy are taken into account.

shift of the conduction band to higher energies little qualitative changes can be detected. The LDA+U scheme simply acts similar to the well known „scissors-operator“ without introducing new effects into the bandstructure in this case.

Correspondingly, the effect of the change of the MgO bandgap on the conductance is also a pure quantitative one. Fig. 8.14 shows the conductance of the unrelaxed Fe/MgO/Fe setup with the LDA+U applied. A direct comparison of this plot with that of Fig. 8.6 shows no new structures, only the absolute value of the conductance is reduced by about 50%. This reduction should be expected due to the larger energy barrier the electrons have to overcome. From the complex bandstructure of the MgO with and without LDA+U applied (Figs. 8.13 and 8.5) one can extract the values of the imaginary part of the k_z value for the slowest decaying band at the Fermi energy at $\vec{k}_{\parallel} = 0$. These are given by $\kappa_{\text{LDA}} = 0.18$ and $\kappa_{\text{LDA+U}} = 0.21$ in atomic units. From the decay proportional to $\exp(-\kappa z)$ of the corresponding waves one would expect a ratio of $\kappa_{\text{LDA}}/\kappa_{\text{LDA+U}} = 0.8$ for the ratio of the logarithms of the corresponding conductances. From Figs. 8.6 and 8.14 one finds for the conductances the values of $\Gamma_{\text{LDA}} = 0.4$ and $\Gamma_{\text{LDA+U}} = 0.18$ in units of $\frac{e^2}{h}$. The ratio of the logarithms of these values is $\log \Gamma_{\text{LDA}}/\log \Gamma_{\text{LDA+U}} \approx 0.5$ which is considerable smaller than expected. This difference is probably due to the very simple model used here, which does not reflect the fact that the MgO barrier consists of only three monolayers and therefore the decay of the wavefunction near the Fe/MgO interface differs from the ideal bulk value.

The little qualitative change of the conductance can also be confirmed by Fig. 8.15. The total conductance is still dominated by the majority spin conductance around the $\bar{\Gamma}$ -point. Compared to Fig. 8.8 no change except from the reduction of the absolute value of the transmission can be spotted for the majority spin contribution. The minority spin contribution is stronger dominated by states around the $\bar{\Gamma}$ -point now, however it still remains orders of magnitude smaller than the majority conductance.

8.6 Additional Oxide Layer

The different setups discussed so far differ only slightly. Neither the relaxation nor the introduction of the LDA+U for the MgO leads to significant, qualitative changes in the conductance. Now, the much more drastic effect of the additional FeO layer at the interface will be investigated. One has to be aware of some difficulties in the description of FeO by LDA or GGA based computational schemes. The straight forward applications of these methods does not give any bandgap for FeO and thus

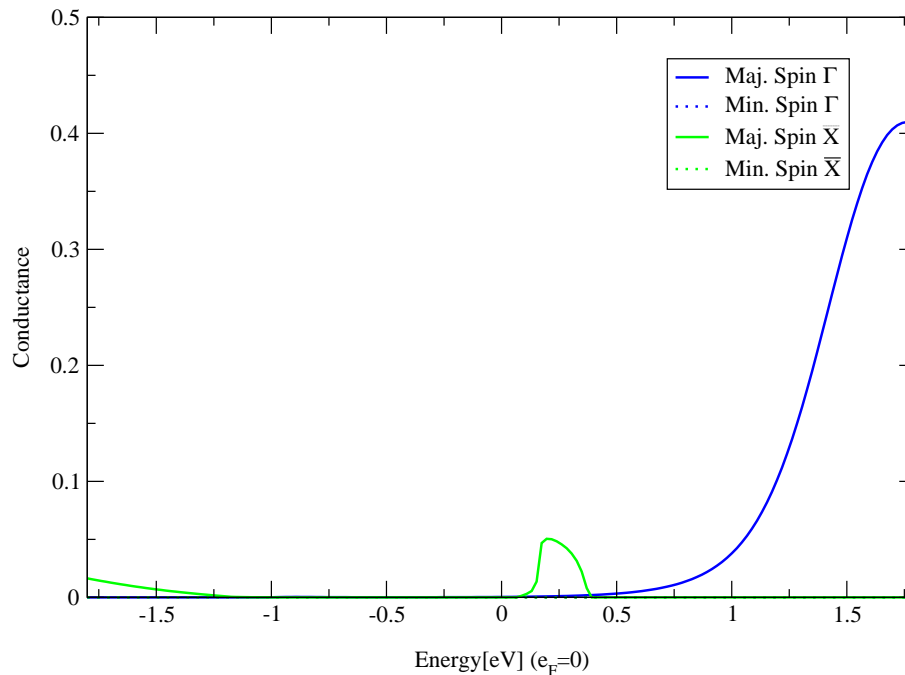


Figure 8.16: Landauer-conductance (in units of $\frac{e^2}{h}$) through a ferromagnetic Fe/FeO/MgO/FeO/Fe junction with 3 monolayers of MgO evaluating states at the $\bar{\Gamma}$ -point and at the \bar{X} -point.

can not describe the electronic structure correctly. Correspondingly, the LDA+U scheme has been applied to correct the band gap FeO. One encounters the problem of choosing a reasonable value for the U and J parameters. These have been chosen to be U=6.8 and J=0.98 values that provide an agreement of the calculated bandgap in the bulk FeO with experimental values. However, since one monolayer of FeO on-top of Fe is certainly far from being bulk FeO these values are somewhat arbitrary.

Fig. 8.16 shows the conductance obtained in the setup Fe/FeO/MgO/FeO/Fe with experimental positions used for all atoms. Again, three monolayers of MgO have been used. However, because of the two additional FeO layers, the insulating barrier region is larger in this setup than in the calculations using the three monolayer MgO barrier only and thus one expects a much smaller conductance. The curve of the energy dependent conductance shows little resemblance of those shown so far (Figs. 8.6, 8.14 or 8.11). The sharp increase of the conductance at the inset of the Fe band at the $\bar{\Gamma}$ -point found in all these plots at around -0.9 eV can no longer be found. Instead a very slow increase can be seen as one would obtain for a simple tunnel barrier due to exponential dependence of the tunneling on the energy. However, this explanation fails of course in this case since still a very strong spin dependence can be seen. The FeO layer seems to greatly reduce the coupling of the incoming Fe

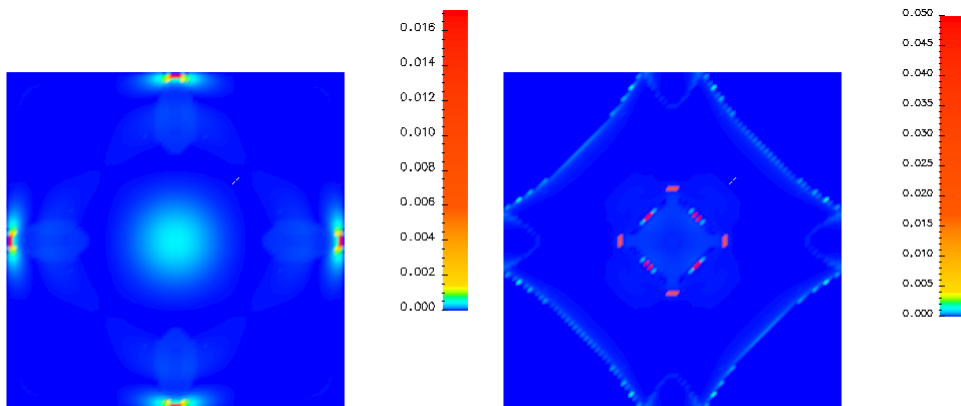


Figure 8.17: \vec{k}_{\parallel} -resolved conductance of the Fe/FeO/MgO/FeO/Fe junction through a 3 monolayers MgO barrier taking the LDA+U correction for the FeO layer into account. Again, the energy of the states is fixed to the Fermi level.

electrons at $\vec{k}_{\parallel} = 0$ to evanescent states in the barrier. One should stress that this is no symmetry effect since the two-dimensional symmetry of the junction remains unchanged. The energy dependent conductance for the \bar{M} -point is also modified. Compared to Fig. 8.9 an increase of the height to the peak slightly above the Fermi level at this specific \vec{k}_{\parallel} -point can be seen. This peak is due to a Fe majority band with very little dispersion perpendicular to the interface. Hence, the high interface sensitivity of this peak can be understood from the little group-velocity of the states of these bands.

Fig. 8.17 shows the conductance at Fermi level for the whole two-dimensional Brillouin-zone. The trend seen for the two special \vec{k}_{\parallel} -points discussed in Fig. 8.16 can clearly be confirmed. The inclusion of the additional FeO layers changes the conduction drastically. In the majority spin channel the transmission of electrons through the barrier is strongly reduced. This reduction is particularly strong around the $\bar{\Gamma}$ -point so that now the contribution from states near the \bar{X} -point to the conductance becomes significant in this spin. This contribution is due to the same peak discussed above, which crosses the Fermi level for \vec{k}_{\parallel} -vectors close to the \bar{X} -point. In the minority spin channel the most pronounced feature is the strong conductance along a line forming a circle around the \bar{M} -point of the Brillouin-zone. One would expect such a structure to occur in the plot if a band with purely two-dimensional dispersion is present in the structure. Hence, this might be due to the formation of some kind of surface resonance leading to an increased transmission.

Like in the results for the Fe/MgO/Fe junction the increase of the MgO bandgap by the application of the LDA+U method not only to FeO but also to the MgO in

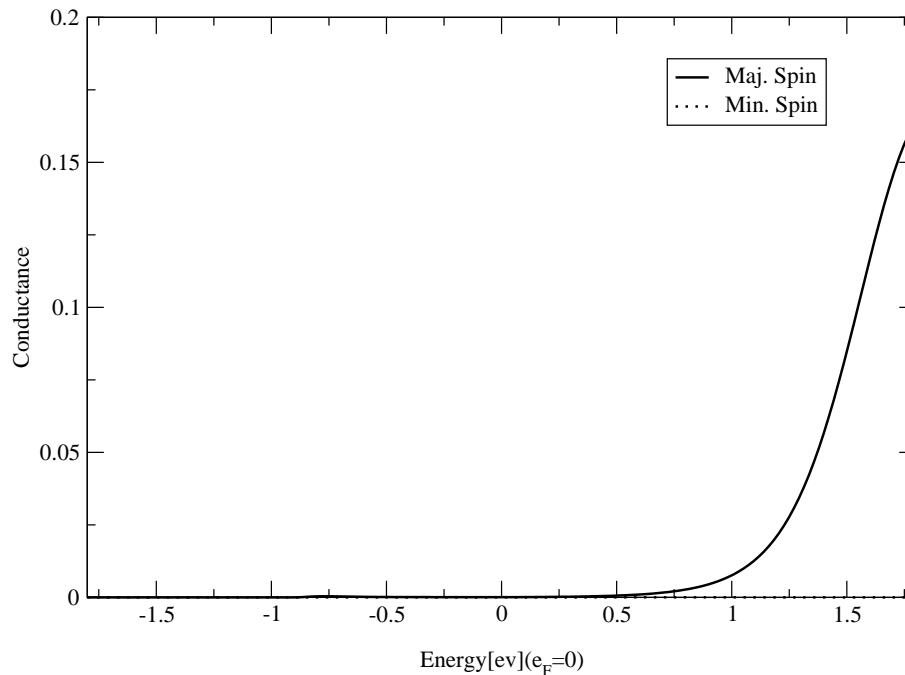


Figure 8.18: Landauer-conductance (in units of $\frac{e^2}{h}$) through a ferromagnetic Fe/FeO/MgO/FeO/Fe junction with the LDA+U method used for MgO and FeO.

this junction does not lead to any significant changes. Like discussed in the previous sections Fig. 8.18 shows only a quantitative reduction of the conductance due to the larger bandgap.

8.7 Artificial Interface Setup

To investigate the effect of the actual interface geometry on the conductance further, some calculations of a hypothetical structure are performed in which the Mg atoms are placed on top of the Fe in the Fe/MgO interface layer. While this setup definitely does not resemble any true interface, both the barrier and the lead materials are the same as in the true Fe/MgO/Fe junction. Hence, the differences found are caused only by the interface electronic structure. Fig. 8.19 shows the energy dependent conductance for such a setup at $\vec{k}_{\parallel} = 0$. At first glance one spots a quantitative agreement with the results presented so far. In particular the same single Fe band leads to a strong conduction again. The peak at the lower energy end of this band should not be taken too seriously. Due to the low velocity of these electrons the influence of the interface will be extremely high and hence the transmission at this peak should be considered as particularly arbitrary in this setup.

A closer inspection of Fig. 8.19 reveals one important difference between this setup

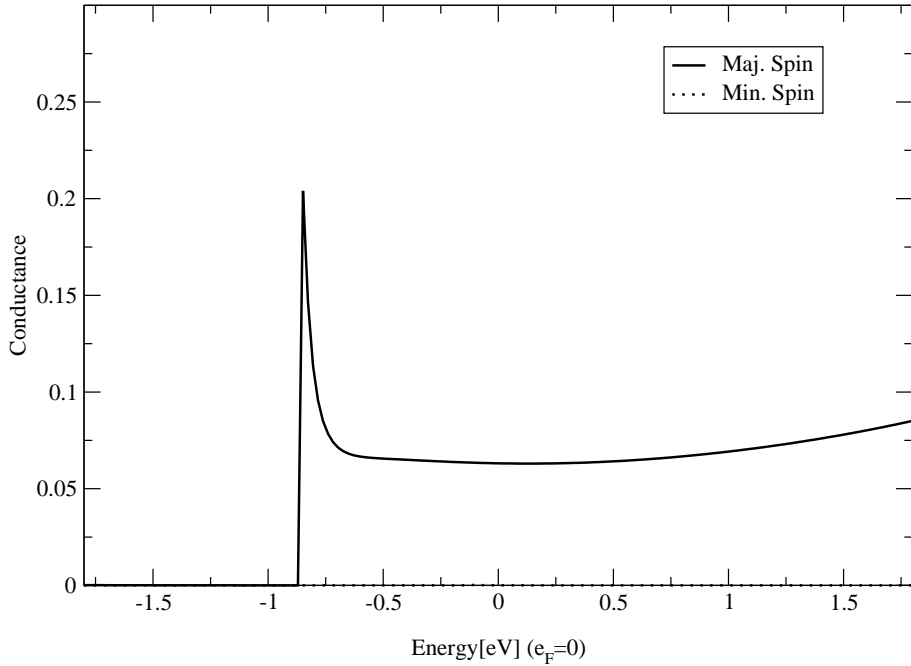


Figure 8.19: Landauer-conductance (in units of $\frac{e^2}{h}$) through a ferromagnetic Fe/MgO/Fe junction in which the Mg atoms are placed on top of the Fe atoms.

and the more physical one discussed in Sec. 8.3. The overall value of the conduction is very much reduced. Compared to the result for the unrelaxed structure shown in Fig. 8.6 the conductance for this hypothetical setup is about a factor of 8 lower. This reduction can only be explained by a much smaller coupling of the Fe Bloch state to the decaying solution within the MgO layers. This reduced coupling is an effect of the change in the interface geometry only, and hence demonstrates the importance of the actual interface structure once again.

An even more drastic change can be seen in Fig. 8.20 showing the conductance for all \vec{k}_{\parallel} -vectors. The conductance in the majority channel seems to be similar to that of the junctions discussed so far. It is dominated by the broad peak around $\vec{k}_{\parallel} = 0$. In the minority spin however, large differences can be found. While the conductance is small for the $\bar{\Gamma}$ -point itself, it becomes very large close by. When integrated over the whole two-dimensional Brillouin-zone, the conductance now becomes clearly dominated by this spin channel giving a contribution of around one order of magnitude higher than that of the majority spin.

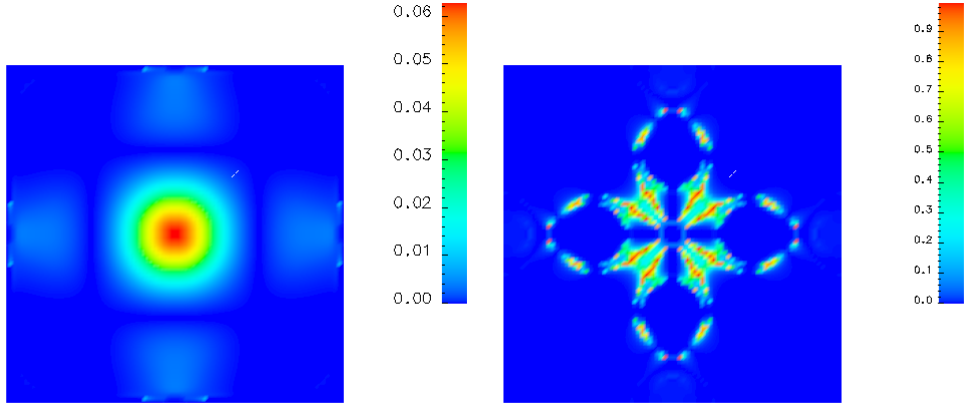


Figure 8.20: \vec{k}_{\parallel} -resolved conductance at the Fermi level of the artificial Fe/MgO/Fe junction with 3 monolayers of MgO and the Mg atoms placed on top of Fe.

8.8 Antiferromagnetic Alignment, TMR

To calculate the TMR ratio for the Fe/MgO/Fe junction the antiferromagnetically coupled system has to be investigated. From the results so far one might already expect that the conductance in an antiferromagnetically aligned junction is very small because the minority spin states of Fe were found to couple only to the strongly decaying MgO evanescent states. Indeed a calculation using an antiferromagnetically couple junctions reveals, the conductance throughout the whole Brillouin-zone is very tiny and comparable to the conductance of the minority spin channel of the ferromagnetically coupled junction. However, one should note that these calculations of the antiferromagnetic setup were very difficult. Due to the loss of symmetry in the system and the procedure of cutting the potential from only a small part of the total Fe(up)/MgO/Fe(down)/MgO supercell the symmetry between the two spin channels was broken introducing a significant error in the transmission of the order of $10^{-3} \frac{e^2}{h}$ at each \vec{k}_{\parallel} which is of the same order of magnitude as the obtained conductances. This makes the evaluation of values for the TMR ratio very uncertain. Integrating the values obtained in such a antiferromagnetic calculation and in Fig. 8.8 one obtains for the TMR ratio of the unrelaxed Fe/MgO/Fe structure a value of

$$\text{TMR} = \frac{R_{AF} - R_{FM}}{R_{AF}} > 95\%.$$

However, due to the large uncertainty in the calculated conductance of the antiferromagnetic junction and the limit number of about 8000 \vec{k} -vectors included in the Brillouin-zone integration this value has a large error.

8.9 Conclusions

Using several setups the conductance through the Fe/MgO/Fe-tunneljunction has been investigated. Different model setups were used in trying to separate different effects occurring in these junction. In the systems with a direct Fe/MgO interface the most pronounced feature was a strong spin dependence of the conductance leading to a very high spin polarization of the conductance. In agreement with results of previous KKR-based studies, in these junctions the majority spin contribution from around the $\bar{\Gamma}$ -point dominates the total conductance. Little dependence of this effect on the thickness of the barrier or the bandgap of MgO is found except from an expected decrease of the overall value of the conductance. The small interface relaxation leads to noticeable changes. However, these are purely quantitatively. A comparison of the results obtained by the Landauer formula with those given by Bardeen's formula confirmed that in the junctions no strong effects due to localized interface states can be found.

In contrast to these results, being relatively consistent for all calculated setups, the influence of a FeO layer at the interface is much more drastic. By reducing the conductance of the minority spin around the $\bar{\Gamma}$ -point drastically, the total conductance is very much reduced and its spin polarization can be expected to be significantly lower. This strong effect of the interface structure can be seen even more drastically for the artificial setup with Mg on top of Fe considered in Sec. 8.6. In this case the spin polarization of the conductance of the interface is actually reversed such that the minority spin conductance is larger than the majority spin conductance.

Finally, the antiferromagnetically coupled Fe/MgO/Fe junction was investigated showing a very low conductivity in agreement with the high predicted TMR ratios published before. However, as the results for the ferromagnetic junctions showed, these theoretical values for the TMR calculated from the ideal Fe/MgO/Fe junction must be treated with extreme caution. In experimentally prepared real junctions, the effects of additional oxides or of terraces in the Fe/MgO layer which might lead to a very local formation of the artificial setup with Mg on top of Fe will be significant. As shown, these effects can modify the spin polarization of the conductance significantly.

Chapter 9

Summary and Outlook

The present thesis introduced a new method for the description of electron transport through two-dimensional interfaces. Different aspects of the method have been described, implemented and tested successfully.

Central to the method is the implementation of the embedding method of Inglesfield. It enables the calculation of the Green function with various boundary conditions by means of the embedding potential added to the Hamiltonian. The calculation of the embedding potential itself, can impose a significant problem. It was shown how this embedding potential for the embedding of a slab within a bulk region can be obtained in terms of the states of the complex bandstructure. In order to calculate this complex bandstructure a transfer-matrix formalism was developed in this work. The transfer-matrix itself is expressed by a Green function obtained within the embedding scheme but with zero embedding potential. Combining the embedding scheme, the transfer-matrix and the complex bandstructure, it became possible to treat a realistic interface between two semi-infinite leads. From the embedded Green function of the interface the electronic conductance through this interface can be calculated.

Single electron transport was treated either in the Landauer model or using Bardeen's formalism of tunneling. These two formulas have been introduced as two different limits of transport. Both models restrict the description of the transport process to a small region. In the Landauer model the scattering or interface region is assumed to couple perfectly to the diffusive leads such that the transport is determined by the transmission of individual Bloch states. This excludes localized state from the transport process since these states are orthogonal to Bloch states and can only couple to the lead via processes beyond the single-electron description. The Landauer model of transport describes the ballistic, coherent electron transport. The

opposite limit of single-electron transport was also considered. Assuming a perfect coupling of the localized states to the leads the only limiting process in the transport is the transmission probability of single electrons across the interface. This is the limit described by Bardeen's formula of tunneling which is often called the limit of sequential tunneling. The differences of both methods have been studied in detail.

The actual calculations were performed using the FLAPW-method. Hence, the existing FLEUR code was modified for the calculation of the embedded Green function. The necessary modifications of the Hamiltonian have been discussed in detail. Beside these modifications and the changes of the overall program flow, the differences in the basis set, the setup of the potential and the use of auxiliary volumes to obtain an easy to handle setup have been described. The method has been applied to several different test systems to validate the implementation.

The spin-dependent transport properties of the Fe/MgO/Fe tunneljunction, proposed for atomically ordered tunnel-magneto resistance (TMR) devices, were investigated. Both the description of coherent tunneling in the formulation of Landauer and the sequential tunneling provided by Bardeen's equation have been evaluated. It was shown that the details of the Fe/MgO interface in this junction is of crucial importance for the tunneling conductance. While the pure relaxation of an Fe/MgO interface already changes the conductance, even more drastic modifications were found as soon as an FeO layer was inserted or if the interface was modified by interchanging the Mg and O atoms. These results might indicate a source of the difficulty to measure TMR values in real systems that are close to those large values of over 1000% predicted by previous *ab-initio* calculations. Since in real junctions used for transport measurements the interface has not been characterized on the atomic length scale, the results presented here indicate that any direct comparison of calculated results with experiments will be very difficult.

Based on the current implementation many further extensions of the method are possible. The most straight forward is the application of the embedding scheme to calculate a self-consistent charge density in the embedded region. While this was not used in the present work in which the use of the potential of a supercell was a reasonable approximation, there are cases in which the use of the self-consistent embedding scheme is of great help. For example the modeling of a true surface by a slab setup (either repeated or finite) sometimes suffers from the quantization of the levels introduced by the finite slab size. This spurious quantization makes it hard to distinguish between states which are truly localized and delocalized states coupling to bulk solutions. The self-consistent embedding scheme, being able to treat a truly semi-infinite crystal, is capable of an improved description of the system in such

cases.

However, as shortly sketched in Sec. 4.7 an even more interesting extension of the method would go beyond the usual self-consistent embedding scheme by considering junctions which are not in equilibrium because of an applied bias voltage. In the case of very weak transmission, one could chose the Fermi energy ($e_F(1) < e_F(2)$) of the two attached leads differently, thus mimicking an voltage drop over the interface region. By summing the charge density due to all states up to $e_F(1)$ and the charge density due to states incoming from the lead with the higher Fermi level from $e_F(1)$ to $e_F(2)$ one would obtain with the stationary charge distribution of the non-equilibrium system. For example this could be used for the investigation of the effect of the screening charge on the transmission of a tunnel-barrier at non-vanishing bias voltage.

Further effort could also be spend to extend the implementation of the method to include features easily available from the standard FLEUR code. In particular two options seem promising. The existing code should be easily extendable to include the treatment of non-collinear magnetism since the parts most difficult to implement are contained in the Hamiltonian setup which can simply be taken over from the non-collinear version of FLEUR. This extension would enable one to look in much greater detail into the transport processes of magnetic systems including for example the transport through magnetic domain walls or through complicated magnetic clusters between electrodes. Another interesting addition to the current implementation would be the inclusion of the spin-orbit interaction which would allow to study effects like the Rashba coupling and their influence on the spin-polarized conductance.

Concluding, a powerful new method has been developed and implemented that allows to describe electronic transport on an *ab-initio* level. Its applicability has been demonstrated for different test systems. The investigation of the magnetic Fe/MgO/Fe tunneljunction showed that the conductivity of such a contact is very depended on the details of the atomic and electronic structure of the Fe/MgO interface.

Bibliography

- [AB69] J.A. Appelbaum and W.F. Brinkman. Theory of many-body effects in tunneling. *Phys. Rev.*, 186:464, 1969.
- [AH72] J.A. Appelbaum and D.R. Hamann. Self-consistent electronic structure of solid surfaces. *Phys. Rev. B*, 6(6):2166–77, 1972.
- [AM76] Niel W. Ashcroft and N. David Mermin. *Solid State Physics*. Saunders College Publications, 1976.
- [And75] O. K. Anderson. Linear methods in band theory. *Phys. Rev. B*, 12:3060, 1975.
- [BBF⁺88] M.N. Baibich, J.M. Broto, A. Fert, F. Nguyen Van Dau, F. Petroff, P. Etienne, G. Creuzet, A. Friederich, and J. Chazelas. Giant magnetoresistance of (001)Fe/(001)Cr magnetic superlattices. *Phys. Rev. Lett.*, 61:2472, 1988.
- [BCP⁺01] M. Bowen, V. Cros, F. Petroff, A. Fert, C.M. Boubeta, J.L. Costa-Kramer, J.V. Anguita, A. Cebollada, F. Briones, J.M. de Teresa, L. Morellon, M.R. Ibarra, F. Guell, F. Peiro, and A. Cornet. Large magnetoresistance in Fe/MgO/FeCo(001) epitaxial tunnel junctions on GaAs(001). *Appl. Phys. Lett.*, 79:1655, 2001.
- [BGSZ89] G. Binasch, P. Grunberg, F. Saurenbach, and W. Zinn. Enhanced magnetoresistance in layered magnetic structures with antiferromagnetic interlayer exchange. *Phys. Rev. B*, 39:4828, 1989.
- [BS89] H. U. Baranger and A. D. Stone. Electrical linear-response theory in an arbitrary magnetic field: A new fermi-surface formation. *Phys. Rev. B*, 40:8169, 1989.
- [Bur63] G.A. Burdick. Energy band structure of copper. *Phys. Rev. B*, 129:138, 1963.

- [Büt86] M. Büttiker. Four-terminal phase coherent conductance. *Phys. Rev. Lett.*, 57:1761, 1986.
- [BZSM01] W.H. Butler, X.-G. Zhang, T.C. Schulthess, and J.M. MacLaren. Spin-dependent tunneling conductance of Fe|MgO|Fe sandwiches. *Phys. Rev. B*, 63:054416/1, 2001.
- [CBLC96] L. Chico, L. X. Benedict, S. G. Louie, and M. L. Cohen. Quantum conductance of carbon nanotubes with defects. *Phys. Rev. B*, 54:2600, 1996.
- [CNvHI93] S. Crampin, M. Nekovee, J. B. A. N. van Hoof, and J. E. Inglesfield. Subvolume embedding for interfacial electronic structure. *Surf. Sci.*, 287/88:732, 1993.
- [CvHNI92] S. Crampin, J. B. A. N. van Hoof, M. Nekovee, and J. E. Inglesfield. Full potential embedding for surfaces and interfaces. *J. Phys. Cond. Mat.*, 4:1475, 1992.
- [CVHSS97] J. Cerdá, M. A. Van Hove, P. Sautet, and M. Salmeron. Efficient method for the simulation of STM images. I. Generalized Green-function formalism. *Phys. Rev. B*, 56:15885, 1997.
- [DBZA84] P.H. Dederichs, S. Blugel, R. Zeller, and H. Akai. Ground states of constrained systems: application to cerium impurities. *Physical Review Letters*, 53:2512, 1984.
- [DVKPL01] M. Di Ventra, S.-G. Kim, S. T. Pantelides, and N. D. Lang. Temperature effects on the transport properties of molecules. *Phys. Rev. Lett.*, 86:288, 2001.
- [DVPL00] M. Di Ventra, S. T. Pantelides, and N. D. Lang. First-principles calculation of transport properties of a molecular device. *Phys. Rev. Lett.*, 84:979, 2000.
- [Esc96] H. Eschrig. *The fundamentals of Density Functional Theory*. Teubner, Stuttgart, Leipzig, 1996.
- [Fan61] U. Fano. Effects of configuration interaction on intensities and phase shifts. *Phys. Rev.*, 124:1866, 1961.
- [Feu74a] T.E. Feuchtwang. Tunneling theory without the transfer-hamiltonian formalism. I. *Phys. Rev. B*, 10:4121, 1974.

-
- [Feu74b] T.E. Feuchtwang. Tunneling theory without the transfer-hamiltonian formalism. II. Resonant and inelastic tunneling across a junction of finite width. *Phys. Rev. B*, 10:4135, 1974.
- [GBW82] H. Rohrer Ch. Gerber G. Binnig and E. Weibel. 7*7 reconstruction on Si(111) resolved in real space. *Phys. Rev. Lett.*, 50(120), 1982.
- [HAB⁺99] S. Heinze, R. Abt, S. Blügel, G. Gilarowski, and H. Niehus. Scanning tunneling microscopy images of transition-metal structures buried below noble-metal surfaces. *Phys. Rev. Lett.*, 83:4808, 1999.
- [HBP⁺98] S. Heinze, S. Blügel, R. Pascal, M. Bode, and R. Wiesendanger. Prediction of bias-voltage-dependent corrugation reversal for STM images of bcc (110) surfaces: W(110), Ta(110), and Fe(110). *Phys. Rev. B*, 58:16432, 1998.
- [Hei64] V Heine. *Surf. Sci.*, 2:1, 1964.
- [HK64] P. Hohenberg and W. Kohn. *Phys. Ref.*, 136:864, 1964.
- [HT94] K. Hirose and M. Tsukada. First-principles theory of atom extraction by scanning tunneling microscopy. *Phys. Rev. Lett.*, 73(1):150–3, 1994.
- [HT95] K. Hirose and M. Tsukada. First-principles calculation of the electronic structure for a bielectrode junction system under strong field and current. *Phys. Rev. B*, 51:5278, 1995.
- [IB88] J.E. Inglesfield and G.A. Benesh. Surface electronic structure: embedded self-consistent calculations. *Phys. Rev. B*, 37:6682, 1988.
- [Ing81] J. E. Inglesfield. A method of embedding. *J. Phys. C*, 14:3795, 1981.
- [Ish] H. Ishida. private communication.
- [Ish97] H. Ishida. Surface-embedded Green function calculation using non-local pseudopotentials. *Surf. Sci.*, 388(1-3):71–83, 1997.
- [Ish01] H. Ishida. Surface-embedded Green function method: A new formulation using linearized-augmented-plane-wave basis set. *Phys. Rev. B*, 63:165409/1, 2001.
- [IT01] H. Ishida and M. I. Trioni. Comparison of the embedding and dyson-equation methods in the Green's-function calculation of a defect in solids. *Phys. Rev. B*, 63:155108, 2001.

- [Jan78] J.F. Janak. Proof that $\partial e/\partial n_i = \epsilon_i$ in density-functional theory. *Phys. Rev. B*, 18(12):7165, 1978.
- [JG89] R. O. Jones and O. Gunnarson. Density functional formalism, its applications and prospects. *Rev. Mod. Phys.*, 61:689, 1989.
- [Jul] M. Julliere. Tunneling between ferromagnetic films.
- [KBT00] N. Kobayashi, M. Brandbyge, and M. Tsukada. First-principles study of electron transport through monatomic al and na wires. *Phys. Rev. B*, 62:8430, 2000.
- [KDT+00] J. Kudrnovský, V. Drchal, I. Turek, C. Blaas, P. Weinberger, , and P. Bruno. Ab initio theory of perpendicular magnetotransport in metallic multilayers. *Phys. Rev. B*, 62:15084, 2000.
- [KH77] D.D. Koelling and B.N. Harmon. A technique for relativistic spin-polarised calculations. *J. Phys. C*, 10:3107, 1977.
- [Koh83] Walter Kohn. Density functional theory: Basic results and some observations. In Reiner M. Dreizler and Joao da Providencia, editors, *Density Functional Methods in Physics*. NATO ASI Series, 1983.
- [KS65] W. Kohn and L.J. Sham. *Phys. Rev.*, 140:A1133, 1965.
- [KS76] N. Kar and P. Soven. Field emission energy distribution from (111) copper. *Solid State Commun.*, 19:1041, 1976.
- [KS95] E. E. Krasovskii and W. Schattke. The extended-lapw-based k.p method for complex band structure calculations. *Solid State Commun.*, 93(9):775, 1995.
- [KS97] E.E. Krasovskii and W. Schattke. Surface electronic structure with the linear methods of band theory. *Phys. Rev. B*, 56:12874, 1997.
- [KS99] E.E. Krasovskii and W. Schattke. Calculation of the wave functions for semi-infinite crystals with linear methods of band theory. *Phys. Rev. B*, 59:R15609, 1999.
- [KSS99] E. E. Krasovskii, F. Starrost, and W. Schattke. Augmented fourier components method for constructing the crystal potential in self-consistent band-structure calculations. *Phys. Rev. B*, 59(16):10504, 1999.

-
- [KUB⁺01] M. Klaua, D. Ullmann, J. Barthel, W. Wulfhekel, J. Kirschner, R. Urban, T.L. Monchesky, A. Enders, J.F. Cochran, and B. Heinrich. Growth, structure, electronic, and magnetic properties of MgO/Fe(001) bilayers and Fe/MgO/Fe(001) trilayers. *Phys. Rev. B*, 64:134411/1, 2001.
- [Kur97] Philipp Kurz. Non-collinear magnetism of ultrathin magnetic films. Master's thesis, RWTH Aachen, 1997.
- [Kur01] Ph. Kurz. *Non-Collinear Magnetism at Surfaces and in Ultrathin Films*. PhD thesis, RWTH-Aachen, 2001.
- [Lan57] R. Landauer. *IBM Journal Res. Dev.*, 1:223, 1957.
- [Lan95] N. D. Lang. Resistance of atomic wires. *Phys. Rev. B*, 52:5335, 1995.
- [Lev79] Mel Levy. Universal variational functionals of electron densities, first-order density matrices, and natural spin-orbits and solution of the v-representability problem. *Proc. Natl. Acad. Sci.*, 76(12):6062, 1979.
- [LLP79] L. D. Landau, E. M. Lifshits, and L. P. Pitaevskij. *Quantenmechanik*, volume 3 of *Lehrbuch der theoretischen Physik*. Akademie Verlag, Berlin, 6 edition, 1979.
- [LYB⁺99] V. P. LaBella, H. Yang, D. W. Bullock, P. M. Thibabo, Peter Kratzer, and Matthias Scheffler. Atomic structure of the GaAs(001)-(2×4) surface resolved using scanning tunneling microscopy and first-principles theory. *Phys. Rev. Lett.*, 83:2989, 1999.
- [Mat97] J. Mathon. Tight-binding theory of tunneling giant magnetoresistance. *Phys. Rev. B*, 56:11810, 1997.
- [MJW78] V.L. Moruzzi, J. F. Janak, and A. R. Williams. Pergamon, New York, 1978.
- [MOB⁺02] J.L. Mozos, P. Ordejon, M. Brandbyge, J. Taylor, and K. Stokbro. Simulations of quantum transport in nanoscale systems: application to atomic gold and silver wires. volume 13, page 346, 2002.
- [MPJ⁺02] H.L. Meyerheim, R. Popescu, K. Jedrecy, M. Vedpathak, M. Sauvage-Simkin, R. Pinchaux, B. Heinrich, and J. Kirschner. Surface x-ray diffraction analysis of the MgO/Fe(001) interface: Evidence for an FeO layer. *Phys. Rev. B*, 65:144433, 2002.

- [NBHJ99] A. Nakamura, M. Brandbyge, L. B. Hansen, and K. W. Jacobsen. Density functional simulation of a breaking nanowire. *Phys. Rev. Lett.*, 82:1538, 1999.
- [ORR02] G. Onida, Lucia Reining, and A. Rubio. Electronic excitations: density-functional versus many-body Green's-function approaches. *Reviews of Modern Physics*, 74:601, 2002.
- [PCV⁺92] J.P. Perdew, J.A. Chevary, S.H. Vosko, K.A. Jackson, M.R. Pederson, D.J. Singh, and C. Fiolhais. Atoms, molecules, solids, and surfaces: Applications of the generalized gradient approximation for exchange and correlation. *Phys. Rev. B*, 46:6671, 1992.
- [Pen96] Rossitza Pentcheva. Ab-initio Rechnungen zum Zusammenhang zwischen Magnetismus und Struktur ultradünner Filme. Master's thesis, Universität Köln, 1996.
- [Per83] John P. Perdew. What do the Kohn-Sham orbital energies mean? How do atoms dissociate? In Reiner M. Dreizler and Joao da Providencia, editors, *Density Functional Methods in Physics*. NATO ASI Series, 1983.
- [PZ81] J. P. Perdew and A. Zunger. Self-interaction correction to density-functional approximations for many-electron systems. *Phys. Rev. B*, 23:5048, 1981.
- [RZM01] I. Riedel, P. Zahn, and I. Mertig. Ab initio calculation of the transmission coefficients from a superlattice electronic structure. *Phys. Rev. B*, 63:195403, 2001.
- [Sch93] F. Schwabl. *Quantenmechanik*. Springer, 4 edition, 1993.
- [SD94] I.V. Solov'yev and P. H. Dederichs. Ab initio calculations of coulomb u parameters for transition-metal impurities. *Phys. Rev. B*, 49:6736, 1994.
- [SFM⁺00] G. Schmidt, D. Ferrand, L.W. Molenkamp, A.T. Filip, and B.J. van Wees. Fundamental obstacle for electrical spin injection from a ferromagnetic metal into a diffusive semiconductor. *Physical Review B (Condensed Matter)*, 62:R4790, 2000.
- [SH88] M. D. Stiles and D. R. Hamann. Ballistic electron transmission through interfaces. *Phys. Rev. B*, 38(3):2021–37, 1988.

-
- [Sin91] D. Singh. Ground-state properties of lanthanum: Treatment of extended-core states. *Phys. Rev. B*, 43(8):6388–92, 1991.
- [Sin94] D. J. Singh. *Planewaves, Pseudopotentials and the LAPW Method*. Kluwer Academic Publishers, Boston, Dordrecht, London, 1994.
- [SLP99] A.B. Shick, A. I. Lichtenstein, and W. E. Pickett. Implementation of the LDA+U method using the full-potential linearized augmented plane-wave basis. *Phys. Rev. B*, 60(15):10763, 1999.
- [SNS00] E. Sjöstedt, L. Nordström, and D. J. Singh. An alternative way of linearizing the augmented plane-wave method. *Solid State Commun.*, 114(1):15–20, 2000.
- [SS88] A.D. Stone and A. Szafer. What is measured when you measure a resistance? - The landauer formula revisited. *IBM Journal Res. Dev.*, 32:384, 1988.
- [Sti96] M. D. Stiles. Spin-dependent interface transmission and reflection in magnetic multilayers. *J. Appl. Phys.*, 79:5805, 1996.
- [SW89] J. M. Soler and A. R. Williams. Simple formula for the atomic forces in the augmented-plane-wave method. *Phys. Rev. B*, 40(3):1560–4, 1989.
- [SW93] Max Schubert and Gerhard Weber. *Quantentheorie*. Spektrum Akademischer Verlag, Heidelberg, 1993.
- [TBCI96] M. I. Trioni, G. .P. Brivio, S. Crampin, and J. E. Inglesfield. Embedding approach to the isolated adsorbate. *Phys. Rev. B*, 53:8052, 1996.
- [TBS02] J. Taylor, M. Brandbyge, and K. Stokbro. Theory of rectification in four wires: The role of electrode coupling. *Physical Review Letters*, 89:138301/1, 2002.
- [TSW93] W.M. Temmerman, Z. Szotek, and H. Winter. Self-interaction-corrected electronic structure of La_2CuO_4 . *Phys. Rev. B*, 47:11533, 1993.
- [vBH72] U. von Barth and L. Hedin. Local density approximation. *J. Phys. C.*, 5:1629, 1972.
- [VDM⁺96] J. L. Vassent, M. Dynna, A. Marty, B. Gilles, and G. Patrat. A study of growth and the relaxation of elastic strain in MgO on Fe(001). *Journal of Applied Physics*, 80:5727, 1996.

- [vHSKB98] J.B.A.N. van Hoof, K.M. Schep, P.J. Kelly, and G.E.W. Bauer. Ab initio magnetoresistance in magnetic domain walls. *J. Magn. Magn. Mater.*, 177-181:188, 1998.
- [VSB⁺97] B. Voigtländer, V. Scheuch, H.P. Bonzel, S. Heinze, and S. Blügel. Chemical identification of atoms at multicomponent surfaces on an atomic scale: CoSi₂(100). *Phys. Rev. B*, 55:R13444, 1997.
- [VWN80] S.H. Vosko, L. Wilk, and N. Nusair. Accurate spin-dependent electron liquid correlation energies for local spin density calculations: a critical analysis. *Can. J. Phys.*, 58:1200, 1980.
- [Wac86] G. Wachutka. New layer method for the investigation of the electronic properties of two-dimensional periodic spatial structures: First applications to copper and aluminium. *Phys. Rev. B*, 34(12):8512, 1986.
- [WB82] G Wachutka and H Bross. Bivariational methods applied to schrodinger's and dirac's equations. *J. of Phys. A*, 15(10):3083–3107, 1982.
- [WEK⁺01] E. Wahlstrom, I. Ekvall, T. Kihlgren, H. Olin, S.-A. Lindgren, and L. Wallden. Low-temperature structure of S/Cu(111). *Phys. Rev. B*, 64:155406/1, 2001.
- [WKU⁺01] W. Wulfhekel, M. Klaua, D. Ullmann, F. Zavaliche, J. Kirschner, R. Urban, T. Monchesky, and B. Heinrich. Single-crystal magnetotunnel junctions. *Appl. Phys. Lett.*, 78:509, 2001.
- [WMZ⁺02] O. Wunnicke, Ph. Mavropoulos, R. Zeller, P.H. Dederichs, and D. Grundler. Ballistic spin injection from Fe(001) into ZnSe and GaAs. *Phys. Rev. B*, 65:241306/1, 2002.
- [WRW⁺] H.B. Weber, J. Reichert, F. Weigend, R. Ochs, D. Beckmann, M. Mayor, R. Ahlrichs, and H. v.Löhneysen. Electronic transport through single conjugated molecules.
- [WZD⁺98] K. Wildberger, R. Zeller, P. H. Dederichs, J. Kudrnovsky, and P. Weinberger. Interface reflectivities and quantum-well states in magnetic multilayers. *Phys. Rev. B*, 58:13721, 1998.
- [XKB⁺01] K. Xia, P.J. Kelly, G.E.W. Bauer, I. Turek, J. Kudrnovský, and V. Drchal. Interface resistance of disordered magnetic multilayers. *Phys. Rev. B*, 63:64407, 2001.

- [ZDD82] R. Zeller, J. Deutz, and P.H. Dederichs. Application of complex energy integration to selfconsistent electronic structure calculations. *Solid State Communications*, 44:993, 1982.

Veröffentlichungen

Teile der vorliegenden Arbeit wurden veröffentlicht in:

- D. Wortmann, H. Ishida, and S. Blügel
„Embedded Green-function approach to the ballistic electron transport through an interface“
Physical Review B **66**, 075113 (2002)
- D. Wortmann, H. Ishida, and S. Blügel
„Ab initio Green-function formulation of the transfer matrix: Application to complex band structures“
Physical Review B **65**, 165103 (2002)

Weitere Veröffentlichungen:

- D. Wortmann, P. Kurz, S. Heinze, K. Hirai, G. Bihlmayer, and S. Blügel
„Resolving noncollinear magnetism by spin-polarized scanning tunneling microscopy“
Journal of Magnetism and Magnetic Materials **240**, 57 (2002)
- S. Heinze, P. Kurz, D. Wortmann, G. Bihlmayer, and S. Blügel
„Complex magnetism in ultra-thin films: atomic-scale spin structures and resolution by the spin-polarized scanning tunneling microscope“
Applied Physics A **75**, 25 (2002)
- D. Wortmann, S. Heinze, Ph. Kurz, G. Bihlmayer and S. Blügel
„Resolving complex atomic-scale spin-structures by spin polarized scanning tunneling microscopy“
Physical Review Letters **86**, 4132 (2001)
- D. Wortmann, S. Heinze, G. Bihlmayer and S. Blügel
„Interpreting STM images of the MnCu/Cu(100) surface alloy“
Physical Review B **62**, 2862 (2000)

Lebenslauf

Persönliche Daten	Name:	Daniel Wortmann
	Adresse:	Rosenplätze 24 59494 Soest
	geboren:	30.12.1973 in Münster
	Familienstand:	ledig
Schulbildung	1980-1984	Grundschule Ascheberg
	1984-1985	Gymnasium Lüdinghausen
	1985-1993	Aldegrevergymnasium Soest
Ersatzdienst	07.93-09.94	Kolpingbildungsstätte Soest
Studium	10.94-09.96	Grundstudium Physik und Mathematik an der Universität Dortmund
	09.96-06.97	Studium Physik am King's College London (DAAD-Stipendiat)
	10.97-02.00	Hauptstudium Physik an der Universität Dortmund
	12.99-01.00	Diplomarbeit am Forschungszentrum Jülich "Interpretation of Scanning Tunneling Microscopy and Spectroscopy of Magnetic Metal Surfaces by Electron Theory"
	02. 2000	Diplom in Physik
Promotion	seit 03.00	Promotion am Forschungszentrum Jülich „An embedding Green function approach for electron transport through interfaces“
	03.01-06.01/	DAAD-Stipendiat
	01.02-03.02	an der Nihon-University Tokyo, Japan

Danksagung

Mein größter Dank gilt Herrn Prof. Dr. Stefan Blügel für die intensive Betreuung dieser Arbeit. Seine grosse Begeisterung für die Physik des Elektronentransports konnte mich immer wieder neu motivieren und seine unzähligen guten Ideen und Vorschläge haben mir oft entscheidend weitergeholfen. Besonders dankbar bin ich auch für die Möglichkeit, diese Arbeit in seiner Arbeitsgruppe am Institut für Festkörperforschung des Forschungszentrum Jülich durchführen zu können.

Diese Arbeit wäre nicht möglich gewesen ohne die vielfältige Hilfe von Herrn Prof. Dr. Hiroshi Ishida. Viele wesentliche Ergebnisse wurden mit seiner Unterstützung erzielt. Für die überaus freundliche Aufnahme während meiner Besuche in Tokyo bin ich ihm zu besonderem Dank verpflichtet.

Herrn Prof. Dr. Peter H. Dederichs danke ich für die Bereitschaft zur Übernahme des Koreferats und für die Anregungen, die aus den Gesprächen mit ihm hervor gegangen sind.

Herr Dr. Gustav Bihlmayer hat ganz wesentlich zum Gelingen dieser Arbeit beigetragen. Seine Hilfe beim Verständnis des FLEUR Programms ist unersetzlich, aber auch die häufigen Diskussionen über physikalische Probleme waren immer fruchtvoll. Gespräche mit Herrn Dr. Stefan Heinze haben mir beim Verständnis des Tunnelproblems im STM sehr geholfen und mein Interesse für Elektronentransport geweckt. Herr Dr. Philipp Kurz hat mir durch seine Arbeit über den nicht-kollinearen Magnetismus viele Anregungen gegeben und zu meinem Verständnis der FLAPW Methode beigetragen. Herrn Manfred Niesert und Herrn Yuri Mokrousov bin ich für das unermüdete Korrekturlesen dieser Arbeit besonders dankbar.

Bei allen weiteren, nicht namentlich erwähnten, Mitgliedern der Arbeitsgruppe in Jülich möchte ich mich für die Unterstützung und die angenehme Arbeitsatmosphäre bedanken.

Mein besonderer Dank gilt meiner Freundin Maryam, meinen Eltern Christel und Manfred Wortmann sowie meiner Schwester Anke für ihre fortwährende Unterstützung.